2012

A 2-D, variable-density numerical model of subsurface fluid flow through the Edwards Aquifer, New Braunfels, TX: mechanisms inhibiting flow across the freshwater/saline-water interface

Scott Ryan Tipple
Louisiana State University and Agricultural and Mechanical College

A 2-D, VARIABLE-DENSITY NUMERICAL MODEL OF SUBSURFACE FLUID FLOW THROUGH THE EDWARDS AQUIFER, NEW BRAUNFELS, TX: MECHANISMS INHIBITING FLOW ACROSS THE FRESHWATER/SALINE-WATER INTERFACE

A Thesis

Submitted to the Graduate Faculty of the
Louisiana State University and
Agricultural and Mechanical College
in partial fulfillment of the
requirements for the degree of
Master of Science

in

The Department of Geology and Geophysics

By
Scott Ryan Tipple
B.S., Louisiana State University, 2009
August, 2012

ACKOWLEDGMENTS

I would like to thank my advisor, Dr. Carol Wicks, for all of her support and direction that she has provided during my research. Her enthusiasm was always contagious, and for that, I am extremely thankful. I would also like to thank Dr. Jeffrey Hanor and Dr. Jeffrey Nunn for their guidance during our discussions of this research. Thanks to Geary Schindel, Roberto Esquilin, and others from the Edwards Aquifer Authority, whom served as host during my research in San Antonio, providing access to geophysical well logs and geochemical data sets, as well as personal knowledge and advice. Particular thanks to Roberto Esquilin, whom served as my direct contact at the Edwards Aquifer Authority for questions I had throughout this research. Thanks to my family for their support, particularly my father, John Mark Tipple, and my brother, Brett James Tipple, for their support and wisdom. Thanks to my friends, whom were there to take my mind of things when I needed a break from school work. Thanks to Peter Pan Hongbin, whom loaded Basin2 on my computer. Finally, I would like to thank Patti Prejean, my longtime girlfriend, for her continued support and encouragement throughout my research. In addition, this work was funded by the American Association of Petroleum Geologists Paul Danheim Nelson Research Grant, the Gulf Coast Association of Geological Societies Research Grant, and the Geological Society of America Research Grant. Thank you to these institutions for contributing to the success of this research.

TABLE OF CONTENTS

LIST OF TABLES

LIST OF FIGURES

ABSTRACT

The Edwards aquifer in south-central Texas, U.S., composed of faulted carbonate bedrock, contains freshwater and saline water. In aquifers that are used as a source of drinking water and that contain fresh and saline waters, saline-water intrusion can result in degradation of water quality. Yet, in the Edwards aquifer, limited saline-water intrusion has occurred. The questions addressed are "Why is the saline-water intrusion less than expected," and "Is there a trigger that will result in saline-water intrusion into the freshwater reservoir?" Three hypotheses were tested. One: an extremely saline water density might prevent mixing across the interface. Two: faults could be acting as a barrier between the freshwater and saline-water zones, preventing movement of the saline water into the freshwater zone. Three: the permeability of the bedrock in the saline water zone might be extremely low, limiting movement of the saline water. A transect of observation wells was chosen in New Braunfels, TX for study.

2-D, variable-density numerical models of groundwater flow were used to determine which factor controlled the lack of saline-water intrusion. Numerical models were produced for each hypothesis using Basin2. It is clear from each model that fault permeability and fault compartmentalization is the primary mechanism inhibiting flow across the freshwater/saline-water interface. When horizontal fault permeability reached 0.01 D, flow was significantly reduced across the interface. When these values reached 0.001 D, flow across the interface ceased. To a lesser extent, saline-water zone permeability controlled the movement of flow across the interface, if permeability values were reduced by three orders of magnitude. However, extremely high saline water densities did not inhibit flow.

A trigger that would increase fault permeability would be continued dissolution of the carbonate rocks, but it most likely would take tens of thousands of years for dissolution to

significantly increase the permeability of the fault surfaces. In addition, dedolomitization of the saline water zone would be another trigger that would induce flow across the interface, but since little diagenesis in the saline water zone has been observed, dedolomitization is not a pressing issue.

INTRODUCTION

In the United States, karst formations comprise 20% of the land surface and supply approximately 40% of the country's drinking water (Karst Waters Institute, 2011) and approximately 25% of the world's drinking water (Ford and Williams, 2007). Saline-water intrusion is a significant problem in many karst aquifers (Fleury et al., 2007). Nowhere is saline-water intrusion more prevalent than along the Atlantic Coast (Barlow and Wild, 2002). The most notable saline-water intrusions occur in Florida in the Floridan and Biscayne aquifers (Fleury et al., 2007; Harmon and Wicks, 2006). However, coastal settings are not the only locations of saline-water intrusion. The Edwards aquifer in Texas and the Ozark aquifer in Missouri are also sites of potential saline-water intrusion (Miller, 1971).

Saline water intrusion is controlled by changes in hydraulic head and is associated with reduced hydraulic head associated with artificial discharge (Fleury et al., 2007; Leve, 1983). Substantial groundwater withdrawals from the aquifer lowers the hydraulic head in the aquifer, allowing saline water to flow down gradient toward the well and form a saline wedge in the subsurface (Fleury et al., 2007; Arfib, 2007). Coupled with the fact that karst aquifers possess many conduits that readily allow for fluid flow, saline-water intrusion can occur quite easily under heavy pumping conditions (Fleury et al., 2007). Saline-water intrusion will likely worsen as populations that rely on these karst aquifers for drinking water grow, requiring more pumping and more strain on these systems.

More than 2 million people throughout south-central Texas rely on the Edwards aquifer for their drinking water (Cox et al., 2009). Pumping in the San Antonio metropolitan area has put a substantial strain on the freshwater supply within Edwards aquifer (Painter et al., 2007). San Antonio is pumping at a rate of more than 4.02×10^6 gallons/day, and the surrounding areas are

also pumping at significant rates (Lindgren et al., 2004). Figure 1 shows the increased pumping rates from 1934-2000 (Lindgren et al., 2004). Although, minimal saline-water encroachment across the freshwater/saline water interface has occurred to date, but saline-water intrusion should still be a pressing concern for the people that rely on the Edwards aquifer for drinking water. It is important to understand why there has been so little saline water flow across the interface by determining what mechanisms impede movement. But, it is also extremely important to determine if there is a trigger that will increase the rate of saline water encroachment across the boundary and if so, to determine that rate and the quantity of saline water which would flow across the interface. If any of three factors hypothesized here (extremely high fluid density, fault compartmentalization, or saline water zone permeability) are overcome or disrupted, severe water quality degradation could occur, affecting the many people of Texas that rely on the Edwards aquifer for fresh, clean water. Four wells, highlighted in red in Figure 2, were selected in New Braunfels, Texas to test the three hypotheses.

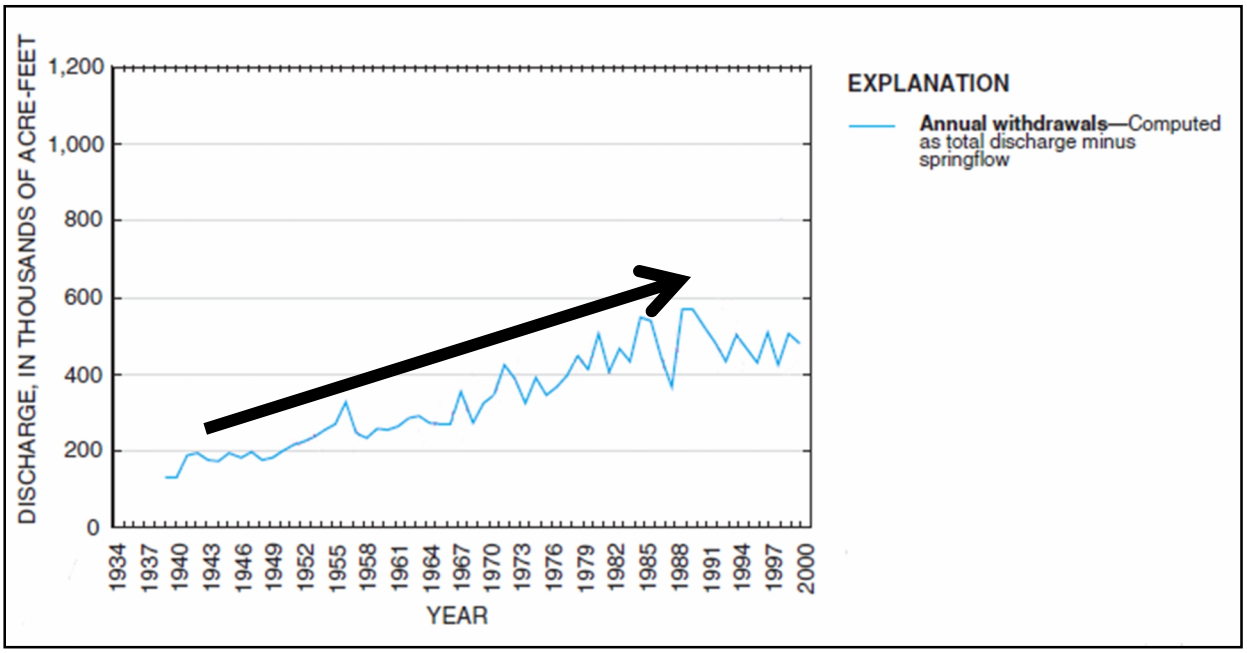

Figure 1. Annual ground-water discharge, springflow, and withdrawals for the San Antonio region, Texas, 1939-2000. Image modified from Lindgren et al., 2004. The black arrow indicates the trend of increasing annual withdrawals for the San Antonio region.

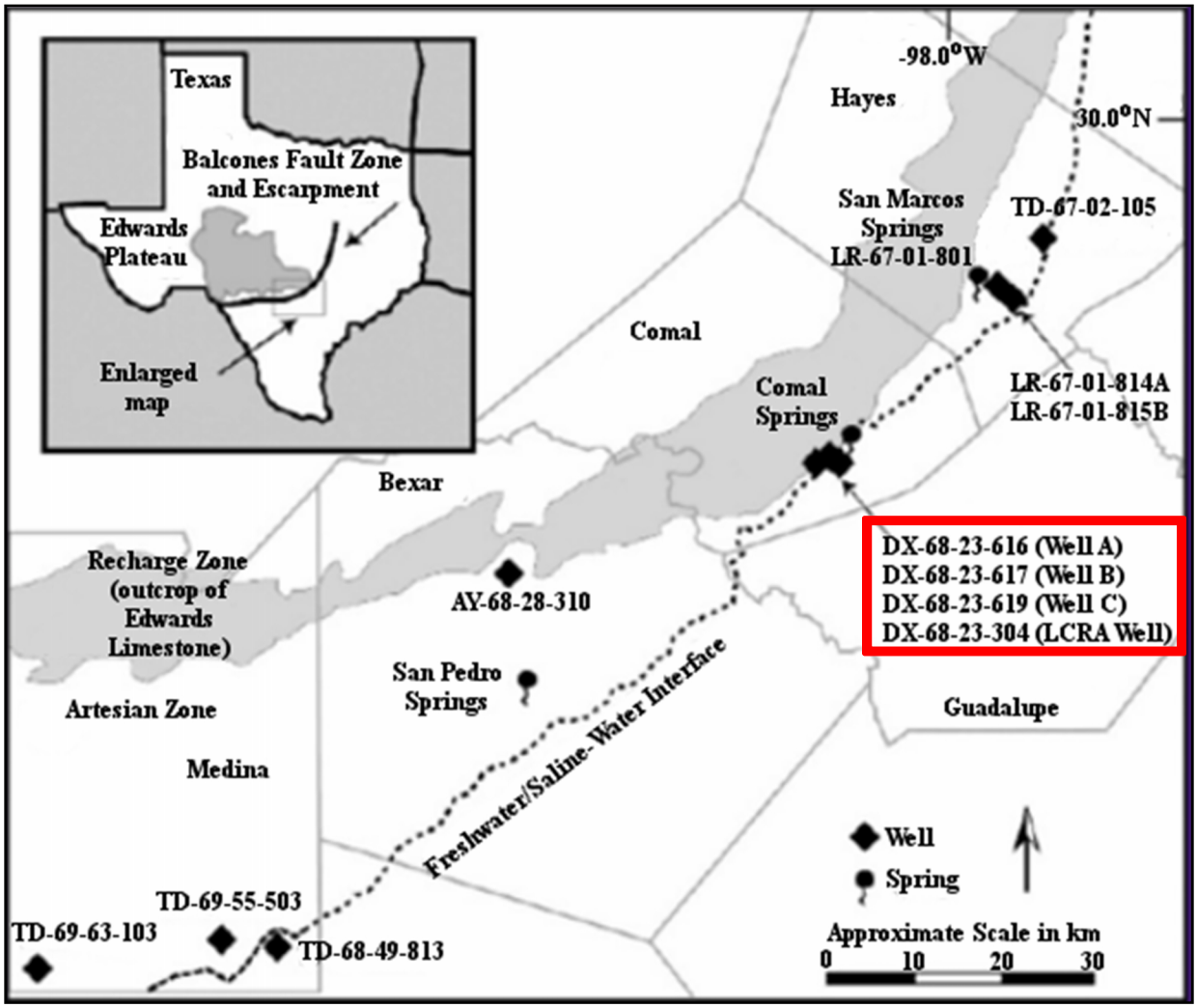

Figure 2. The wells used in New Braunfels, Texas are highlighted in red. Image modified from Birdwell and Engel, 2009.

REGIONAL SETTING

The Edwards aquifer consists of highly karstified Cretaceous limestone and covers an area of about 5424 km^2 (Maclay and Small, 1983; Cox et al., 2009). In a north-northeast trending arcuate transect that parallels the Balcones Fault Zone (BFZ) (Cox et al., 2009), the Edwards aquifer is situated and covers a distance of 290 km and a width between 8 and 64 km wide, reaching from north of Austin to south of Brackettville (Figure 3) (Birdwell and Engel, 2009). The recharge zone for the Edwards aquifer resides on the Edwards Plateau, with groundwater generally flowing west to east (Cox et al., 2009). The aquifer discharges into several large springs (Cox et al., 2009), with the Comal and San Marcos being the two largest springs in terms of discharge (Loáiciga et al., 2000).

The freshwater/saline-water interface is known as the "bad-water" line (Groschen and Buszka, 1997). Up-dip of this interface, the freshwater zone exists in confined and unconfined sections (Scanlon et al., 2003). Down-dip of this interface, the saline-water zone is confined and has salinity ranges of 1,000 to 12,500 $mg \cdot L^{-1}$ total dissolved solids (TDS) in the hydrologically active zone (Oetting et al., 1996; Groschen and Buszka, 1997). The salinity increases down-dip of the interface (Oetting et al., 1996). The BFZ consists of many faults that produce fluid flow barriers and/or conduits (Maclay and Small, 1983). The faults that produce fluid flow barriers produce a result of compartmentalization of waters (Groschen and Buszka, 1997). Six geochemical zones (to be discussed later) exist within the saline-water zone, which reflect the regional variation among the flow paths (Oetting et al., 1996) and the compartmentalization of the waters (Groschen and Buszka, 1997).

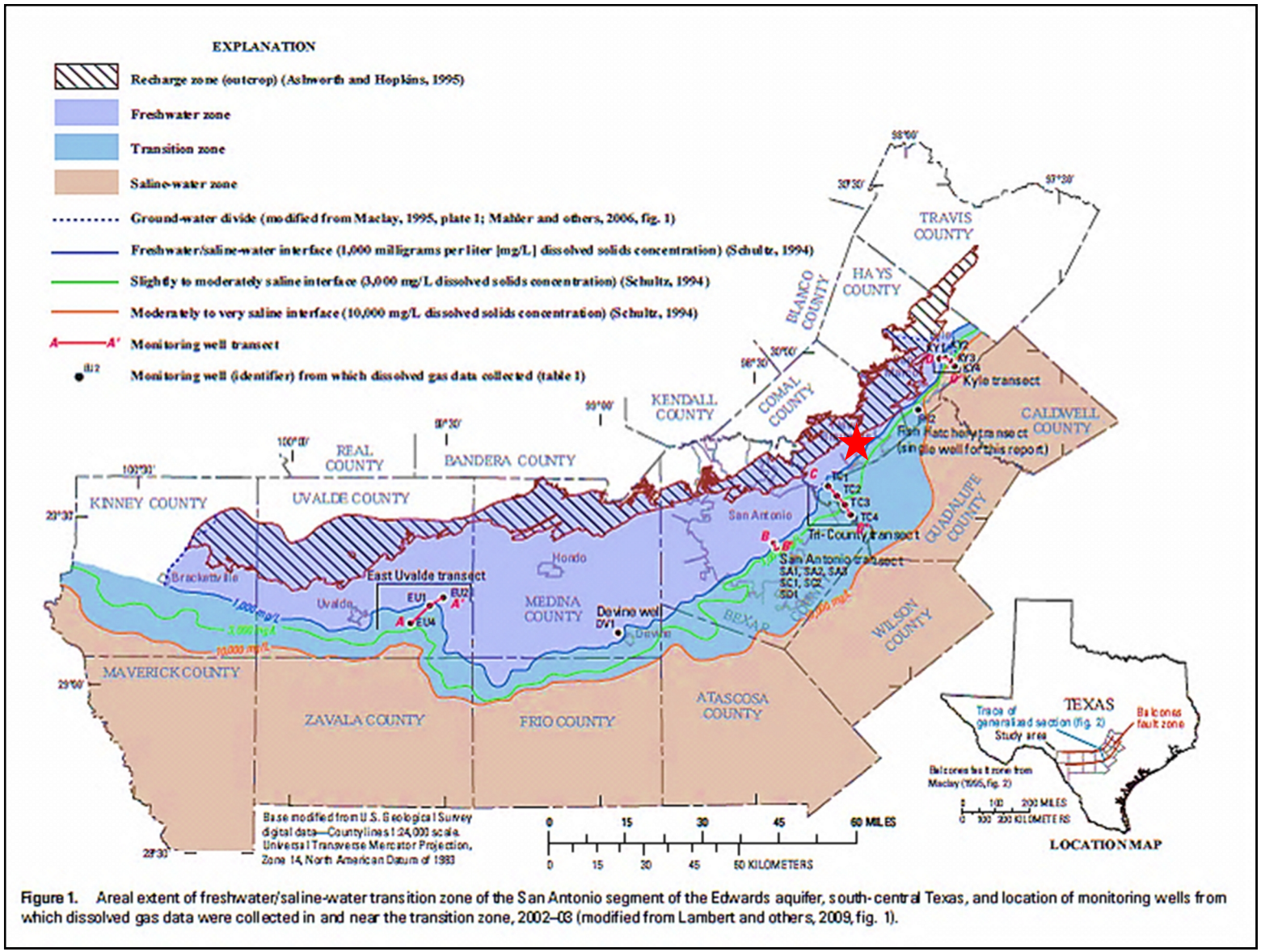

Figure 1. Areal extent of freshwater/saline-water transition zone of the San Antonio segment of the Edwards aquifer, south-central Texas, and location of monitoring wells from which dissolved gas data were collected in and near the transition zone, 2002–03 (modified from Lambert and others, 2009, fig. 1).

Figure 3. The arcuate transect of the freshwater/saline-water interface throughout the Edwards aquifer. The red star denotes the location of New Braunfels. Image source: Hunt et al., 2010.

GEOLOGIC BACKGROUND

STRATIGRAPHY

The stratigraphy of the Edwards aquifer comprises all or part of seven sedimentary formations: the Kainer, Person, and Georgetown formations in the eastern region (San Marcos Platform), the Devils River formation in the central region (Devils River Trend), and the West Nueces, McKnight and Salmon Peak formations in the western region (Maverick Basin) (Figure 4) (Maclay and Small, 1983; Maclay and Small, 1984; Groschen and Buszka, 1997). Each formation that comprises the Edwards aquifer is either a limestone or dolostone (Groschen and Buszka, 1997). Diagenesis has converted much of the dolostone in the freshwater zone into calcic limestone (Groschen and Buszka, 1997). However, in the saline-water zone, minimal diagenesis has been observed, so the formations have retained much of its dolostone (Groschen and Buszka, 1997). The Kainer formation is approximately 100 m thick and is subdivided into four units: a basal, nodular wackestone unit, a dolomitic member consisting of dolomitized wackestone, an evaporite unit (Kirschberg evaporite), and an uppermost grainstone unit (Maclay and Small, 1984; Groschen and Buszka, 1997). The Person formation is approximately 55 m thick and is subdivided into five units: a basal, shaly mudstone unit, a leached and collapsed unit containing breccia and wackestone, and a cyclic, uppermost unit containing rudist-bearing wackestone and shell-fragmented grainstone (Maclay and Small, 1984; Groschen and Buszka, 1997). For much of the uppermost unit in the San Marcos Platform, an erosional disconformity is present (Groschen and Buszka, 1997). The Georgetown formation has a thickness range from 25 m to 80 m thick and is almost completely eroded (Maclay and Small, 1984; Groschen and Buszka, 1997).

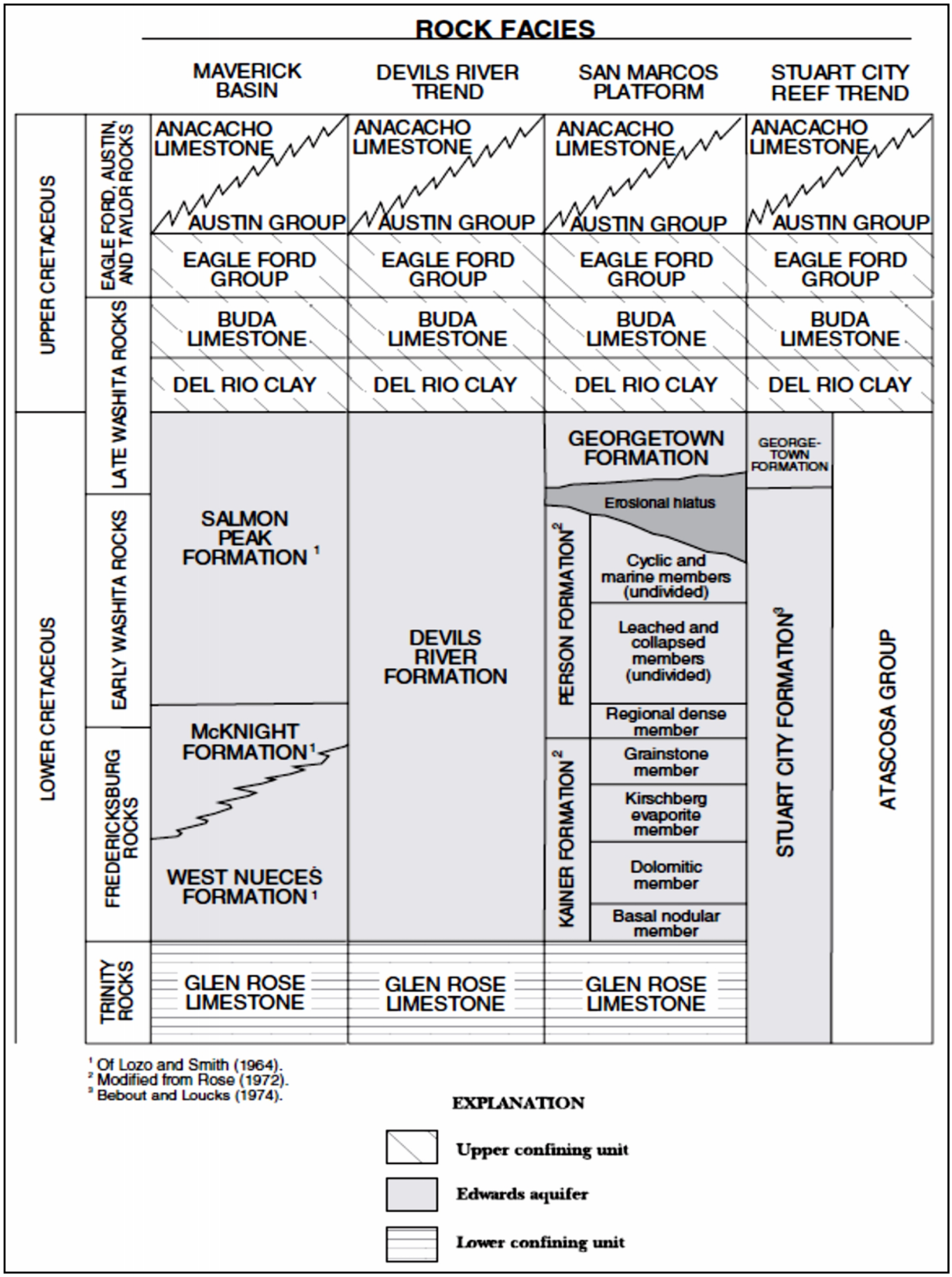

Figure 4. Correlations between hydrostratigraphic units of the Edwards aquifer. Image source: Groschen and Buszka, 1997.

The Devils River formation, part of the Devils River Trend, is associated with the same stratigraphic interval as those formations in the San Marcos Platform but lacks consistent subdivision markers (Groschen and Buszka, 1997). The Devils River formation is approximately 160 m thick, with 21 m of basal, shaly limestone, 70 m of wackestone and mudstone, 12 m of mudstone and breccia, and 60 m of rudist-bearing wackestone and grainstone (Maclay and Small, 1984; Groschen and Buszka, 1997). In the Maverick Basin, the West Nueces, McKnight, and Salmon Peak formations make up the western region of the aquifer (Maclay and Small, 1984; Groschen and Buszka, 1997). The West Nueces formation consists of two subdivisions: an 18 m thick basal, shaly limestone unit, and a 24 m thick wackestone and grainstone unit (Maclay and Small, 1984; Groschen and Buszka, 1997). The McKnight formation consists of three subdivisions: a 21 m thick mudstone and grainstone unit interbedded with breccia, an 8 m thick clayey, lime mudstone unit, and a 17 m thick uppermost mudstone and evaporite unit (Maclay and Small, 1984; Groschen and Buszka, 1997). The Salmon Peak formation consists of two subdivisions: a 90 m thick basal, massive, lime mudstone unit, and a 23 m thick uppermost grainstone unit (Maclay and Small, 1984; Groschen and Buszka, 1997).

The stratigraphic unit below the Edwards aquifer group is the Glen Rose Limestone formation, which is approximately 365 m thick (Maclay and Small, 1984; Groschen and Buszka, 1997). The Glen Rose Limestone consists of limestone and dolostone in its basal section and calcareous shale, limestone, and dolostone in the upper section (Maclay and Small, 1984; Groschen and Buszka, 1997). The stratigraphic unit above the Edwards aquifer is the Del Rio Clay (Maclay and Small, 1984; Groschen and Buszka, 1997). The Del Rio Clay is a predominantly argillaceous, calcareous shale that ranges from 3 m to 18 m in thickness (Maclay and Small, 1984; Groschen and Buszka, 1997). The Glen Rose Limestone and Del Rio Clay are the confining units for the Edwards aquifer (Oetting et al., 1996).

The Stuart City formation is also a part of the Edwards aquifer stratigraphy and was deposited contemporaneously with the Edwards Group (Kainer and Person formations), West Nueces, McKnight, and Salmon Peak formations, and the Devils River formation (Groschen and Buszka, 1997). The Georgetown formation was deposited on top of the Stuart City formation (Groschen and Buszka, 1997). The formation is a mixture of reefal and grainstone deposits and has a thickness range of 610 to 760 m (Groschen and Buszka, 1997).

Some of the strata have been intruded by igneous rocks, mainly basalt, due to locally formed volcanoes (Lindgren et al., 2004). The volcanic activity, concentrated in Uvalde County, occurred after deposition of the strata that comprise the Edwards aquifer (Lindgren et al., 2004). The basalt intruded as plugs, dikes, and sills contemporaneously with the deposition of the Anacacho Limestone and Austin Chalk during the late Upper Cretaceous (Lindgren et al., 2004). Most of the basalt has been altered to serpentinite, due to hydrochemical alterations (Oetting et al., 1996; Lindgren et al., 2004).

STRUCTURE

There are three major regional structural features affecting the hydrology of the Edwards aquifer (Lindgren et al., 2004). These features include the Llano uplift, the Ouachita structural belt, and Balcones Fault Zone (BFZ) (Lindgren et al., 2004). The Llano uplift is pre-Cambrian in age, with metamorphic and plutonic rocks exposed in its core (Lindgren et al., 2004). The San Marcos arch is the subsurface extension of the Llano uplift and is a broad anticline that plunges southeast (Lindgren et al., 2004). The Ouachita structural belt is a compressional belt that originated in the late Paleozoic and was subsequently buried under Mesozoic and Cenozoic strata (Lindgren et al., 2004). The location of the Llano uplift, Ouachita structural belt and Balcones Fault Zone are shown in Figure 5.

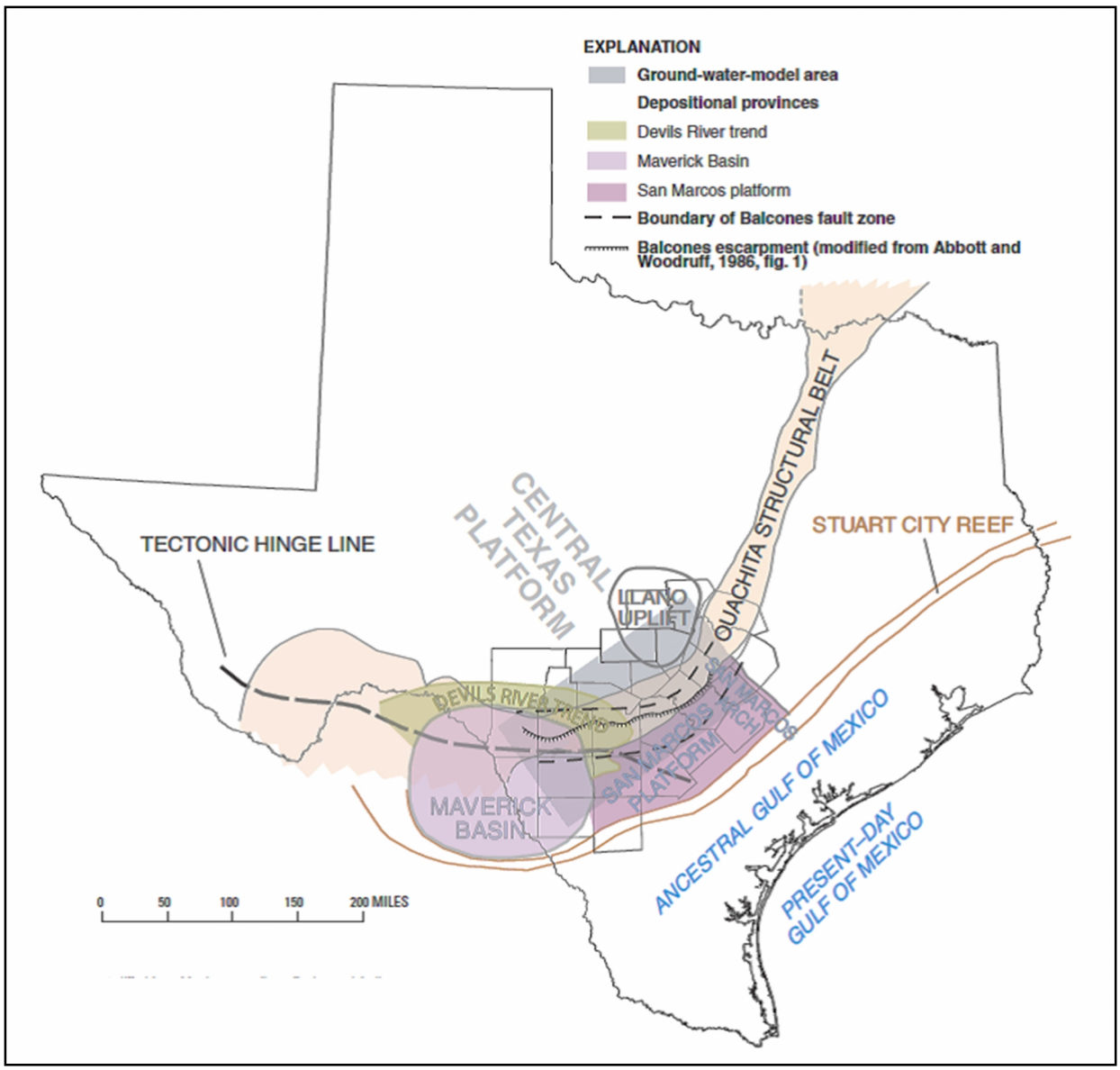

Figure 5. An illustration of the structural complexities of the Edwards aquifer. Image Source: Lindgren et al., 2004.

The BFZ is the most important of the three structural features because the BFZ consists of many faults that produce fluid flow barriers and/or conduits within the aquifer (Maclay and Small, 1983). The BFZ is a broad en echelon system of normal faults that trends north-northeast in an arcuate transect which spans most of south-central Texas (Lindgren et al., 2004; Ferrill et al., 2004). The BFZ has a width range between 25 km and 30 km, with a maximum displacement of 366 m for the Comal Springs fault (Ferrill et al., 2004). The normal faults within the BFZ tend to mostly dip

southeast toward the Gulf of Mexico (Lindgren et al., 2004; Ferrill et al., 2004). However, the normal faults modeled in New Braunfels are antithetic to the Comal Springs fault and dip northeast (Ferrill et al., 2004). Figure 6 shows an analog structural model within the Edwards aquifer (Ferrill et al., 2011). The evidence for faulting for each well in the New Braunfels transect comes from wireline log interpretation (Lindgren et al., 2004; Roberto Esquilin, written commun. 2012). The BFZ represents the separation between the flat Edwards Plateau and the coastward-dipping Gulf Coast Plain that extends to the Gulf of Mexico (Loáiciga et al., 2000; Ferrill et al., 2004). Most of the uplift responsible for creating the BFZ occurred during the Miocene (Ewing, 1991). A cross section of the BFZ, along with the Edwards Plateau and Gulf Coastal Plain is shown in Figure 7.

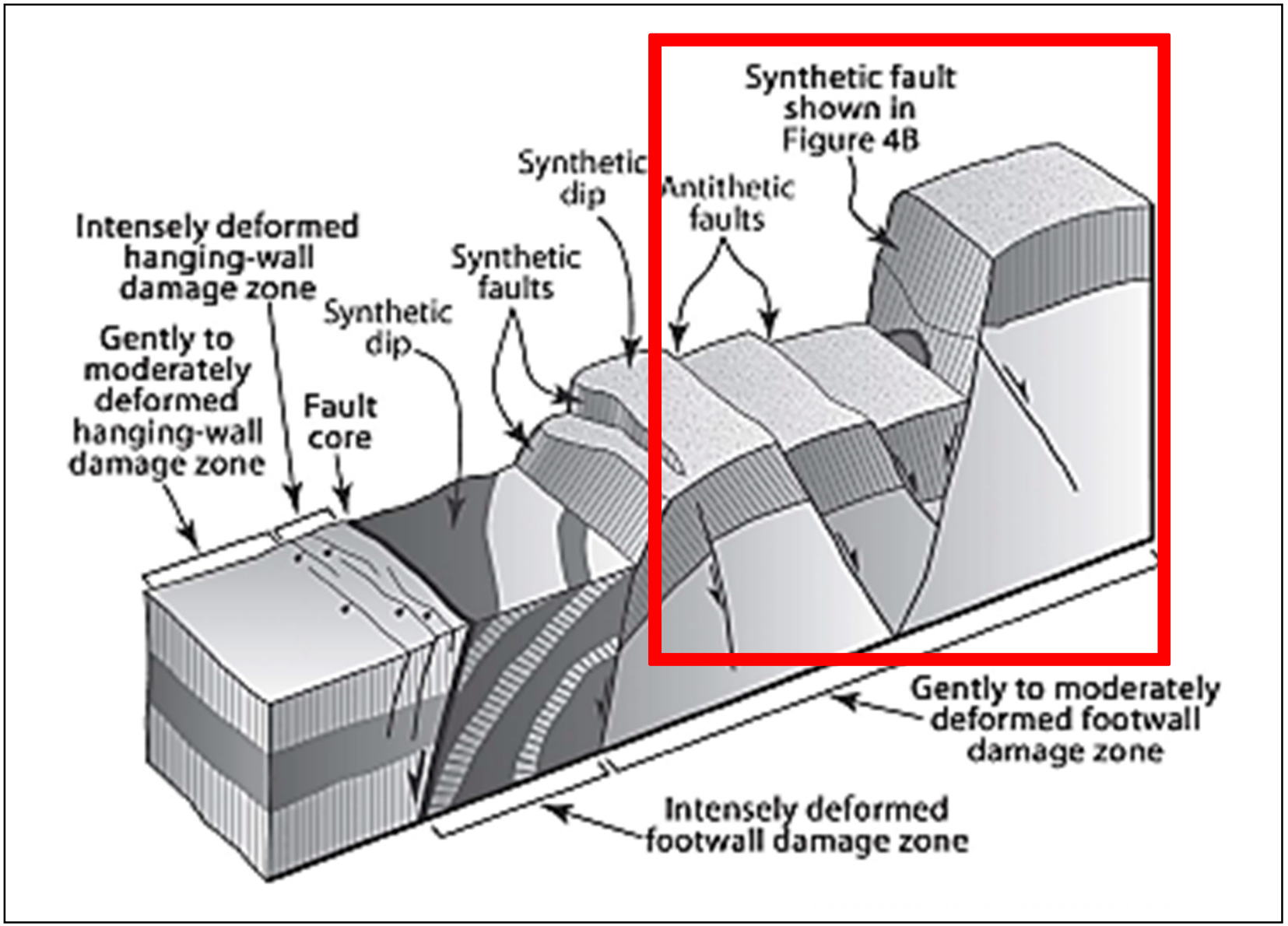

Figure 6. A block diagram showing elements of a fault zone, with antithetic and synthetic faults highlighted in red. Image source: Ferrill et al., 2011.

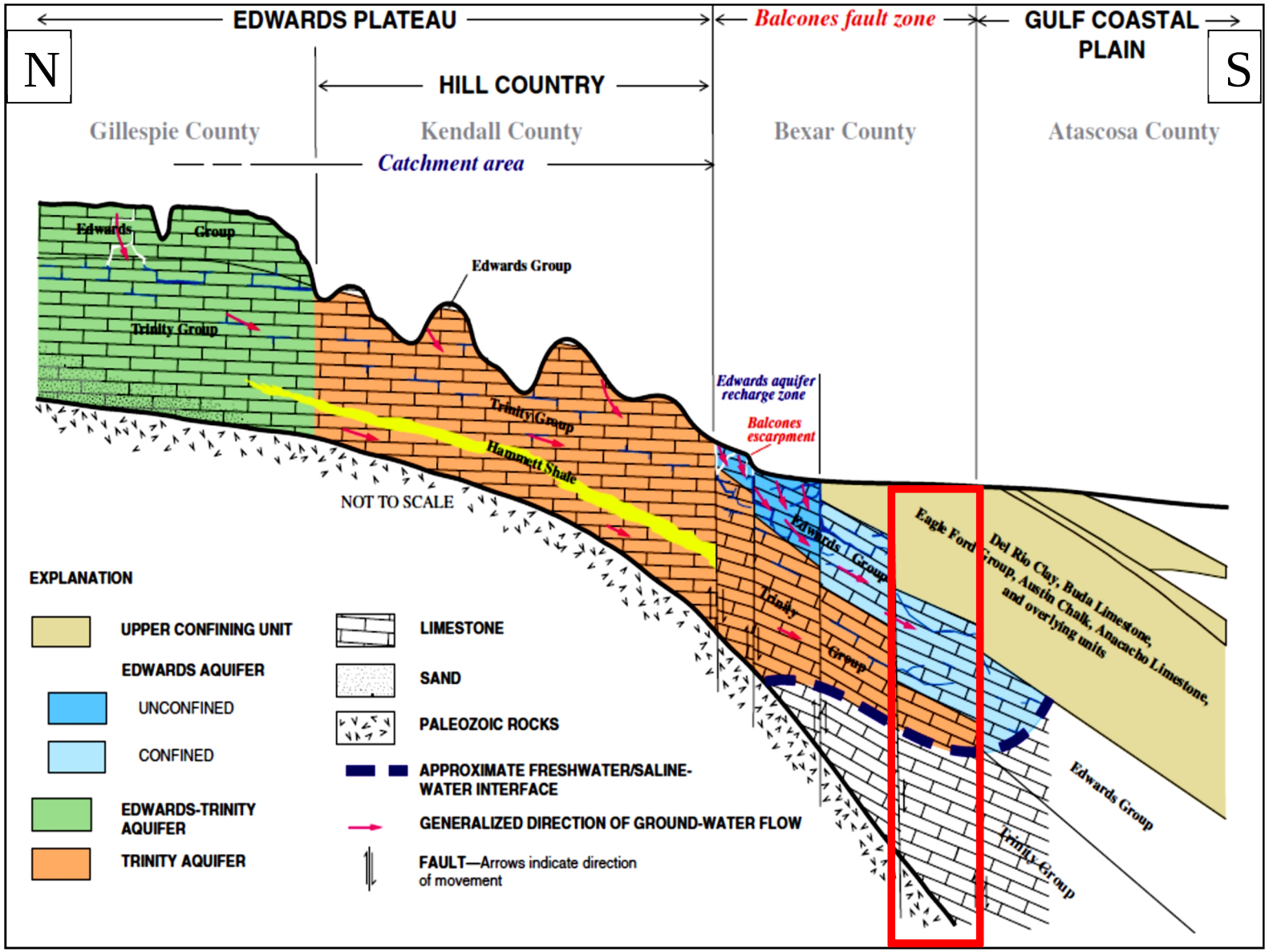

Figure 7. A generalized cross-section of the Edwards aquifer. The red box indicates the area that is confined and has the most horizontal stratigraphy, correlating to New Braunfels, TX. Image source: Lindgren et al. 2004.

HYDROLOGIC FRAMEWORK

As a result of diagenesis converting dolostone into calcic limestone during de-dolomitization, large effective porosity and large transmissivity results in the freshwater zone of the Edwards aquifer (Groschen and Buszka, 1997). Transmissivity associated with the freshwater zone near the freshwater/saline-water interface is as high as 190,000 $m^2 \cdot d^{-1}$ (Groschen and Buszka, 1997). Because little diagenesis has occurred in the saline-water zone, lower effective porosities and transmissivities are associated with the saline-water zone (Groschen and Buszka, 1997). Effective porosity in the saline-water zone is less than 10% and transmissivity is approximately 1,000 $m^2 \cdot d^{-1}$ (Groschen and Buszka, 1997). Permeability is two to three orders of magnitude lower in the saline-water zone than in the freshwater zone (Groschen and Buszka, 1997). Due to these factors, the residence time of waters in the saline-water zone is significantly longer than in the freshwater zone (Groschen and Buszka, 1997).

Groundwater flow can be divided into three sections for the Edwards aquifer: the catchment zone in the Edwards Plateau, the recharge zone, and the confined zones (Figure 8) (Lindgren et al., 2004). Discharge occurs via springflow and withdrawal by wells (Lindgren et al., 2004). The sedimentary rocks that make up the Edwards aquifer are exposed in the Edwards Plateau, where the Edwards and Trinity aquifers receive direct recharge to the water table (Lindgren et al., 2004). The recharge zone is unconfined and receives direct recharge to the water table (Lindgren et al., 2004). Recharge into the freshwater zone via meteoric water is approximately 790 million $m^3 \cdot yr^{-1}$ (Groschen and Buszka, 1997). Only about 10% of the recharge actually enters the saline-water zone as meteoric water (Groschen and Buszka, 1997). The confined zones comprise the freshwater and the interface between the freshwater/saline-water zones (Lindgren et al., 2004).

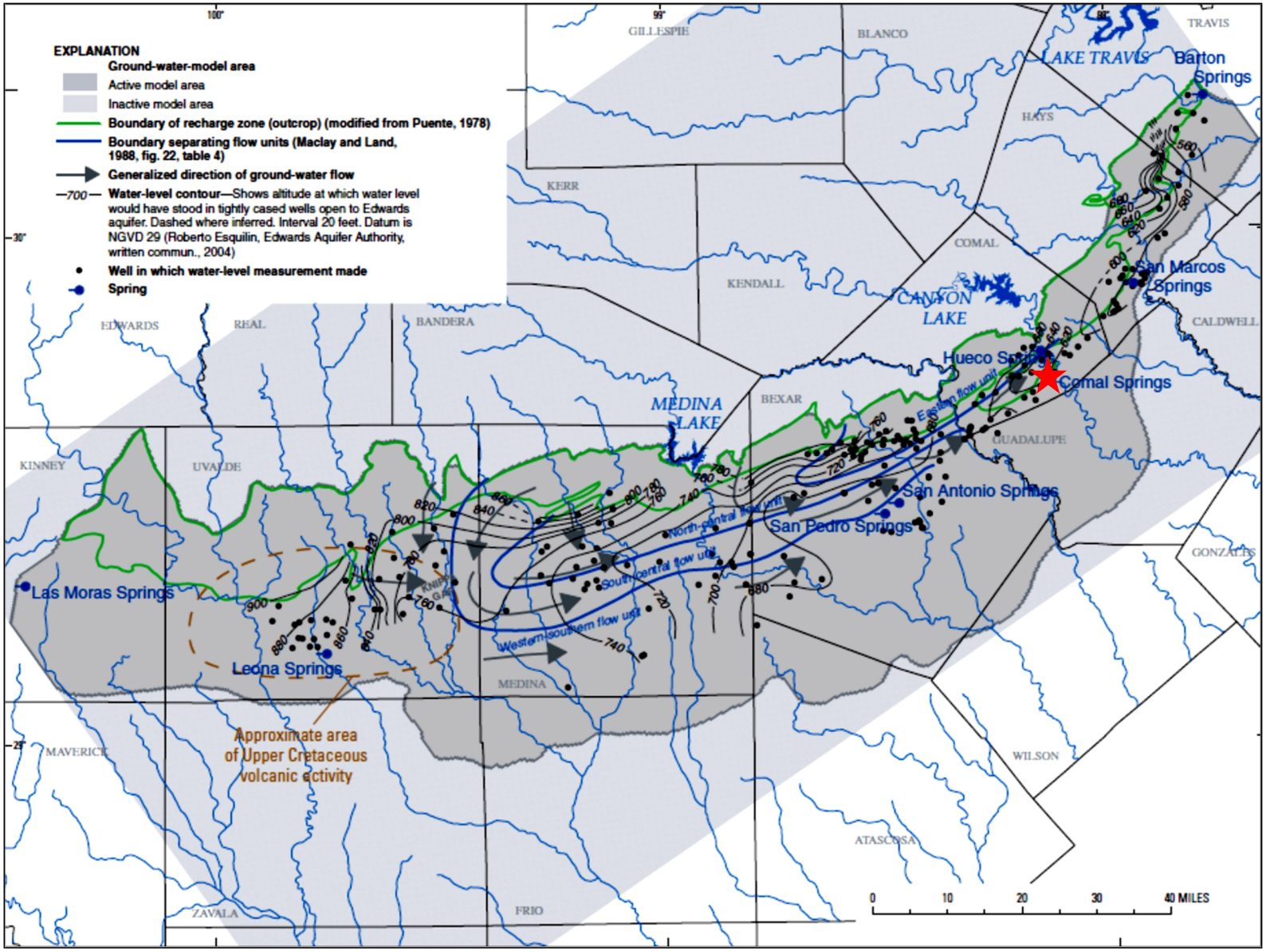

Figure 8. The measured potentiometric surfaces and computed flow paths for the Edwards aquifer (west to east). The red star denotes New Braunfels. Image Source: Lindgren et al., 2004

KARSTIFICATION OF THE EDWARDS AQUIFER

Karst develops out of the dissolution of soluble carbonate rocks, which produces a heterogeneous system of conduits that allow fluids to flow down gradient (Lindgren et al., 2004). Karst aquifers are dual-flow systems with Darcian flow in porous media and turbulent flow in conduits (Lindgren et al., 2004). The controlling factors responsible for the development of karst and increased permeability in carbonate aquifers are climate, topography, sea level, regional structure, presence of soluble rocks, nature of subsurface flow, and the condition of the carbonate rocks at the surface that are exposed to meteoric waters (Stringfield et al., 1979). Surface conditions are important also because the initiation of karstification in carbonate aquifers is more favorable with a layer of soil or a relatively permeable, less soluble confining unit above the carbonate rocks than just bare carbonate rocks exposed at the surface (Stringfield et al., 1979). This allows the meteoric waters to percolate downward to the carbonate rocks instead of surficially running off (Stringfield et al., 1979).

The development of the Edwards aquifer is owed to several episodes of karstification that resulted in paleokarst features (Oetting et al., 1996; Lindgren et al., 2004). Subaerial exposure and relative sea level fall during the late Cenozoic can be attributed to the development of the Edwards paleokarst features (Lindgren et al., 2004). The sediments were originally composed of calcite, aragonite, dolomite, and gypsum and have undergone dissolution and dedolomitization to produce a highly porous and heterogeneous limestone aquifer (Lindgren et al., 2004). Deike (1990) suggests, based on dolomite dissolution rates, that mixing between meteoric waters and brine-filled pre-aquifer units formed a major part of the Edwards aquifer during the Holocene (~11,000 years B.P.). Calculations for the rate of dolomite dissolution during the formation of the Edwards aquifer range from 10^{-13} to 10^{-14} mmol dolomite $cm^{-2} \cdot s^{-1}$ (Deike, 1990).

According to Fleury et al. (2007), there are three classifications for karst aquifers, based on the degree of karstification and access to the sea: (1) poorly developed karstification, (2) well-developed karstification below sea level and open to the sea, and (3) well-developed karstification below sea level, partially or totally closed to the sea. In the last classification, these aquifers have undergone several episodes of karstification, so the degree of karstification is great (Fleury et al., 2007). Stringfield et al. (1979) classifies karst aquifers into three classifications as well but by organizing the aquifers into their capacities to hold water, which serves as proxy for the degree of karstification. The Stringfield et al. (1979) classification scheme is as follows: (1) aquifers with low yield of water to wells, (2) aquifers with low to intermediate yields of water for springs and wells, and (3) aquifers with intermediate to very large yields of water for springs and wells. The most productive karst aquifers are those that fall into categories two and three for Fleury et al. (2007) and into category three for Stringfield et al. (1979). The Edwards aquifer falls into the last category of each classification scheme (Stringfield et al., 1979; Fleury et al., 2007). Therefore, the Edwards aquifer is the fourth most productive aquifer in the United States behind the Floridan and Biscayne aquifers in Florida and the Ozark aquifer in Missouri (Stringfield et al., 1979).

DENSITY DRIVEN MODELS FOR SALINE WATER INTRUSION

The extent of saline water intrusion into freshwater karst aquifers, both coastal and continental, is a function of density differences. Freshwater has a density of 1000 $kg \cdot m^{-3}$ (Essaid, 1986), where seawater has a density range between 1022 $kg \cdot m^{-3}$ to 1028 $kg \cdot m^{-3}$, with an average of 1025 $kg \cdot m^{-3}$ (Fleury et al., 2007). When saline water intrudes karst aquifers via conduits (both from natural dissolution of the carbonate or from faults), a saline water wedge occurs beneath the freshwater (Essaid, 1986; Fleury et al., 2007). Badon-Ghyben (1889) and Herzberg (1901) both, independently, found the relationship that governs freshwater that resides above a saline water wedge (Essaid, 1986). The position of the saline water wedge is defined as the pressure equilibrium at the interface between two fluids of differing densities (Essaid, 1986; Fleury et al., 2007). An assumption is made that the interface is sharp, i.e. immiscible fluids, (Essaid, 1986) and that the freshwater is mobile, while the saline water is immobile (Fleury et al., 2007). The resultant Ghyben-Herzberg formula predicts the location of the interface of the saline water wedge (Essaid, 1986; Fleury et al., 2007). The Ghyben-Herzberg formula is as follows:

$$\text{Equation 1: } \rho_s \cdot g \cdot z = \rho_f \cdot g \cdot (z \cdot h_f)$$

where ρ_s is the density of the saline water; ρ_f is the density of freshwater; g is gravitational acceleration ($g = 9.8\ m \cdot s^{-2}$); z is the interface depth below sea level; and h_f is the hydraulic head within the aquifer (Fleur et al., 2007). The formula, rearranged for interface depth, is as follows (Fleury et al., 2007):

$$\text{Equation 2: } z = (\rho_f \cdot h_f)/(\rho_s - \rho_f)$$

The primary factor controlling saline water intrusion is a difference in hydraulic head between the aquifer and saline water source (oceans, brines, etc.) (Fleury et al., 2007). Saline

water intrusion occurs when the hydraulic head for the saline water source is higher than that of the freshwater aquifer (Arfib et al., 2007; Fleury et al., 2007). In areas that have large populations dependent on karst aquifers, substantial freshwater pumping lowers the hydraulic head, increasing the possibility of intrusion (Fleury et al., 2007). To maintain the quality of groundwater inside these karst aquifers, the hydraulic head must remain above that of the saline water.

Density stratification is another mechanism that results in saline water intrusion (Fleury et al., 2007). In sub-horizontal conduits, density stratification occurs when freshwater flows out of the aquifer on top of saline waters that flow in, forming saline water wedge within the conduit (Fleury et al., 2007). The position of the wedge within the conduit is determined by the dimensions of the conduit and the outflow rate (Fleury et al., 2007). The saline water wedges formed inside these sub-horizontal conduits are smaller scale than those produced by differences in hydraulic head. In addition, another mechanism that results in saline water intrusion is when conduits that develop at depth cross the saline water zone of contamination in the micro-fissures of the matrix (Fleury et al., 2007). Hydraulic head, again, controls the exchanges between the conduit and the matrix (Fleury et al., 2007).

METHODS

BASIN2 INTRODUCTION

Basin2 (Bethke et al., 2007) was used to simulate various fluid flow scenarios. Basin2 is a variable density numerical model that can trace steady-state or transient fluid flow through sedimentary basins (Bethke et al., 2007). In order to run differing hydraulic cases, several variable parameters were required. The most important parameters included fault permeability, aquifer rock permeability and porosity, and fluid density. To be discussed in greater detail later, these parameters affect each hydraulic scenario in different ways and are important to the goals of this research. Figure 9 shows the first physical model that was produced with no flow fields, color maps, or contours. The Edwards aquifer units are highlighted in light blue, the Del Rio Clay formation is highlighted in gray, and the potentiometric surface is highlighted in the dashed dark blue line. The transect of wells used in New Braunfels, Texas is shown in Figure 10.

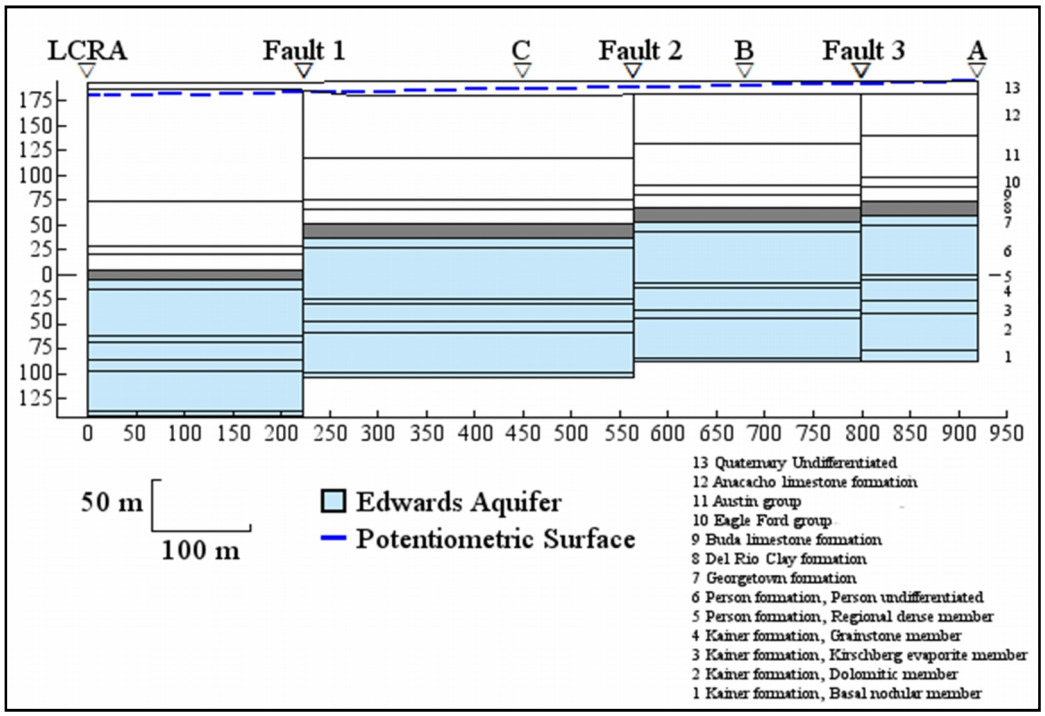

Figure 9. The physical model for the New Braunfels transect, showing the Edwards aquifer units, upper confining unit, and the potentiometric surface used to drive fluid flow.

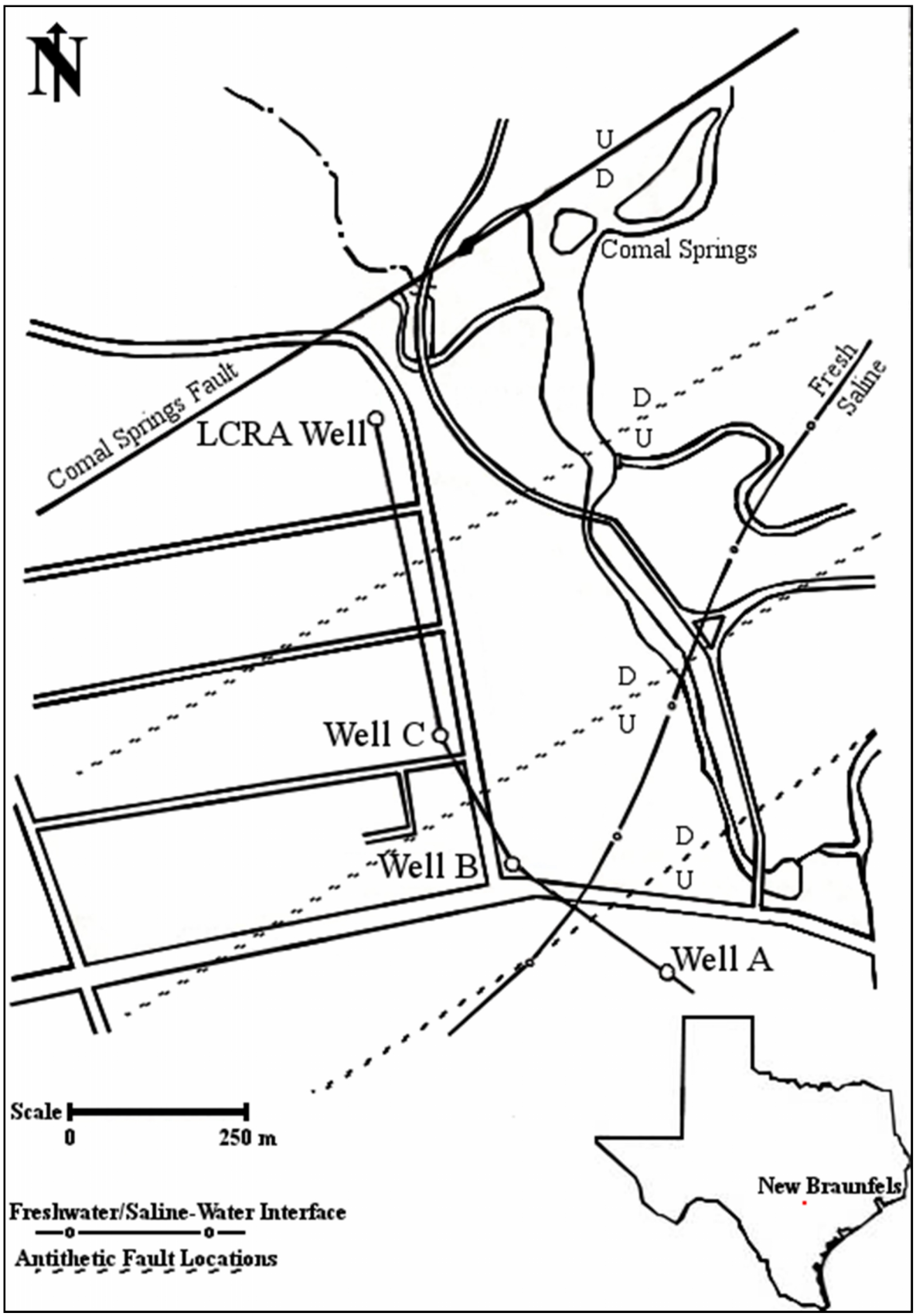

Figure 10. The transect of wells used in this study. Image modified from Schindel et al., 2005.

TRANSECT & WELL LOG DATA

A trip to the Edwards Aquifer Authority (EAA) was completed in August, 2011 to determine the most appropriate set of wells that transect the Edwards Aquifer freshwater/saline-interface and gather data on those wells. The New Braunfels EAA transect was chosen due to favorable locations of each well in relation to the interface (i.e., a good distribution of wells in the saline and mixing zones) and the wealth of geophysical well log data compared to other transects owned by the EAA. The transect contains five observation wells: DX-68-23-616 (A) (saline), DX-68-23-617 (B-1) (mixed), DX-68-23-618 (B-2) (mixed), DX-68-23-619 (C) (mixed), and DX-68-23-304 (LCRA) (mixed). B-2 was not used because it did not penetrate the entire aquifer stratigraphy, its extreme proximity to B-1, and its lack of geophysical well logs for interpretation. For wells A, B, C, and LCRA, geophysical well logs and geochemical data were collected from the EAA (Figures 11, 12, 13, and 14, respectively). The well logs collected from the EAA for wells A, B, and C include gamma ray, resistivity (short and long normal), fluid temperature, fluid resistivity, and, density. However, the LCRA well does not have fluid temperature and fluid resistivity well logs. This set of observation wells was drilled by Texas Water Wells for the Edwards Underground Water District (now Edwards Aquifer Authority) and logged by the United States Department of the Interior Geological Survey Water Resources Division. Faults are assumed vertical in this transect due to limitations of Basin2. In addition, there is no way of determining dip of the faults from well log data.

DX-68-23-616

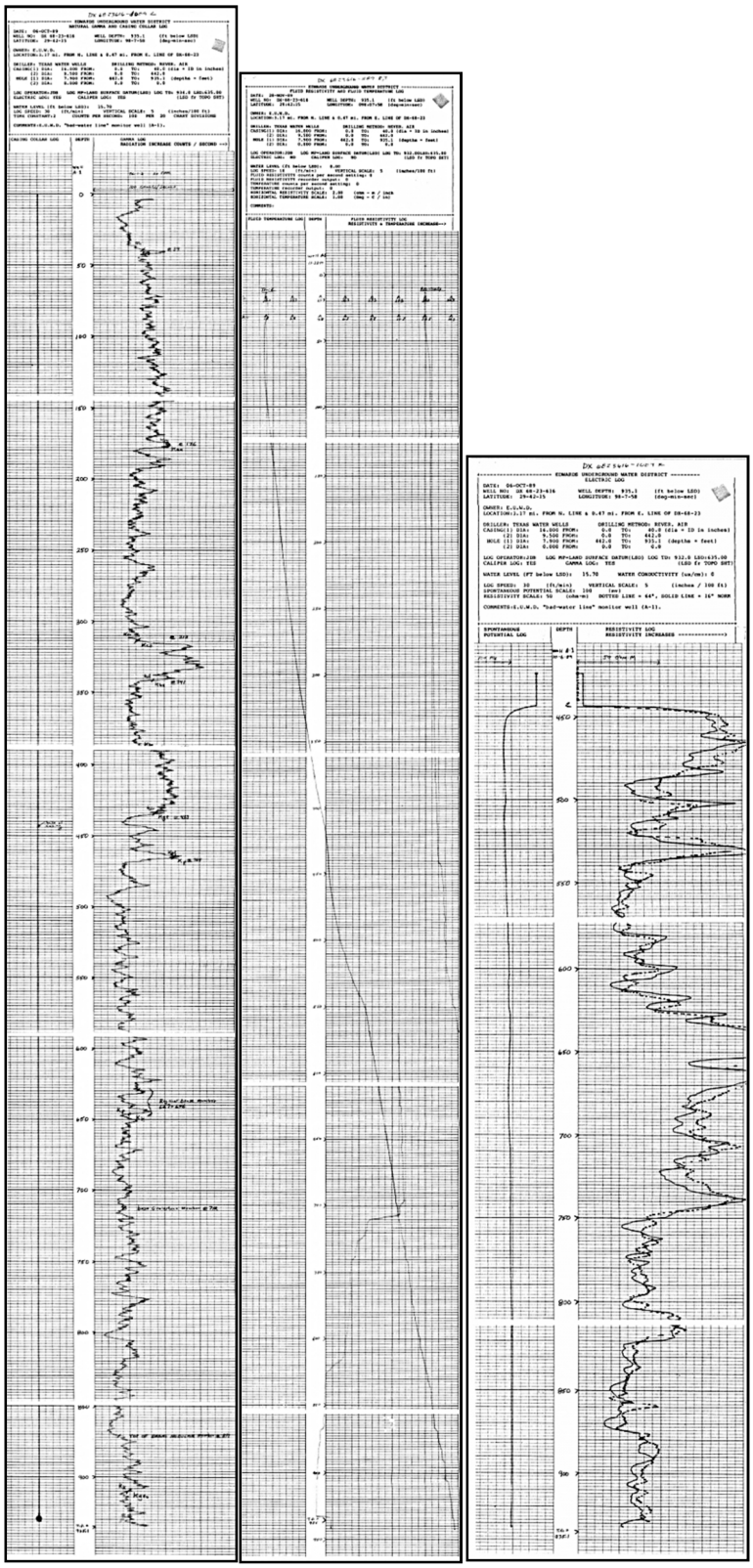

Figure 11. Well log response for Well A. Gamma ray is on the left, fluid temperature and resistivity is in the center, and bulk resistivity and caliper is on the right.

DX-68-23-617

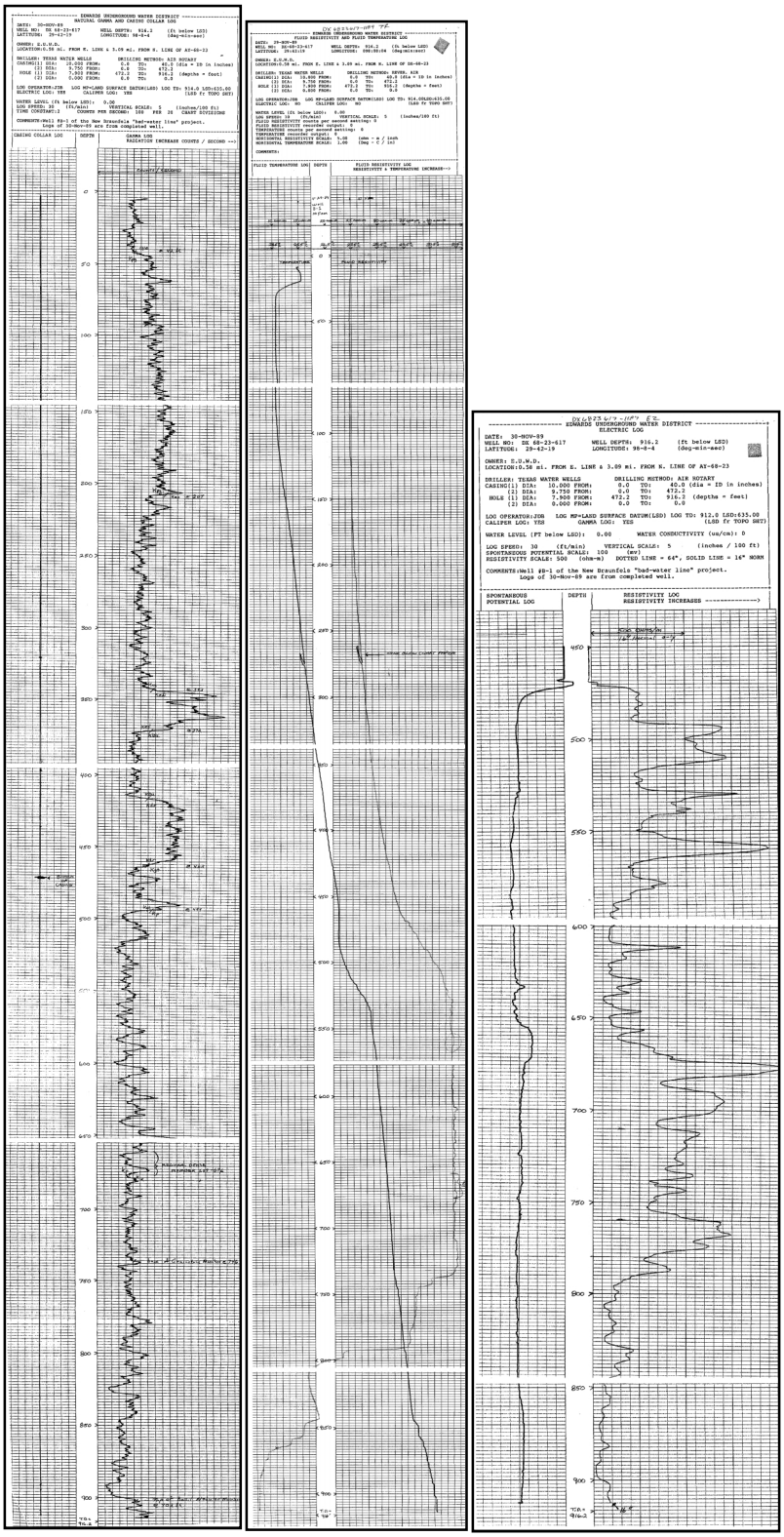

Figure 12. Well log data for Well B. Gamma ray is on the left, fluid temperature and resistivity is in the center, and bulk resistivity and caliper is on the right.

DX-68-23-619

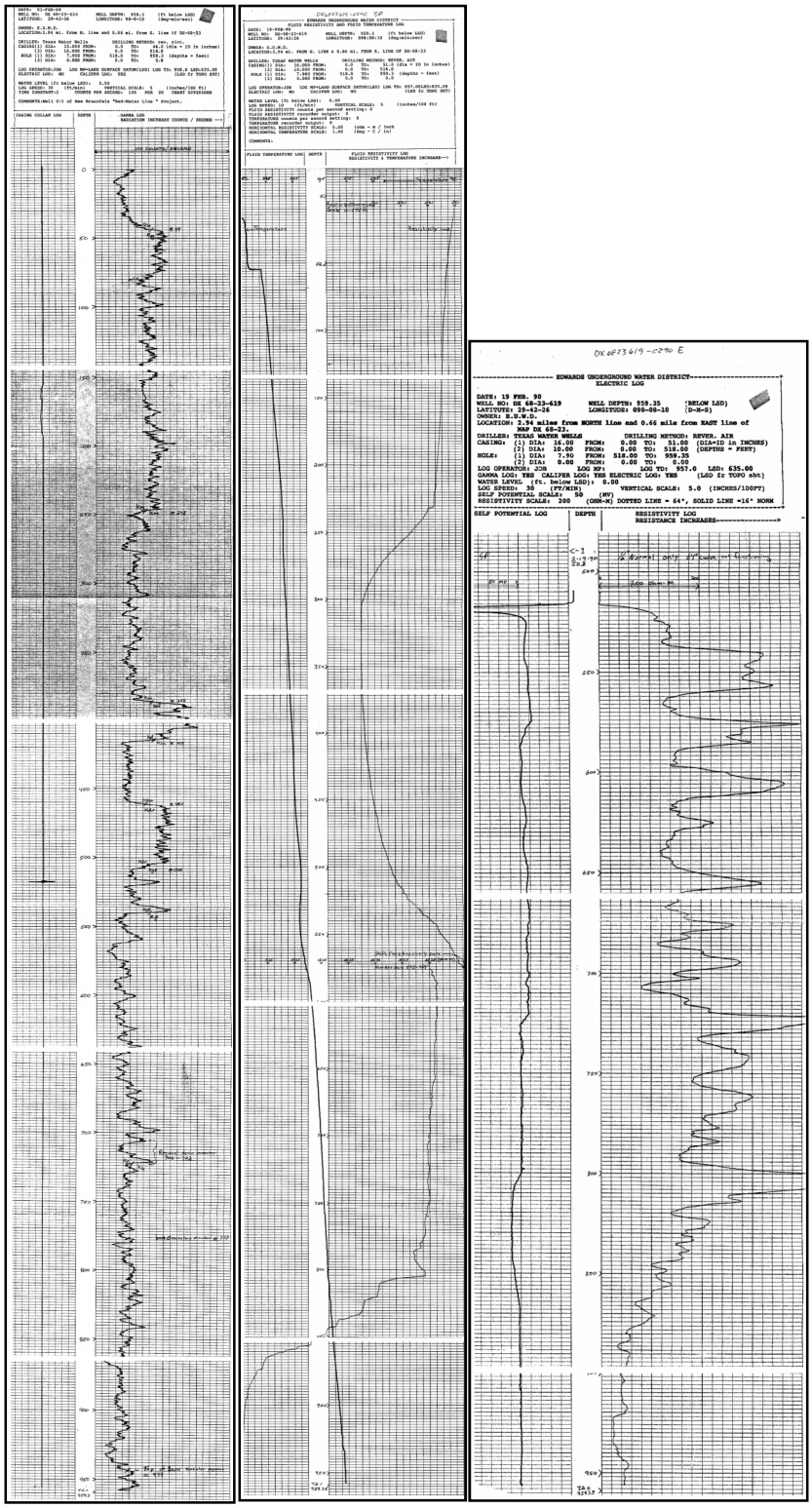

Figure 13. Well log data for Well C. Gamma ray is on the left, fluid temperature and resistivity is in the center, and bulk resistivity and caliper is on the right.

DX-68-23-304

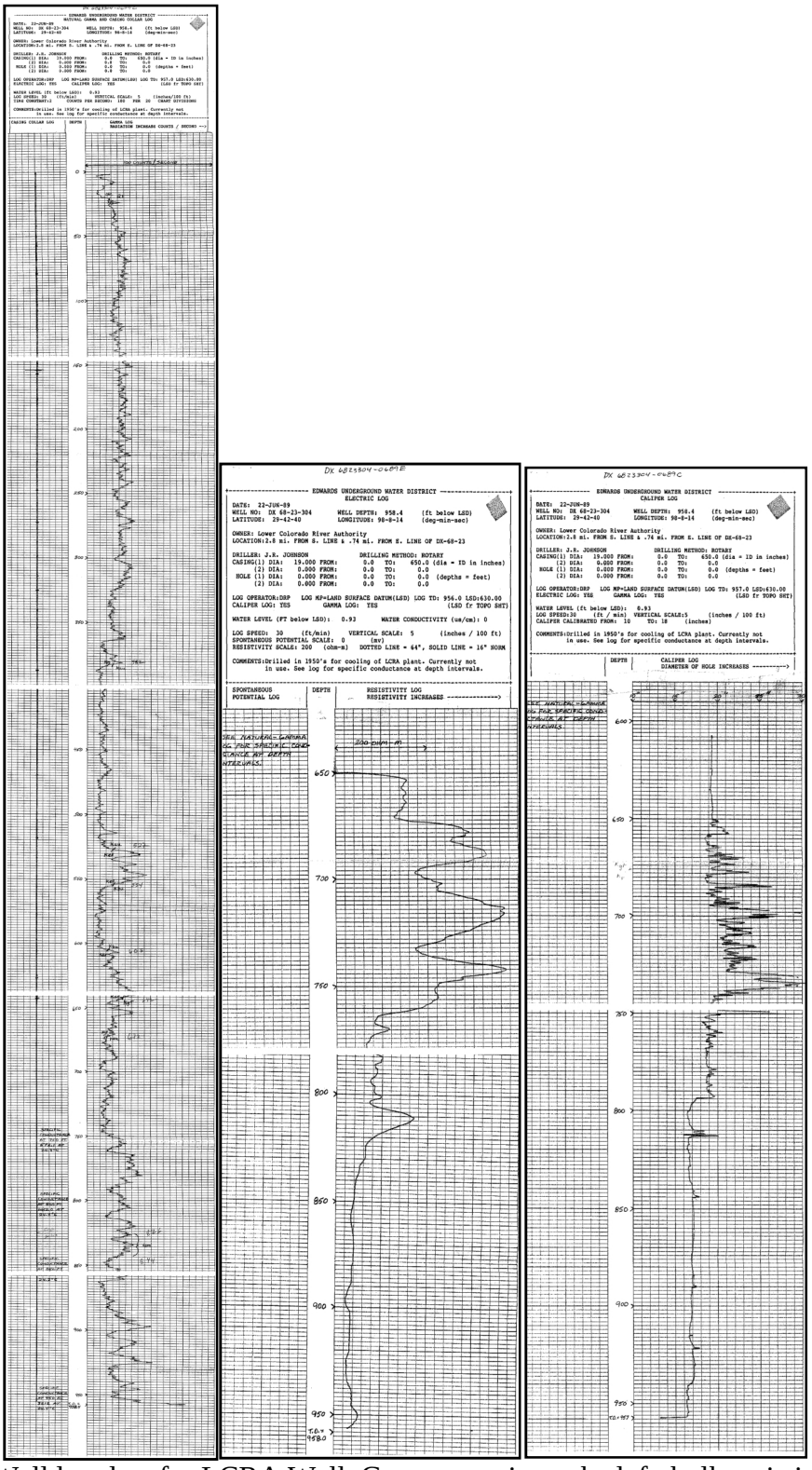

Figure 14. Well log data for LCRA Well. Gamma ray is on the left, bulk resistivity is in the center, and caliper is on the right.

DETERMINATION OF PARAMETERS

Packer tests were performed in fifty feet intervals on wells A, B, and C by Hovorka et al. (1995) (Figures 2, 9, and 10). Hydraulic conductivities from the packer tests permit determination of intrinsic horizontal permeability for each interval. Intrinsic horizontal permeability is related to hydraulic conductivity by:

$$\text{Equation 3: } k = (K \cdot \mu)/(\rho_{fl} \cdot g)$$

where: k is intrinsic horizontal permeability (m^2), K is hydraulic conductivity (m/s), μ is dynamic viscosity (Pa·s), ρ_{fl} is fluid density (kg/m^3), and g is gravity (m/s^2). Dynamic viscosities were attained by using a temperature-dependent relationship by Appelo and Postma (2005):

$$\text{Equation 4: } \mu = 10^{(-(1.37023\cdot(T-20)+8.36x10^{-4}\cdot(T-20)^2/(109+T))}$$

where: μ is dynamic viscosity (g/s·m) and T is temperature (°C). Dynamic viscosity was converted from g/s·m to Pa·s for use in equation 3. To determine an appropriate temperature for each interval, a single arithmetic average was required for equation 4. To ascertain an average temperature, fluid temperature well logs were scanned and digitized using the program Engauge Digitizer (Mitchell, 2002). Engauge Digitizer is software that converts data points on image files into numbers (Mitchell, 2002). Prior to importing the scanned .tiff files into Engauge Digitizer, images were cropped into appropriate sections using the program GIMP (GNU Image Manipulation Program, version 2.6) (Kimball and Mattis, 2008), so that the program could run without crashing. Crashing occurred within Engauge Digitizer if the image file was too large. GIMP allowed scanned images to be straightened, darkened, and cropped. In Engauge Digitizer, three points are required to set the vertical and horizontal axis. The vertical axis was set using depth (m) and the horizontal axis was set using the temperature scale (°C). Once each axis was

set, points were plotted along the well log curve. Once the entire log section had been plotted, the data was imported into Microsoft Excel, where arithmetic averages were calculated and used in equation 4.

Fluid densities were attained by using fluid temperature (°C) and fluid resistivity (Ω·m) well logs. These logs were used to determine electrically equivalent NaCl salinity (mg/L) every 15.24 meters using Figure 15. Fluid densities were calculated as a function of temperature and salinity based on equation 5 by McCutcheon et al. (1993):

$$\text{Equation 5: } \rho_{fl} = \rho_0 + (A \cdot S) + (B \cdot S^{3/2}) + (C \cdot S^2)$$

where: ρ_{fl} is fluid density (kg/m^3) as function of temperature and salinity, ρ_0 is fluid density (kg/m^3) as function of temperature (°C) only, S is salinity (ppt), and A,B, and C are coefficients. $A = [(8.24493x10^{-1}) - (4.0899x10^{-3} \cdot T) + (7.6438x10^{-5} \cdot T^2) - (8.2467x10^{-7} \cdot T^3) + (5.3675x10^{-9} \cdot T^4)]$, $B = [(-5.724x10^{-3}) + (1.0227x10^{-4} \cdot T) - (1.6546x10^{-6} \cdot T^2)]$, $C = [4.8314x10^{-4}]$, and $\rho_0 = [10^3 \cdot (1-(T+288.9414)/(508929.2 \cdot (T+68.12963)) \cdot (T-3.9863)^2)]$ (McCutcheon et al., 1993). Salinity was converted from mg/L to ppt by dividing equivalent NaCl salinity determined in Figure 15 by 10^3 and was also arithmetically averaged for each interval. Once average fluid density, average fluid temperature, and viscosity were calculated for each flow test and packer test interval, intrinsic horizontal permeability was then calculated for each interval using equation 3. Calculations and Hovorka et al. (1995) data are shown in Table 1.

Because the stratigraphic formation thicknesses did not coincide with the 15.24 meter intervals chosen for the flow test and packer tests by Hovorka et al. (1995), an additional step was required to produce intrinsic horizontal permeability for each stratigraphic formations thickness. This was done by arithmetically averaging the interval permeability determined by

equation 3. These values are shown in Appendix A for each well. These new values for permeability now represented the stratigraphic formation intervals permeability and could be used in Basin2.

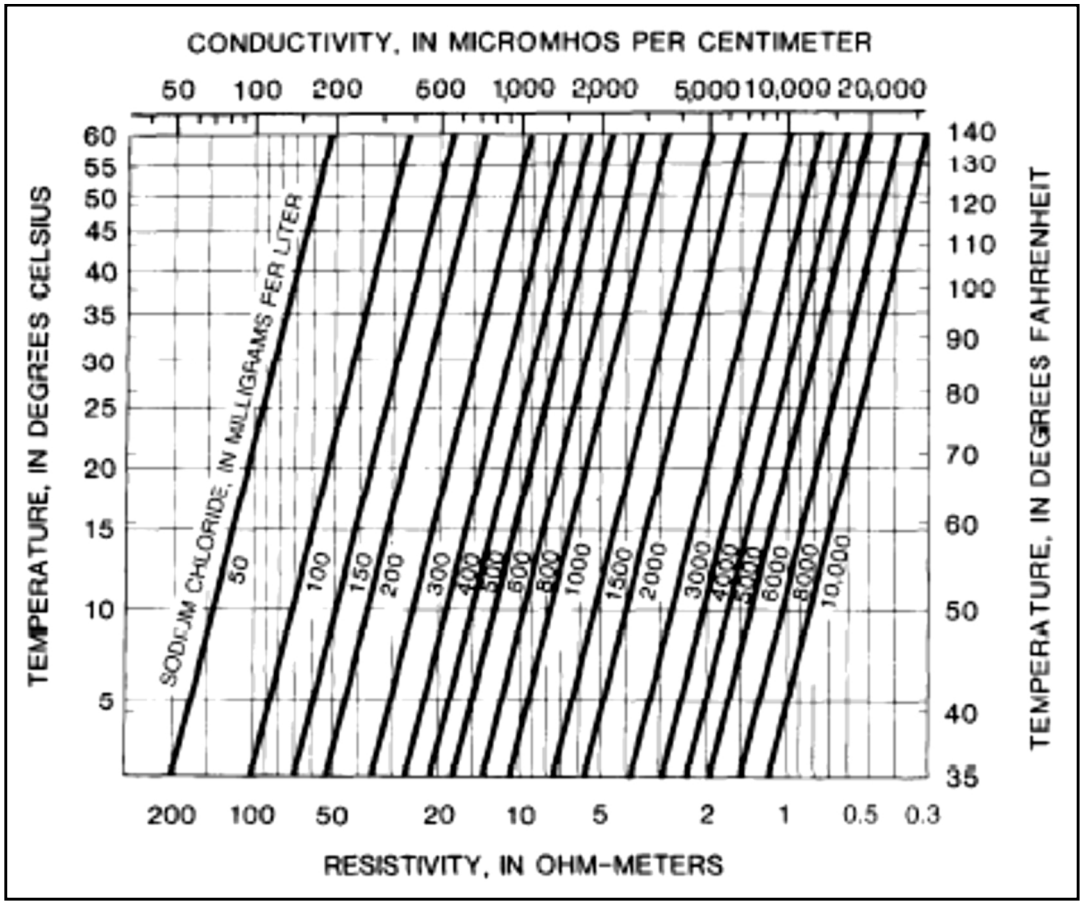

Figure 15. Cross-plot of electrically equivalent NaCl solution as a function of resistivity or conductivity and temperature. Image source: Keys, 1985.

Stratigraphic formation tops were picked using a combination of gamma ray and resistivity well log signatures. All logs are shown in Appendix E. For each well, all tops were recorded in Appendix A. All depth measurements were converted from English to metric. Gamma ray logs were also used to determine the fractional shale volume (V_{SH}), which was used for creating lithologies for Basin2. Determining the gamma ray index is the primary step in calculating percent volume shale. This relationship is shown by:

Equation 6: $I_{gr} = (GR_{log} - GR_{min})/(GR_{max} - GR_{min})$

where: I_{gr} is gamma ray index, GR_{log} is gamma ray reading of formation, GR_{min} is minimum gamma ray (cleanest carbonate reading), and GR_{max} is maximum gamma ray (shale reading) (Asquith and Krygowski, 2004). Cleanest carbonate reading refers to zones in the formation with little to no shale. For GR_{log}, a trend line was picked for each formation and used as the reading. I_{gr} was related to V_{SH} by equation 7, which is a relationship for rocks older than the 65.5 Ma (Paleogene) (Larionov, 1969) (Appendix A):

Equation 7: $V_{sh} = 0.33 \cdot (2^{2 \cdot Igr} - 1)$

Porosity was determined by using density porosity logs. Density porosity logs were chosen over sonic porosity and neutron porosity logs. Density derived porosity gives total porosity (primary and secondary), as does neutron because both are nuclear. However, no corrections were required with the density logs because they were logged with an assumed matrix of limestone, which has a matrix density of 2.71 g/cm^3 (Asquith and Krygowski, 2004). Several inaccuracies occur with sonic and neutron porosity logs in carbonates. Sonic logs measure the interval transit time of a compressional wave within a formation (Asquith and Krygowski, 2004). For sonic logs, only primary porosity is calculated, not total porosity. In vuggy or fractured carbonate systems, sonic logs cannot account for secondary porosity and, therefore, produce porosity values that are too low (Asquith and Krygowski, 2004). Neutron logs measure the hydrogen concentration within a formation (Asquith and Krygowski, 2004). Neutron porosities are much larger than actual porosity values in formations that have interstitial mud and/or clays. This is due to the hydrogen that is bound to the mud and/or clay's internal structure, which increases the neutron porosity values. This is called the shale effect (Asquith and Krygowski, 2004).

Table 1. Hydraulic conductivities and horizontal permeabilities for specified intervals (modified from Hovorka et al., 1995). The first six columns are from Hovorka et al., 1995. The remaining columns are results from this study.

Well #	Tested Top (m)	Tested Bottom (m)	Specific Capacity (m^2/d)	Trans. (m^2/d)	Interval Hydraulic Conductivity (m/s)	Interval		Avg. ρ_w (kg/m^3)	Avg. Temp °C	Viscosity (Pa/s)	Intrinsic Horizontal Perm. (D)
						From (m)	To (m)				
616	135.3	154.2	7.7	4.3	2.6E-06	135.3	154.2	997.2	26.0	8.7E-04	0.2
	135.3	169.5	28.7	21.3	1.3E-05	154.2	169.5	997.0	26.7	8.6E-04	1.2
	135.3	184.7	29.1	21.6	2.5E-07	169.5	184.7	996.8	27.4	8.4E-04	0.0
	135.3	209.4	36.4	28.4	3.2E-06	184.7	209.4	996.6	27.9	8.3E-04	0.3
	135.3	224.6	48.7	40.5	9.2E-06	209.4	224.6	996.5	28.4	8.2E-04	0.8
	135.3	255.1	92.7	89.1	1.9E-05	224.6	255.1	998.2	29.1	8.1E-04	3.1
	135.3	270.4	128.8	133.1	3.3E-05	255.1	270.4	996.4	29.8	8.0E-04	2.8
617	143.9	161.5	15.2	2.3	1.5E-06	143.9	161.5	996.6	27.6	8.4E-04	0.1
	143.9	171.9	65.5	13.7	1.3E-05	161.5	171.9	996.6	28.2	8.3E-04	1.1
	143.9	188.1	71.3	15.1	1.1E-06	171.9	188.1	996.2	28.3	8.3E-04	0.1
	143.9	221.6	115.2	27.2	4.2E-06	188.1	221.6	996.2	28.9	8.1E-04	0.4
	143.9	253.6	383.4	118.2	3.3E-05	221.6	253.6	996.0	29.9	8.0E-04	2.7
	143.9	268.5	456.6	146.0	2.2E-05	253.6	268.5	996.0	30.0	8.0E-04	1.8
619	157.9	175.9	5.0	2.5	1.6E-06	157.9	175.9	996.9	26.2	8.6E-04	0.2
	157.9	186.8	17.3	11.4	9.4E-06	175.9	186.8	996.9	26.4	8.6E-04	0.8
	157.9	201.5	23.4	16.5	4.0E-06	186.8	201.5	996.8	26.6	8.6E-04	0.4
	157.9	215.2	21.4	14.9	3.0E-06	201.5	215.2	996.7	26.7	8.5E-04	0.3
	157.9	236.5	46.4	38.2	1.3E-05	215.2	236.5	996.7	26.9	8.5E-04	1.1
	157.9	252.1	58.7	50.9	9.6E-06	236.5	252.1	996.7	27.0	8.5E-04	0.8
	157.9	267.3	111.9	112.0	4.7E-05	252.1	267.3	996.7	27.1	8.5E-04	4.1
	157.9	282.9	109.5	109.3	1.0E-05	267.3	282.9	998.6	27.4	8.4E-04	0.9
	157.9	292.3	61.2	53.6	4.6E-06	282.9	292.3	1007.4	27.7	8.4E-04	0.4

Density porosity logs were digitized using the program Engauge Digitizer. The vertical axis was set using depth (m), and the horizontal axis was set using the density porosity scale, which varied from -15 to 40 %. Once each axis was set, points were plotted along the well log curve. Once the entire log had been plotted, the data were imported into Microsoft Excel, where total porosities were arithmetically averaged for each stratigraphic formation for all wells (Appendix A).

BASIN2 PHYSICAL MODEL

Basin2 input files were constructed in Microsoft WordPad for the New Braunfels transect of the Edwards aquifer. Each model was run as steady-state with Basin2 assuming fully compacted sediment, salinity distribution as a function of diffusion, dispersion, and advection, temperature distribution as a function of conduction and advection, and with the left and right side of the cross-section open to flow. The left and right sides do not act as pressure boundaries because this is an extremely local, focused model with flow occurring across these boundaries. At the base of the Kainer formation is a no flow boundary. This is due to lack of well data past the Basal Nodular member and due to the fact that the Glen Rose limestone formation is the lower confining unit of the Edwards aquifer. In addition, the potentiometric surface was input (data from Hamilton et al., 2006) and was the driving force of fluid flow within these models. The residence time option was turned on for the aquifer, as well as the “tables” option, which produced Basin2 output files. Also, the Basin2 option of “under_relax” was turned on, and equal to 0.01, to ensure that each model would run until convergence.

The total cross-sectional length of the 2-D Basin2 model was set at 920 meters, the distance from the LCRA well to well A (Figures 9 and 10). The cross-section was constructed to have the LCRA well on the left (Northwest) with well A on the right (Southeast). Three faults

were created in the input file, exactly halfway between each well. Fault locations are based on actual fault locations, according to Schindel et al. (2005). The "x_well (m)" command was set to input the locations of real wells and "fake" wells along the cross-section in meters. Real wells are located at 0 m , 450 m, 680 m, and 920 m (LCRA, C, B, and A). Primary "fake" wells were also located at 225 m, 565 m, and 800 m, as well as secondary "fake" wells at 224.9 m, 225.1 m, 564.9 m, 565.1 m, 799.9 m, and 800.1 m to simulate structural faults. Secondary "fake" wells are separated by 0.2 m to simulate the thickness of a fault. Basin2 cannot accommodate structural faults (Bethke et al., 2007), so well locations had to be constructed in this particular manner to get actual structural faults represented correctly in the model. Hydraulic faults were input at the same locations of the primary "fake" wells to complete the creation of a normal faulted aquifer system. These locations are at 225 m, 565 m, and 800 m. The hydraulic faults were extended through each stratigraphic formation. This was performed by setting the "fault_bottom" and "fault_top" function. "Fault_bottom" was set to one and "fault_top" was set to thirteen. Horizontal fault permeability, as well as vertical fault permeability, was set to 0.1 D as the base model. In addition, real and primary "fake" wells were named using the "well_name" function (LCRA, Fault 1, C, Fault 2, B, Fault 3, A).

Rock properties were constructed for each stratigraphic formation. Seven stratigraphic subunit properties were created in the input file. The first (top) subunit is geologically oldest and the last (bottom) subunit is geologically youngest (Bethke et al., 2004). For the non-aquifer stratigraphy above the Edwards aquifer, rock properties built into Basin2's code were used due to lack of permeability data. The non-aquifer stratigraphy consists of seven subunits for a total of fourteen subunits used in Basin2. However, one non-aquifer subunit was defined as a hiatus in

deposition between the Cretaceous and Quaternary stratigraphy, so it does not define an actual stratum. Table 2 shows the built-in rock properties defined by Basin2.

Table 2. Rock properties built into Basin2.

	Sandstone (ss)	**Shale (sh)**	**Carbonate (cn)**
Porosity			
phi0	0.4	0.55	0.4
phi1	0.05	0.05	0.05
bpor (km-1)	0.5	0.85	0.55
bpor_ul (km-1)	0.1	0.17	0.11
Permeability			
A_Perm	15	8	6
B_Perm (log D)	-3	-7	-4
p_kxkz	2.5	10	2.5
perm_max (D)	1	1	1
Grain Density	2.65	2.74	2.75
Thermal Conductivity			
A_tc (cal/cm sec °C)	-4.40E-03	-4.40E-03	-4.40E-03
B_tc (cal/cm sec °C)	5.35E-03	5.35E-03	5.35E-03
t_kxkz	1	1	1
Heat Capacity			
A_mk	2.20E-01	4.21E-01	3.44E-01
B_mk	1.23E-04	7.23E-06	8.45E-06
C_mk	2.65E-09	5.19E-09	1.57E-08
D_mk	-7.22E-01	-3.98E+00	-1.97E+00
E_mk	-3.29E-03	-4.02E-04	-3.06E-03
Diffusion and Dispersion			
diff_con	1.00E-06	1.00E-06	1.00E-06
diff_tres	0	0	0
diff_T (K)	0	0	0
difft_tres (K)	0	0	0
alpha_L (cm)	1000	1000	1000
alpha_T (cm)	100	100	100

The oldest aquifer formation, the Kainer formation, was divided into four stratigraphic subunits: the Basal Nodular member, identified as “rock bas;” the Dolomitic member, identified

as “rock dol;” the Kirschberg Evaporite member, identified as “rock ev;” and the Grainstone member, identified as “rock grs.” For the Person formation, two stratigraphic subunits were created for the Regional Dense member, identified as “rock rdm,” and for the Leached, Collapsed, Cyclic, and Marine members that were combined into an Undivided member, identified as “rock per.” The Georgetown formation was also created, identified as “rock gtn.” Parameters that were constructed in the input file are listed in Table 3.

Table 3. Rock parameters created for each rock subunit for Basin2.

Rock Properties						
Rock	**Phi0**	**Phi1**	**A_Perm**	**B_Perm (log D)**	**rho_rk (g/cm^3)**	**p_kxkz**
rock bas	21.3	0	-3.7878	1.2388	2.71	100
rock dol	23.3	0	7.5552	-1.4158	2.877	100
rock ev	21.5	0	-9.4913	2.3819	2.96	100
rock grs	26	0	-2.8744	0.6515	2.71	100
rock rdm	8	0	-2.9299	0.3243	2.71	100
rock per	25	0	-2.9299	0.3242	2.71	100
rock gtn	22	0	-0.6966	-0.6303	2.71	100

The “Phi0” function controls reducible porosity present at deposition, while the “Phi1” function controls irreducible porosity (Bethke et al., 2007). Since a single value of porosity was required for Basin2, porosities were arithmetically averaged for each formation between all wells. Basin2 also required two coefficients for permeability, “A_Perm” and “B_Perm,” which were determined by graphing the arithmetically averaged porosities versus logarithmic permeability of wells A, B, and C. The LCRA well was not used because the packer test performed by Hovorka et al. (1995) did not extend to the LCRA well, so no permeability

calculations could be made. “A_Perm” is the slope of the permeability correlation with porosity, while “B_Perm” is the intercept of the permeability correlation with porosity. Appendix B shows the tables and graphs for all seven stratigraphic subunits created. The “rho_rk” function is rock matrix density of the rock. Values for rock matrix density were attained from Asquith and Krygowski (2004). “p_kxkz” is the permeability anisotropy value and was set to 100 for all subunits. Transmissivity was not an included parameter in any model.

Thirteen stratigraphic subunits were created with the column function (excluding the hiatus subunit), which required a series of well statements. For each well (LCRA, C, B, and A), thickness (m), lithology, formation subunit tops, surface temperature at the top of a formation subunit, and salinity concentrations at the top of formation subunits were defined (Appendix C). Lithology was determined by the “x” function and was determined as a fraction of two rock units. The “x” function refers back to the rock properties that were defined in Table 3 or the built-in properties defined by Basin2 (Table 2). The rock properties that were created specifically for each subunit were used (e.g. bas or dol), as well as the V_{SH} values determined by equation 7. V_{SH} values (Appendix A) were input as a fraction and were defined by Basin2’s built-in shale rock properties (Table 2). “Dep_wat” refers to the stratigraphic tops of each subunit. Positive “dep_wat” values refer to depth of formation tops below sea level, while negative values refer to depth of formation tops above sea level (Appendix A). “Dep_wat” values were determined by subtracting formation tops by the land surface datum for each well (Table 4). In the case of the first subunit, real water depth is represented by “dep_wat.”

Table 4. Land surface datums for all wells.

Land Surface Datum				
Well	**A**	**B**	**C**	**LCRA**
LSD (m)	193.548	193.548	193.548	192.024

The temperatures at the top of each subunit were defined by the function "t_surf." These values were attained by the digital data obtained by digitizing the fluid temperature logs. Fluid temperatures (°C) were correlated with the correct subunit tops for all wells. Also, salinity concentrations at the top of each subunit were defined by the function "c_surfw." Salinities obtained from Figure 15 were converted from mg/L to molality (mol/L) using the molecular weight of NaCl (58.4428 g/mol) (Bethke et al., 2007). Basin2 required salinities to be in molality (Bethke et al., 2007). Inputting the fluid temperatures and salinities allowed Basin2 to calculate the correct distribution of fluid density across the New Braunfels transect. An example of a partial input file is shown in Figure 16.

The time at which deposition of a formation was completed was defined by the function "t_dep." Basin2 considers time as negative and assumes a uniform rate of deposition (Bethke et al., 2007). Values were defined in the input file as negative with units of "m.y." for million years. Values were obtained from Young (1986). However, since all models were run as steady-state, Basin2 considered the stratigraphy to be invariant with time (Bethke et al., 2007) but required them in order to construct the stratigraphy properly.

HYPOTHESES TESTED USING BASIN2

A base model was produced to serve as reference for all other models. To test the hypothesis in which extremely high fluid density acts as the mechanism inhibiting fluid flow across the freshwater/saline-water interface, two models were produced that set the Kirschberg Evaporite member salinity equal to halite saturation. Halite saturation model 1 has horizontal fault permeability of 0.1 D and a vertical fault permeability of 0.1 D. Halite saturation model 2 has horizontal fault permeability of 0.01 D and a vertical fault permeability of 0.1 D. To test the hypothesis in which faults are acting as fluid flow barriers, models were produced that reduced

the horizontal fault permeability by an order of magnitude for each model from the Base Model (0.1 D). These models include Model 1, 5, and 9 (i.e. 0.01, 0.001, and 0.0001 D, respectively). In addition, to test the hypothesis in which saline water zone permeability is limiting movement across the interface, aquifer rock permeability was reduced by an order of magnitude for each model from the Base Model. Models 2-4 have the same fault permeability as Model 1 (aquifer rock permeability was reduced one, two, and three orders of magnitude, respectively). Models 6-8 have the same fault permeability as Model 5 (aquifer rock permeability was reduced one, two, and three orders of magnitude, respectively). Model 10-12 have the same fault permeability as Model 9 (aquifer rock permeability was reduced one, two, and three orders of magnitude, respectively). Vertical fault permeability was not altered from 0.1 D.

```
rock bas
        phi0 = 21.3%; phi1 = 0; A_perm = -3.7878;
        B_perm = 1.2388 log_darcy; rho_rk = 2.71 g/cm3;
        p_kxkz = 100
rock dol
        phi0 = 23.3%; phi1 = 0; A_perm = 7.5552;
        B_perm = -1.4158 log_darcy; rho_rk = 2.877 g/cm3;
        p_kxkz = 100
rock ev
        phi0 = 21.5%; phi1 = 0; A_perm = -9.4913;
        B_perm = 2.3819 log_darcy; rho_rk = 2.96 g/cm3;
        p_kxkz = 100;
rock grs
        phi0 = 26%; phi1 = 0; A_perm = -2.8744;
        B_perm = 0.6515 log_darcy; rho_rk = 2.71 g/cm3;
        p_kxkz = 100
rock rdm
        phi0 = 8%; phi1 = 0; A_perm = -2.9299;
        B_perm = 0.3243 log_darcy; rho_rk = 2.71 g/cm3;
        p_kxkz = 100
rock per
        phi0 = 25%; phi1 = 0; A_perm = -2.9299;
        B_perm = 0.3243 log_darcy; rho_rk = 2.71 g/cm3;
        p_kxkz = 100
rock gtn
        phi0 = 22%; phi1 = 0; A_perm = -0.6966;
        B_perm = -0.6303 log_darcy; rho_rk = 2.71 g/cm3;
        p_kxkz = 100


left = open; right = open;
strat 'Kainer, Basal Nodular'
        t_dep = -105.5 m.y.
        column  thickness(m) x(bas) x(sh) dep_wat(m) t_surf c_surfw
        w (1:2)         4.57    .58  .42   131.67     27.68  .4277
        w (3:7)         4.57    .58  .42   85.34      27.68  .4277
        w (8:10)        4.27    .65  .35   72.85      30.50  .0119
        w (11:13)       11.89   .76  .24   71.93      29.81  .0155
strat 'Kainer, Dolomitic'
        t_dep = -104.34 m.y.
        column  thickness(m) x(dol) x(sh) dep_wat(m) t_surf c_surfw
        w (1:2)         39.62   .73  .27   127.10     27.43  .0856
        w (3:7)         39.62   .73  .27   80.77      27.43  .0856
        w (8:10)        38.40   .71  .29   68.58      29.85  .0052
        w (11:13)       36.27   .74  .26   60.05      29.42  .0154
strat 'Kainer, Kirshberg Evaporite'
        t_dep = -103.17 m.y.
        column  thickness(m) x(ev) x(sh) dep_wat(m)  t_surf c_surfw
        w (1:2)         11.28   .73  .27   87.48      26.93  .0023
        w (3:7)         11.28   .58  .42   41.15      26.93  .0023
        w (8:10)        9.14    .56  .44   30.18      29.00  .0025
        w (11:13)       12.19   .64  .36   23.77      28.28  .0095
strat 'Kainer, Grainstone'
        t_dep = -102 m.y.
        column  thickness(m) x(grs) x(sh) dep_wat(m) t_surf c_surfw
        w (1:2)         17.37   .82  .18   76.20      26.90  .0022
        w (3:7)         16.76   .75  .25   29.87      26.90  .0022
        w (8:10)        21.34   .70  .30   21.03      28.85  .0018
        w (11:13)       20.12   .73  .27   11.58      28.04  .0073
```

Figure 16. An example of a partial input file showing the “x”, “dep_wat”, “t_surf”, and “c_surfw” functions.

RESULTS

BASE MODEL

The base model produced the highest flow rates of all models across the Edwards Aquifer (Figures 17 and 18). Figure 17 shows the saline water wedge. It is drawn at 500 ppm. The wedge will not be indicated on further models because it will cover flow velocity arrows. Figure 18 does not show a wedge because the upper portion of the cross-section is colder and is represented in fluid density not salinity. The three fault zones, with a horizontal and vertical fault permeability of 0.1 D and no reduced aquifer rock permeability, do not act as flow barriers within this karst aquifer. Minimal flow velocity changes occur along the flow path, indicating that a horizontal fault permeability of 0.1 D is too large to inhibit flow. The base model was produced to get an estimation of aquifer geometries and flow velocities. Because flow velocities are extremely high across the freshwater/saline-water boundary, this model does not accurately portray current flow patterns.

However, this model did provide an initial indication of flow rates and how to reduce these rates, to get more accurate results. Table 5 shows the horizontal and vertical flow velocity ranges, as well as fluid density ranges for the base model. Initial contouring of salinity and temperature (Figures 19 and 20, respectively) proved the base model salinity to be accurate. No fluid resistivity or fluid temperature logs existed for the LCRA well. That is why data does not extend passed Well C.

The base model does, though, accurately display the distribution of fluid densities along the transect. The low fluid density area in the center of the transect (value range of 1010-1007.5 kg/m^3), indicated by white on the color map, does overlie the saline-water wedge, which intrudes

into the freshwater zone. The position of the low fluid density area, which indicates the freshwater/saline-water interface, is very accurate. Overlying the interface is water that has slightly higher fluid densities (value range of 1007.5-1.015 kg/m^3) due to colder temperatures. Underlying the interface is water that also has higher fluid densities (value range of 1015-1021 kg/m^3). It is important to note that values of fluid density do not actually get to the 1022-1028 kg/m^3 range of seawater. Therefore, the entire transect is considered brackish waters.

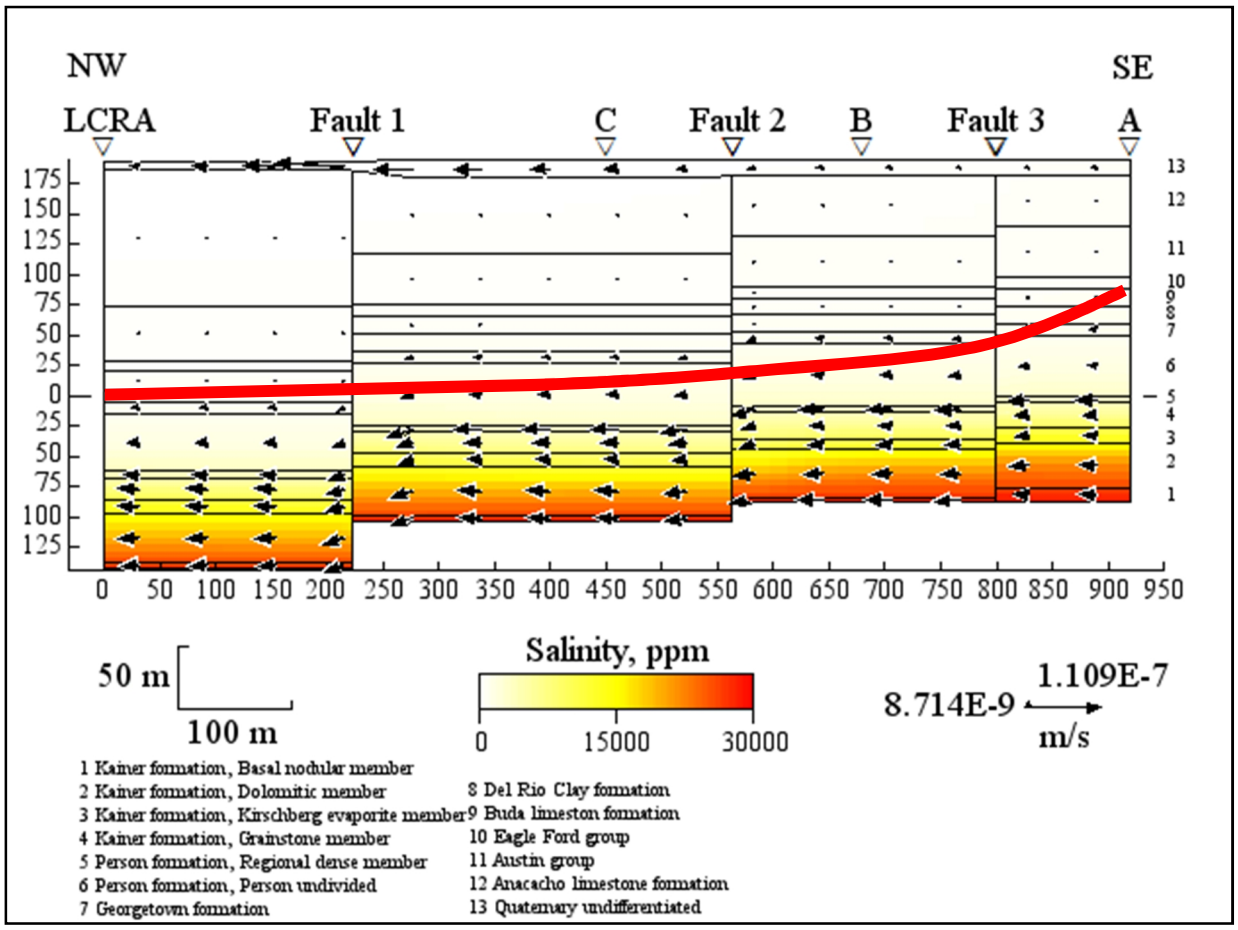

Figure 17. The Base Model (salinity, in ppm) is shown with the saline water wedge highlighted.

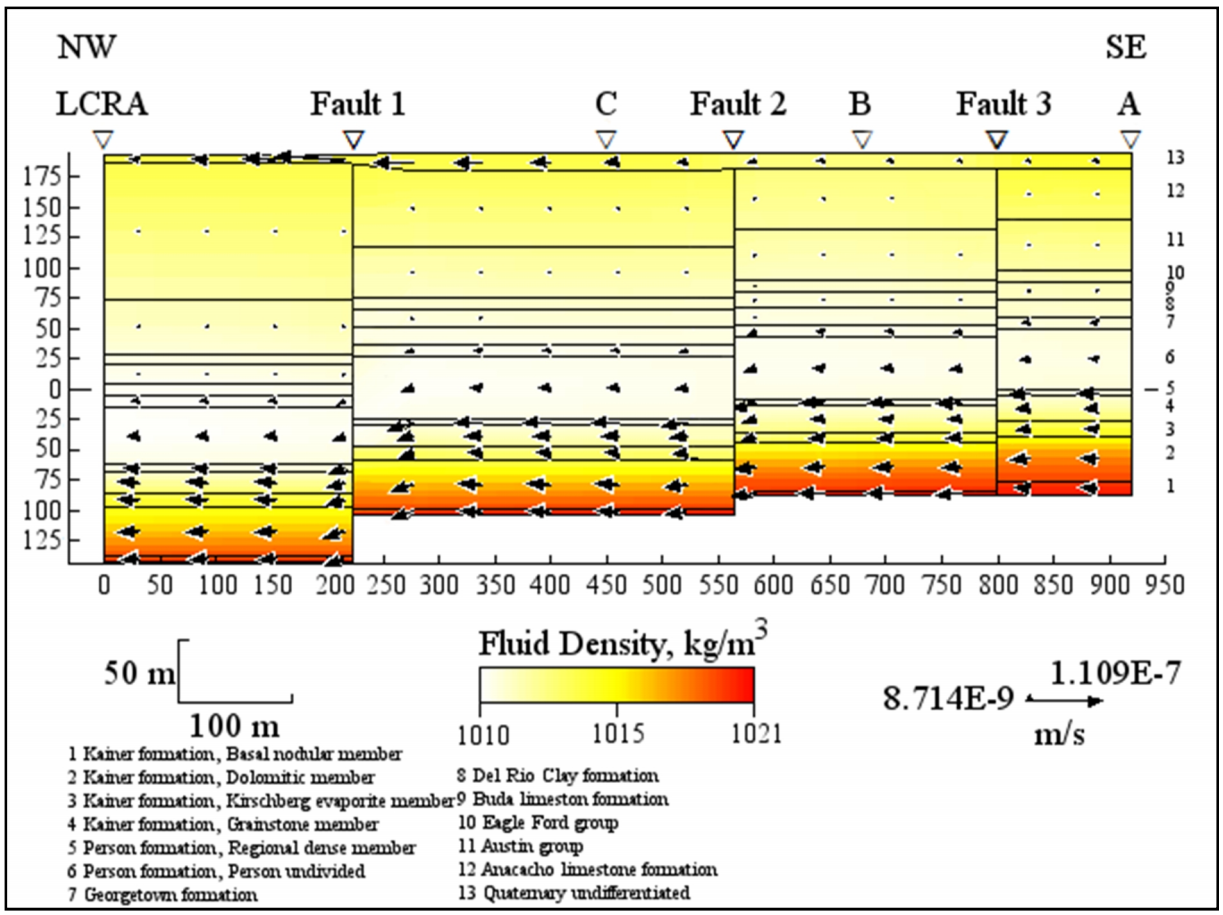

Figure 18. The Base Model for the New Braunfels transect of the Edwards Aquifer.

Table 5. Horizontal and vertical flow velocity and fluid density ranges for each rock subunit for the Base Model.

Subunit	Horizontal Flow Velocity Range (m/s)		Vertical Flow Velocity Range (m/s)		Fluid Density Range (kg/m^3)	
	From	To	From	To	From	To
Quaternary	1.0E-07	5.3E-09	1.9E-09	5.1E-09	1012	1014
Anacacho	2.2E-09	9.3E-10	1.6E-09	2.0E-11	1012	1013
Austin Chalk	1.5E-09	1.3E-09	1.9E-09	3.7E-12	1011	1012
Eagleford	1.6E-10	9.5E-11	1.5E-09	3.7E-13	1010	1011
Buda	1.5E-09	1.0E-09	1.9E-09	1.8E-12	1010	1011
Del Rio	1.8E-10	8.0E-11	1.5E-09	9.7E-12	1010	1011
Georgetown	1.1E-08	9.4E-09	5.1E-09	3.2E-11	1010	1011
Person Undivided	1.7E-08	1.4E-08	5.9E-09	2.8E-11	1010	1010
Regional Dense Member	4.1E-08	2.1E-08	1.2E-08	2.1E-11	1010	1010

Table 5 continued.

Grainstone	3.5E-08	1.9E-08	7.7E-09	7.3E-12	1011	1012
Kirschberg Evaporite	3.1E-08	1.9E-08	6.5E-09	1.4E-11	1012	1014
Dolomitic	3.3E-08	2.5E-08	9.9E-09	2.6E-11	1017	1018
Basal Nodular	3.8E-08	2.1E-08	9.8E-09	2.6E-10	1021	1021

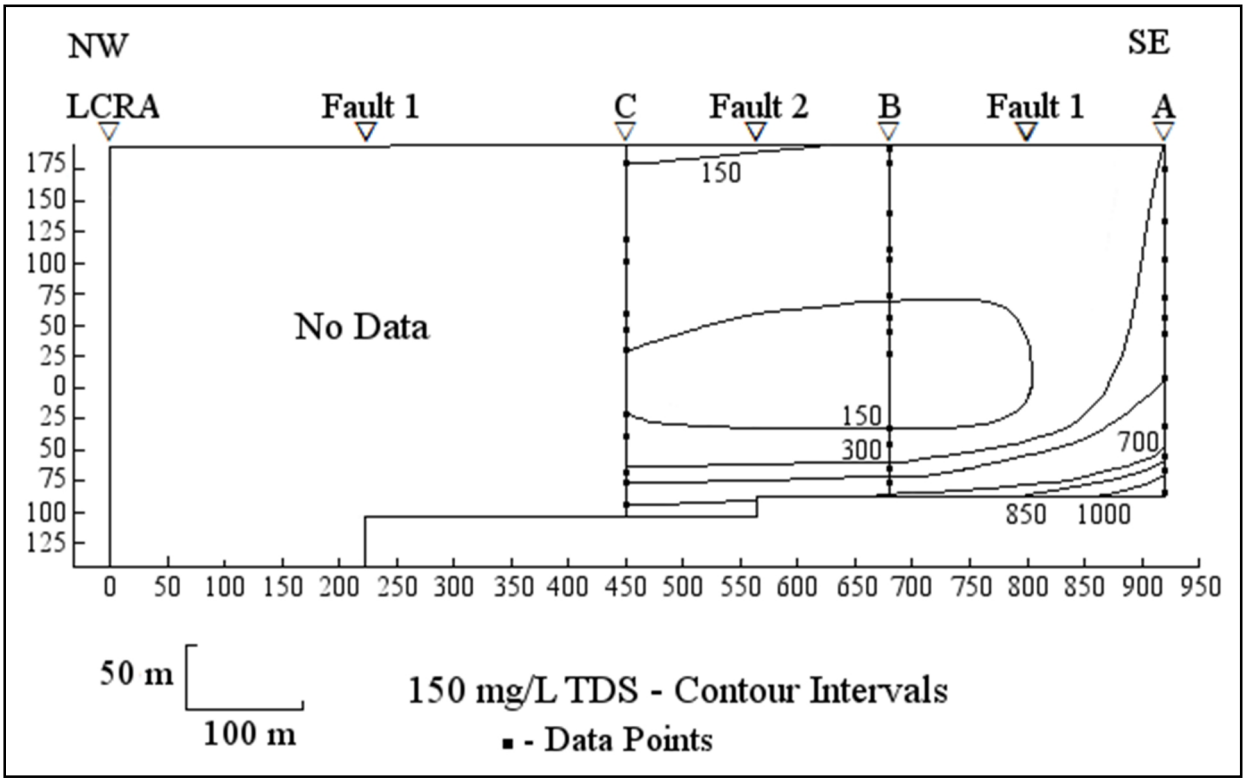

Figure 19. Contours of salinity (mg/L) based on fluid resistivity and fluid temperature well log calculations.

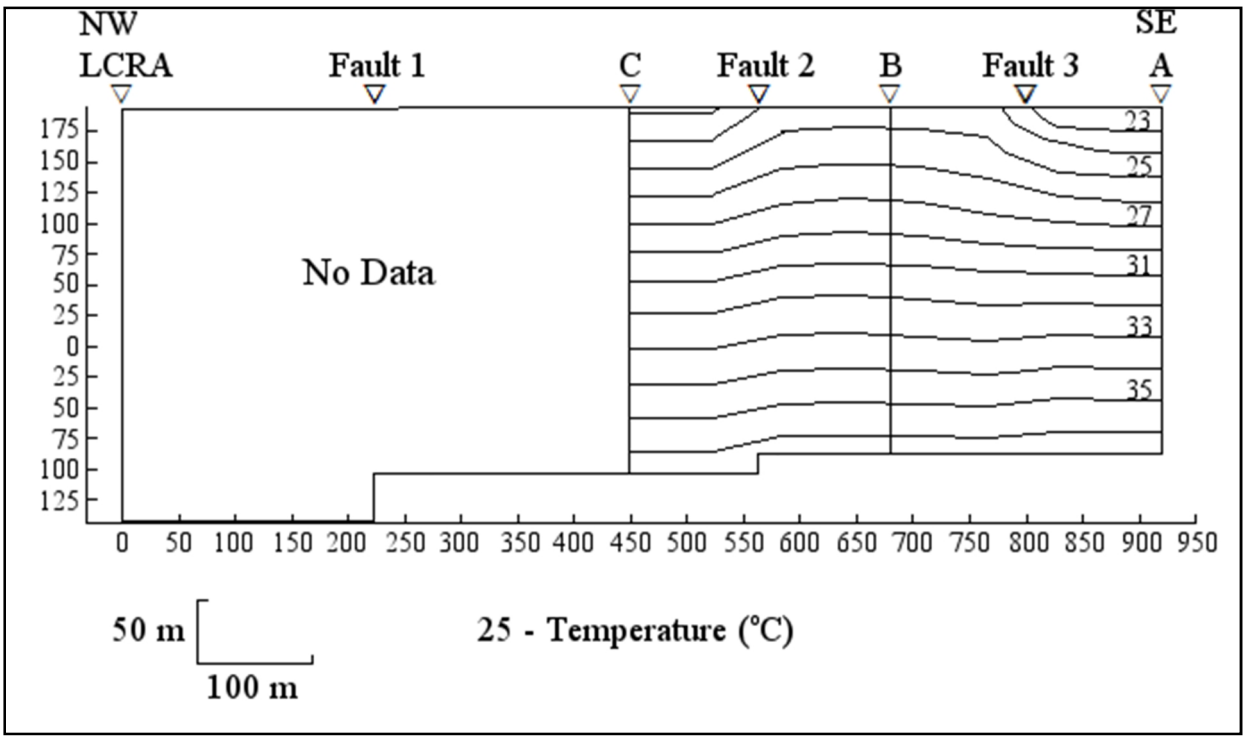

Figure 20. Contours of temperature (°C) based on fluid temperature well logs.

HALITE SATURATION MODELS

The models produced to test the effects of increased fluid density on flow (Figures 21 and 23) indicate that increased fluid density, with salinity equal to halite saturation (6.5 molality or 380,000 ppm), is not a controlling factor inhibiting saline-water intrusion, because significant flow is still occurring across the freshwater/saline-water interface in both models. 380,000 ppm equivalent-NaCl salinity for the halite-saturated models are the maximum salinity that can be geochemically achieved (Langmuir, 1997), and therefore, provided an excellent benchmark to test whether fluid density played a significant role in the inhibition of flow across the freshwater/saline-water boundary. Fluid densities, in this case controlled primarily by salinity, have pushed the freshwater/saline-water interface approximately 100 meters upward from the base model. The Kirschberg Evaporite member has a fluid density range of 1137.5-1180 kg/m^3.

The other rock subunits within the Edwards aquifer have a fluid density range of 1052.5-1137.5 kg/m^3. The non-aquifer subunits overlying the Edwards Aquifer approach freshwater values.

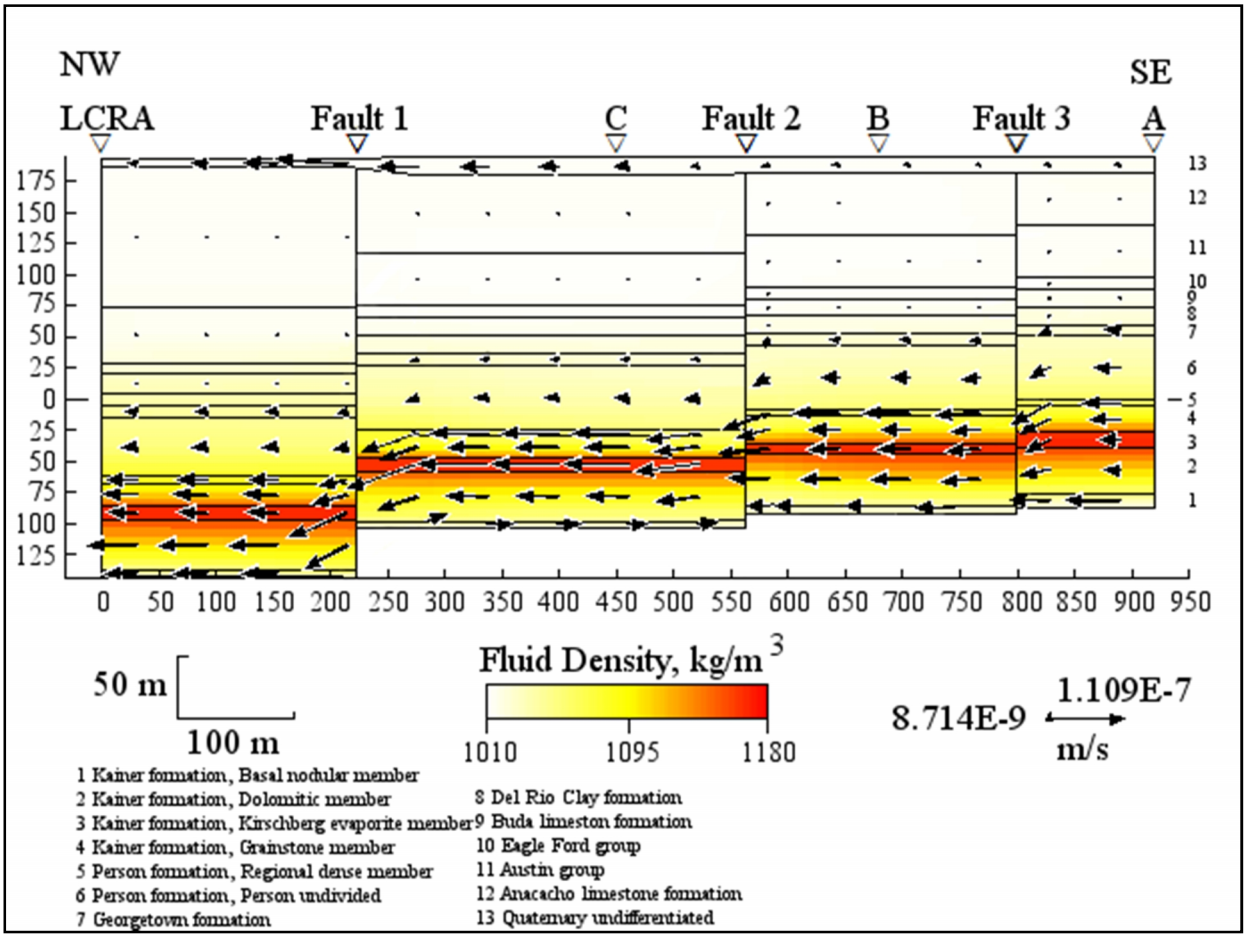

Figure 21. Halite saturation of the Kirschberg Evaporite member with horizontal fault permeability of 0.1 D.

Figure 22 shows horizontal flow velocity ranges for the base model and the two halite saturation models. The first halite saturation model (Figures 21 and 22) shows horizontal flow velocities (purple) reduced by less than one order of magnitude ($2.5x10^{-7}$ m/s) from the base model (gold) ($9x10^{-6}$ m/s). The red line indicates the average horizontal flow velocity values across the aquifer rock subunits for the base model. In addition, the light blue and purple lines indicate the average horizontal flow velocities for the halite saturation models. Figure 22 also indicates that flow velocities for the halite saturation models have broader ranges from the base

model. For the first halite saturation model, this shows that increased fluid density only minimally reduces flow and not enough to prevent flow. Average vertical flow velocities are also reduced by less than one order of magnitude ($9.5x10^{-7}$ m/s) from the base model ($7x10^{-7}$ m/s) and also show the same trend of broader velocity ranges (Appendix D; Figure AD1).

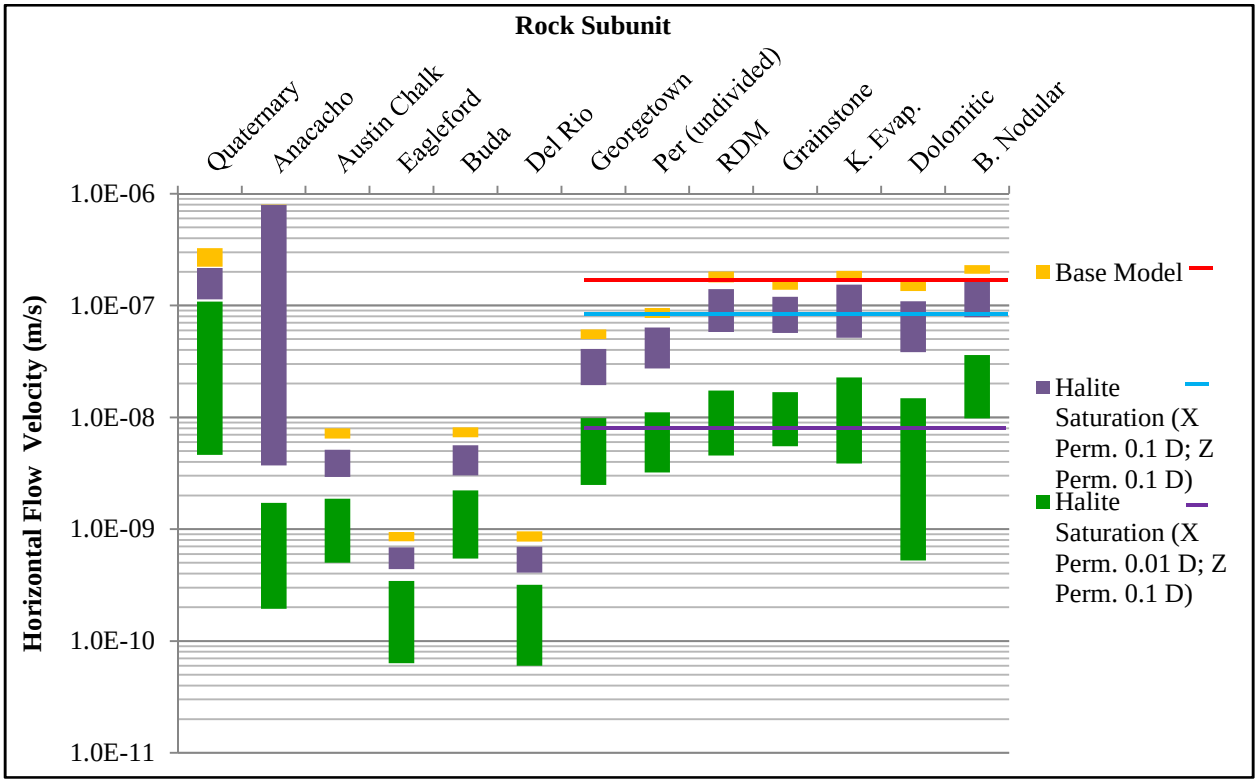

Figure 22. Horizontal flow velocity ranges for the base model and the halite saturation models. Red, light blue, and purple lines represent average horizontal flow velocity (m/s).

In addition to the first halite-saturation model, in which horizontal and vertical fault permeability and aquifer rock permeability were not altered from base model values, a second halite saturation model (Figure 23) was produced to show the effects of reduced horizontal fault permeability on halite saturated flow within the Kirschberg Evaporite. With horizontal fault permeability reduced to 0.01 D, significant flow still occurs. However, the second halite saturation model (Figure 22) does show average horizontal flow velocities (green) reduced by more than one order of magnitude ($2.5x10^{-8}$ m/s) from the base model (gold) ($9x10^{-6}$ m/s) and

one order of magnitude from the first halite-saturation model ($2.5x10^{-7}$ m/s). The reduction of horizontal flow velocity is exclusively due to reduced horizontal fault permeability, not increased fluid density. Therefore, reduction of horizontal fault permeability has a greater effect on flow velocity than increasing salinity to halite saturation. Also, average vertical flow velocities have also decreased by more than two orders of magnitude ($1.5x10^{-9}$ m/s) from the base model ($7x10^{-7}$ m/s). Vertical flow velocity ranges are shown in Table AD1. In addition, between faults 2 and 3, a downward bulge in fluid density has initiated, indicating that high fluid density waters have increased resistance crossing fault zones.

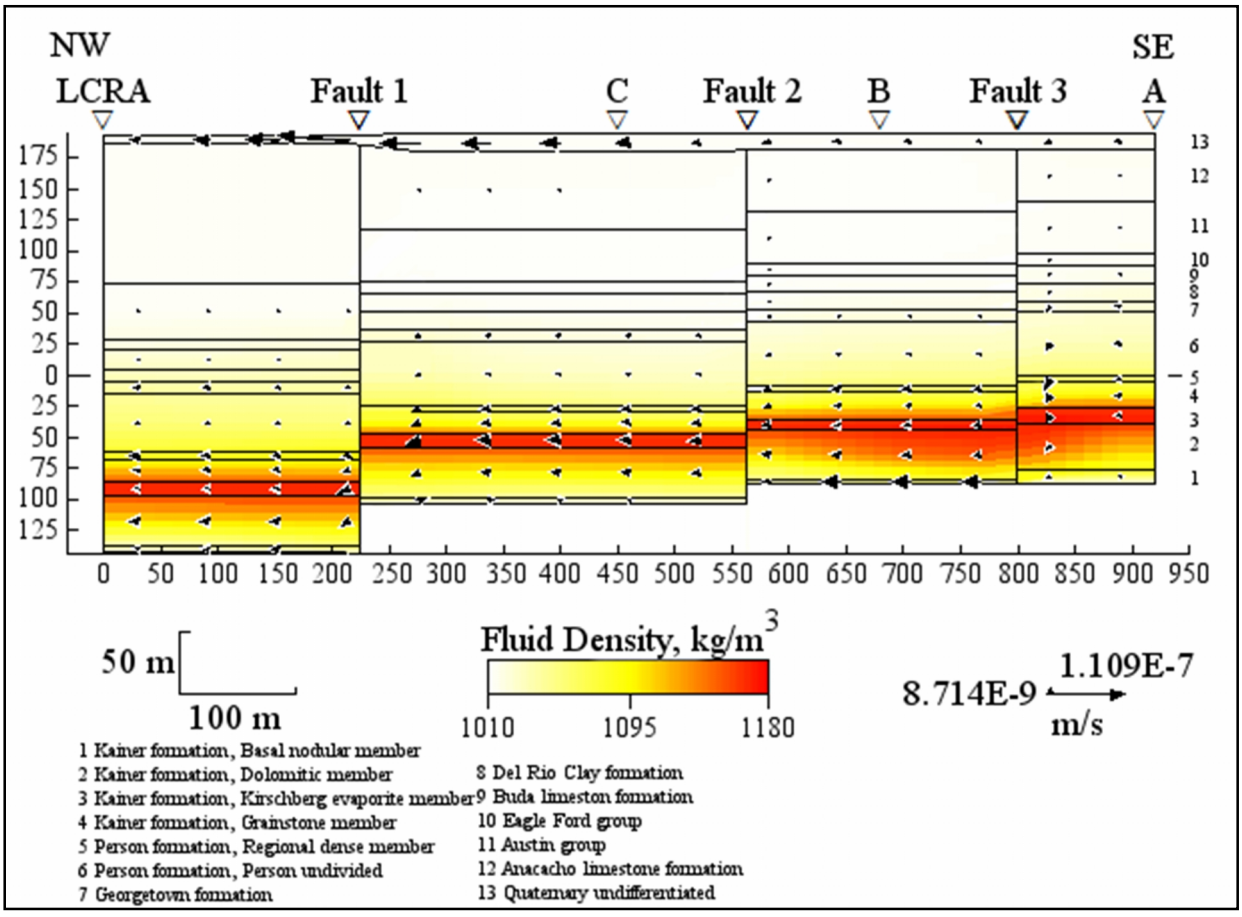

Figure 23. Halite saturation of the Kirschberg Evaporite member with horizontal fault permeability of 0.01 D.

MODELS 1-12

Models 1-12 tested different combinations of horizontal fault and aquifer rock permeability. Models 1-4, 5-8, and 9-12 tested the effects of changing aquifer rock permeability with altered horizontal fault permeability (0.01, 0.001, and 0.0001 D, respectively) and constant vertical fault permeability (0.1 D). Table 6 shows the permeability values used for Models 1-12. These values were attained from "B_Perm" values.

Table 6. Permeability values for Models 1-12.

Aquifer Rock Permeability (D)				
	Models 1, 5, 9	**Models 2, 6, 10**	**Models 3, 7, 11**	**Models 4, 8, 12**
Subunit				
Georgetown	0.23426	0.02343	0.00234	0.00023
Person (Undivided)	2.11009	0.21101	0.0211	0.00211
Regional Dense Member	2.11009	0.21101	0.0211	0.00211
Grainstone	4.48229	0.44823	0.04482	0.00448
Kirschberg Evaporite	240.935	24.0935	2.40935	0.24094
Dolomitic	0.03839	0.00384	0.00038	0.000038
Basal Nodular	17.3301	1.73301	0.1733	0.01733

MODELS 1-4

Figure 24 shows horizontal flow velocity ranges for Models 1-4. These models have horizontal fault permeability values of 0.01 D and vertical fault permeability values of 0.1 D. The red, light blue, purple, and black lines in Figure 24 represent the average horizontal flow velocity for Models 1-4, respectively. Model 1 (Figure 25), which had no reduced aquifer rock permeability, shows significant reduction of average horizontal flow velocity (9.7×10^{-7} m/s) from the base model (Figures 18 and 22) (9×10^{-6} m/s). Average horizontal flow velocities do not include the Quaternary subunit because the fault does not penetrate the Quaternary subunit, and

only aquifer rock subunit permeabilities were altered. The Quaternary subunit, therefore, serves as a benchmark for comparison since velocity ranges for all models remain the same.

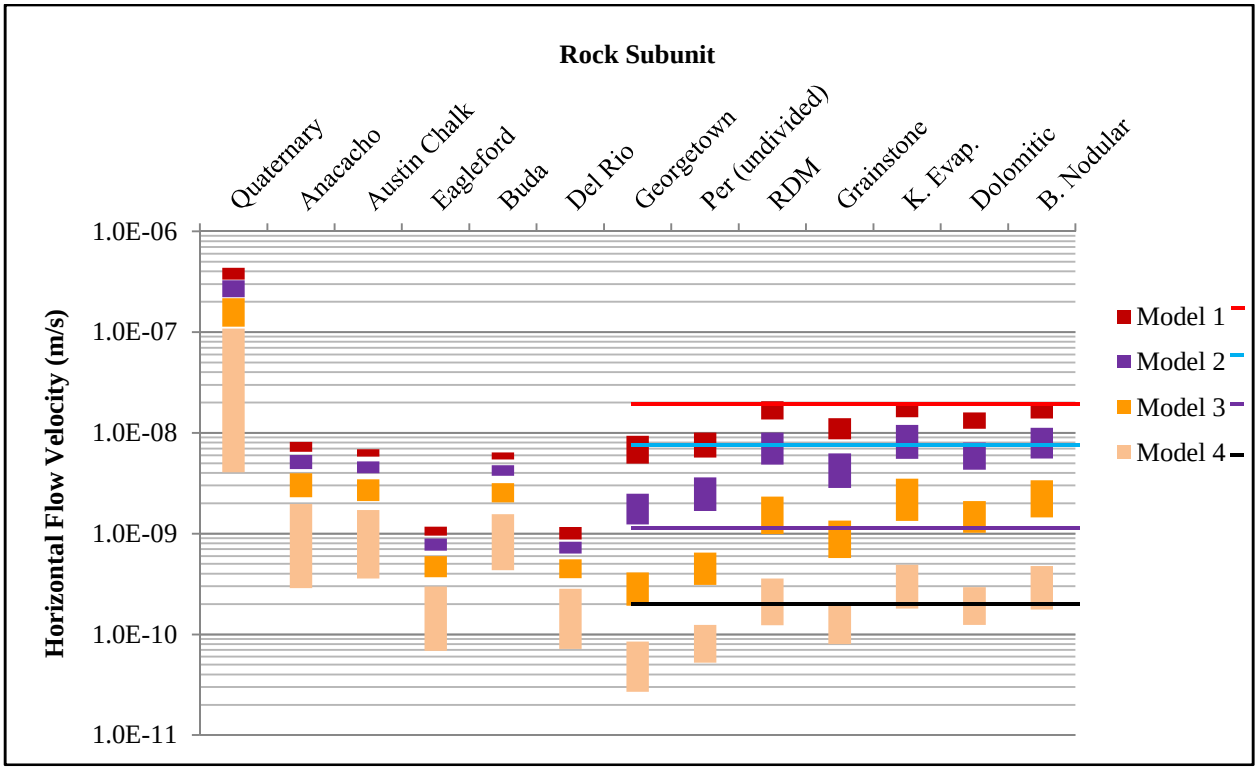

Figure 24. Horizontal flow velocity ranges for Models 1-4. Red, light blue, purple, and black lines represent average horizontal flow velocity (m/s).

In addition, model 1 has the narrowest range of horizontal flow velocities. The highest velocities in Model 1 occur in the Regional Dense member and the lowest occur in the Georgetown subunit. There is also a decreased area of reduced fluid density, representing the freshwater/saline-water interface. The fluid density range in this area, colored white in Figure 25, has a range of 1008-1010 kg/m^3 and extends through the Kirschberg Evaporite member, Grainstone member, Regional Dense member, and Person (undivided) member. Appendix D contains tables with horizontal and vertical flow velocity and fluid density ranges for Models 1-12.

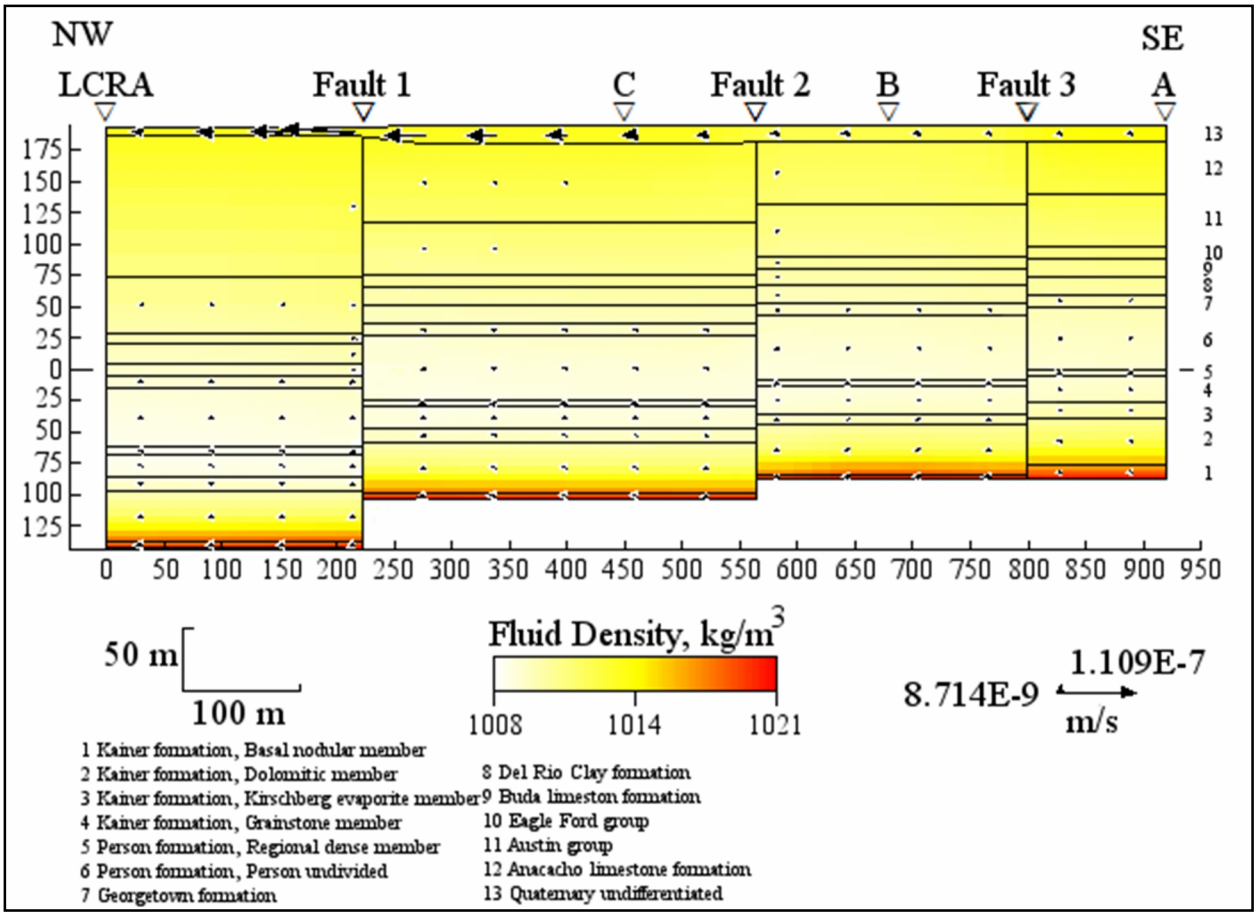

Figure 25. Model 1 is shown. Horizontal fault permeability is 0.01D and vertical fault permeability is 0.1 D, with no reduced aquifer rock permeability.

Model 2 (Figure 26), which has reduced aquifer rock permeability of one order of magnitude (values in Table 6), shows even more reduction in horizontal flow velocity. Average horizontal flow velocity decreased from 9.7×10^{-7} m/s in Model 1 (red) to 5.5×10^{-8} m/s in Model 2 (light blue). The horizontal flow velocity ranges for Model 2 also increase from Model 1. The highest velocities reside in the Kirschberg Evaporite member and the lowest in the Georgetown formation. In addition, flow arrows are reduced from Model 1 and remain in all aquifer subunits, still flowing through all faults. However, flow velocity arrows are absent from the Del Rio and Eagleford shales. At this particular point, velocities are lower than the graphic capabilities of Basin2. This occurs at approximately 8.7×10^{-9} m/s. Model 2 also shows reduced fluid density in the middle subunits (Kirschberg Evaporite, Grainstone, Regional Dense member, Person

(undivided), and Georgetown), which has expanded upward and laterally to the right from Model 1. This reduced fluid density area in the middle has a fluid density range of 1008-1010 kg/m^3.

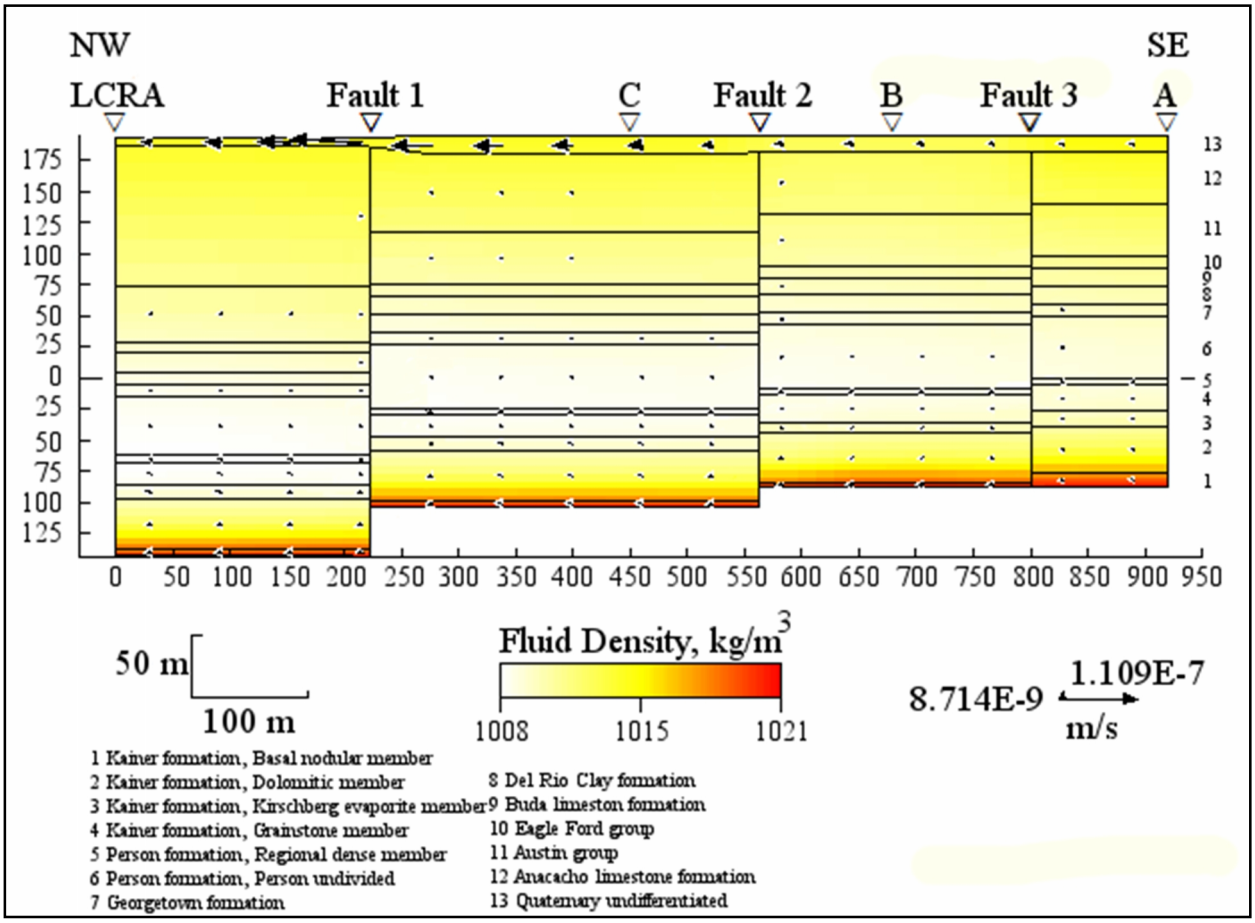

Figure 26. Model 2 is shown. Horizontal fault permeability is 0.01D and vertical fault permeability is 0.1 D, with reduced aquifer rock permeability of one order of magnitude.

Model 3 (Figure 27) has reduced aquifer rock permeability of two orders of magnitude (values in Table 6). Average horizontal flow velocity has been reduced to 1.5x10^{-9} m/s (purple), with the flow velocity within the Kirschberg Evaporite subunit being the highest and the flow velocity within the Georgetown subunit being the lowest. The Grainstone, Person (undivided), and Georgetown subunits have reduced flow enough to inhibit flow velocity arrows within the model. Flow velocity arrows for the Basal Nodular and Kirschberg Evaporite subunits extend throughout the cross-section, flowing through all faults, but the flow velocity arrows for the

Dolomitic and Regional Dense member subunits are concentrated between fault 1 and 2. Again, reduced fluid densities have expanded upward and laterally to the right. The reduced fluid density subunits for Model 3 include: Grainstone, Regional Dense Member, Person (undivided), Georgetown, Del Rio, Buda, Eagleford, and Austin Chalk. This reduced fluid density area in the middle has a fluid density range of 1008-1010 kg/m^3.

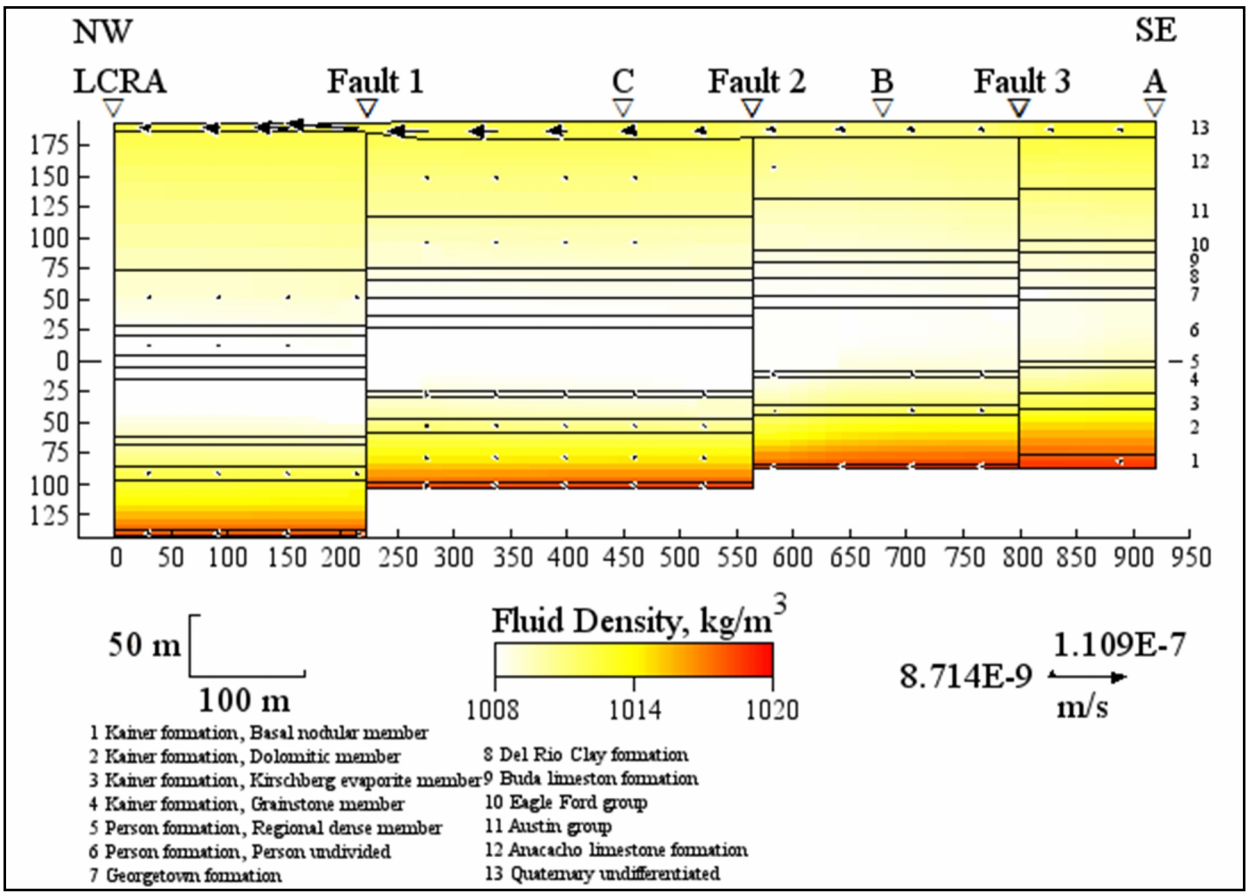

Figure 27. Model 3 is shown. Horizontal fault permeability is 0.01D and vertical fault permeability is 0.1 D, with reduced aquifer rock permeability of two orders of magnitude.

Model 4 (Figure 28) has reduced aquifer rock permeability of three orders of magnitude (values in Table 6). Average horizontal flow velocity has decreased to 9.2x10^{-9} m/s (black). Since flow velocity has dropped below Basin2's ability to resolve the flow velocity arrows, 8.71x10^{-9} m/s, Model 4 does not show any flow velocity arrows in the aquifer subunits. In

addition, since flow has been reduced so much by the reduction of permeability within the saline water zone, the middle reduced fluid density area, which represents the freshwater/saline-water interface, has narrowed and migrated upward out of the Edwards aquifer stratigraphy. However, the freshwater/saline-water interface does not occur outside the Edwards aquifer stratigraphy. Therefore, model 4 does not give an accurate estimation of the Edwards aquifer.

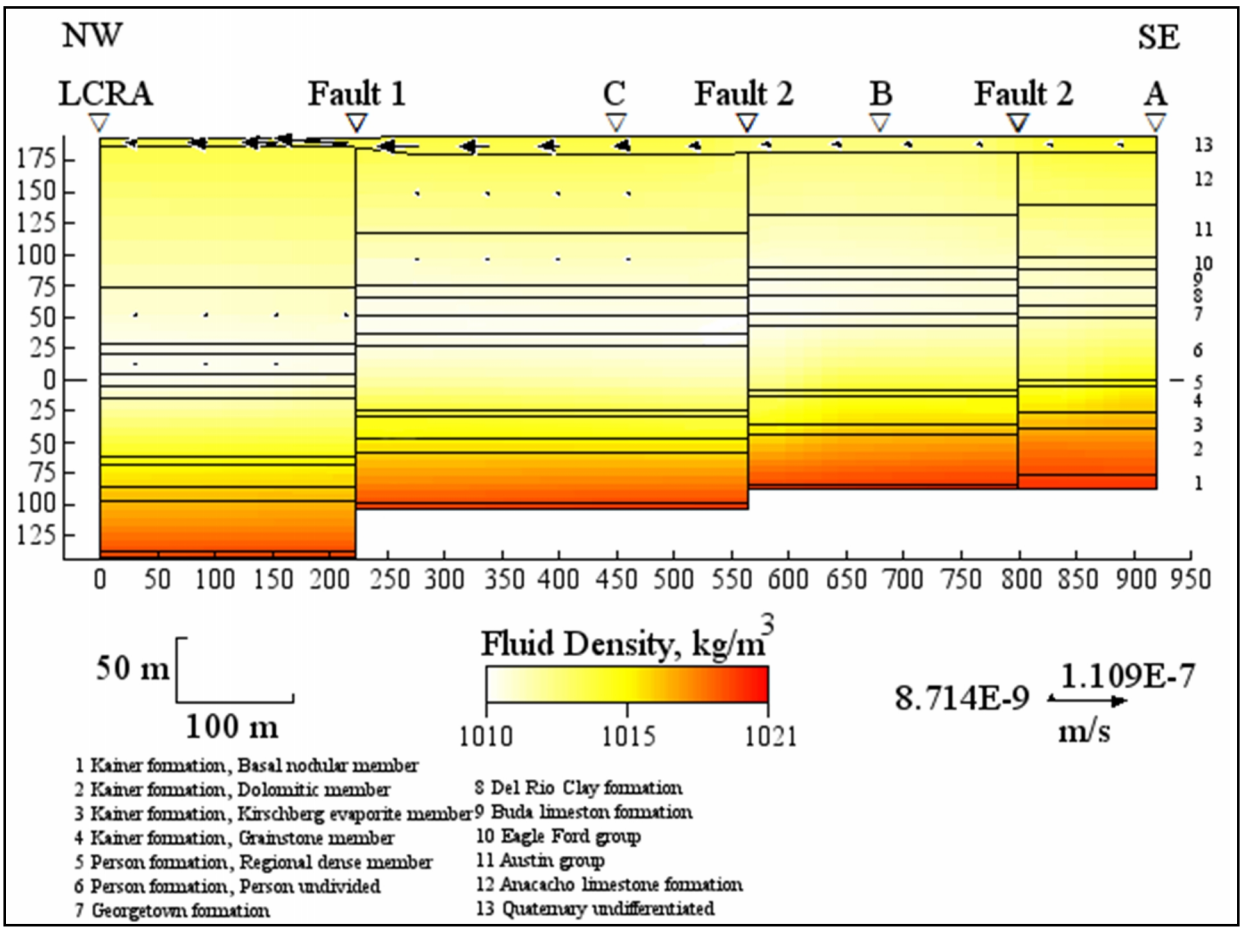

Figure 28. Model 4 is shown. Horizontal fault permeability is 0.01D and vertical fault permeability is 0.1 D, with reduced aquifer rock permeability of three orders of magnitude.

For Models 1-4, vertical flow velocities are shown in Appendix D: Figure AD2. For Models 1-4, the average vertical flow velocities are 8.3×10^{-8} (red), 1.0×10^{-9} (light blue), 9.0×10^{-9} (purple), and 8.0×10^{-11} (black) m/s, respectively. For all rock subunits, excluding the Quaternary subunit, overlap of velocity ranges occurred. The narrowest velocity range occurred in Model 1,

and the largest velocity range occurred in Model 4. For Model 4, the Regional Dense member, Grainstone, Kirschberg Evaporite and Dolomitic subunits had significantly low velocity value ranges that approached $1.0x10^{-13}$ m/s or surpassed it. The Anacacho, Austin Chalk, Eagleford, Buda, and Del Rio Formations have approximately the same vertical velocity ranges, $5.0x10^{-8}$ to $1.0x10^{-11}$ m/s.

MODELS 5-8

Models 5-8 tested changing aquifer rock permeability with constant horizontal fault permeability (0.001 D) and vertical fault permeability (0.1 D). With Model 5 (no reduced aquifer rock permeability) (Figure 29), flow velocity arrows are only present within the Basal Nodular and Georgetown members (excluding the Quaternary subunit) and are only present to the left of fault 1. The dark blue, light blue, dark red, and purple lines represent average horizontal velocity. Average horizontal flow velocity is $8.7x10^{-8}$ m/s (dark blue) (Figure 30). However, the Basal Nodular member, which has the highest flow velocity, has a range of $9.9x10^{-7}$ to $1.0x10^{-8}$ m/s. The lowest velocity resided in the Person (undivided) subunit, with a velocity range of $9.0x10^{-8}$ to $9.8x10^{-8}$ m/s. The middle reduced fluid density area is laterally expansive (LCRA well to Fault 2), ranging from the Kirschberg Evaporite member (85 m below sea level) up to the Del Rio Formation (sea level). Fluid has essentially ceased flowing across the freshwater/saline-water interface. All remaining models will have similar non-flow patterns.

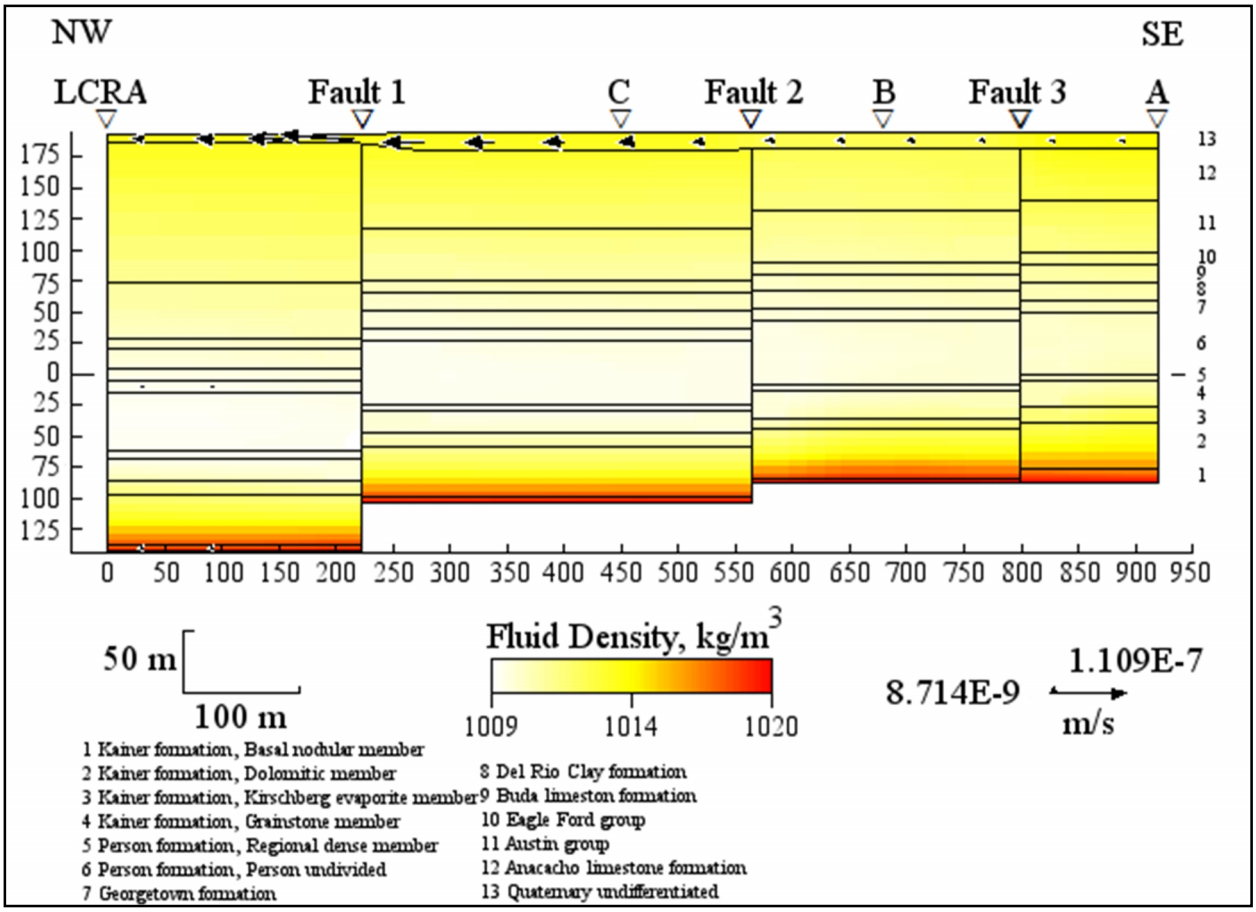

Figure 29. Model 5 is shown. Horizontal fault permeability is 0.001D and vertical fault permeability is 0.1 D, with no reduced aquifer rock permeability.

Model 6 (Figure 31), with reduced aquifer rock permeability of one order of magnitude, has an average horizontal flow velocity of 9.9×10^{-8} m/s (light blue). Flow velocity arrows are only present within the Basal Nodular and Kirschberg Evaporite members (excluding the Quaternary subunit). The highest velocity range occurred in the Basal Nodular member (velocity range of 1.0×10^{-8} to 3.0×10^{-8} m/s), and the lowest occurred in the Georgetown member (velocity range of 1.0×10^{-9} to 6.0×10^{-9} m/s). The middle reduced fluid density area has expanded upward and laterally to the right (LCRA well to Fault 3). Models 7 and 8 (Figures 32 and 33, respectively), do not have any flow velocity arrows since the velocities fall below the level of resolution for Basin2 (excluding the Quaternary subunit). Average horizontal flow velocities are 6.0×10^{-9} (dark red) and 1.5×10^{-10} m/s (purple), respectively. Models 7 and 8 had reduced aquifer

rock permeability of two and three orders of magnitude, respectively. The middle reduced fluid density area within Model 7 has decreased in size and lateral extent across the transect. For Model 8, the middle reduced fluid density area has moved upward and has a similar location of reduced fluid density as Model 4. The average vertical velocities for Models 5-8 (Appendix D: Figure AD3) are 2.0×10^{-9} (dark blue), 6.0×10^{-9} (light blue), 9.5×10^{-9} (dark red), and 6.5×10^{-11} (purple) m/s, respectively. The Grainstone member for Model 8 has the lowest velocity value with 8.2×10^{-15} m/s. This value is the lowest of all models.

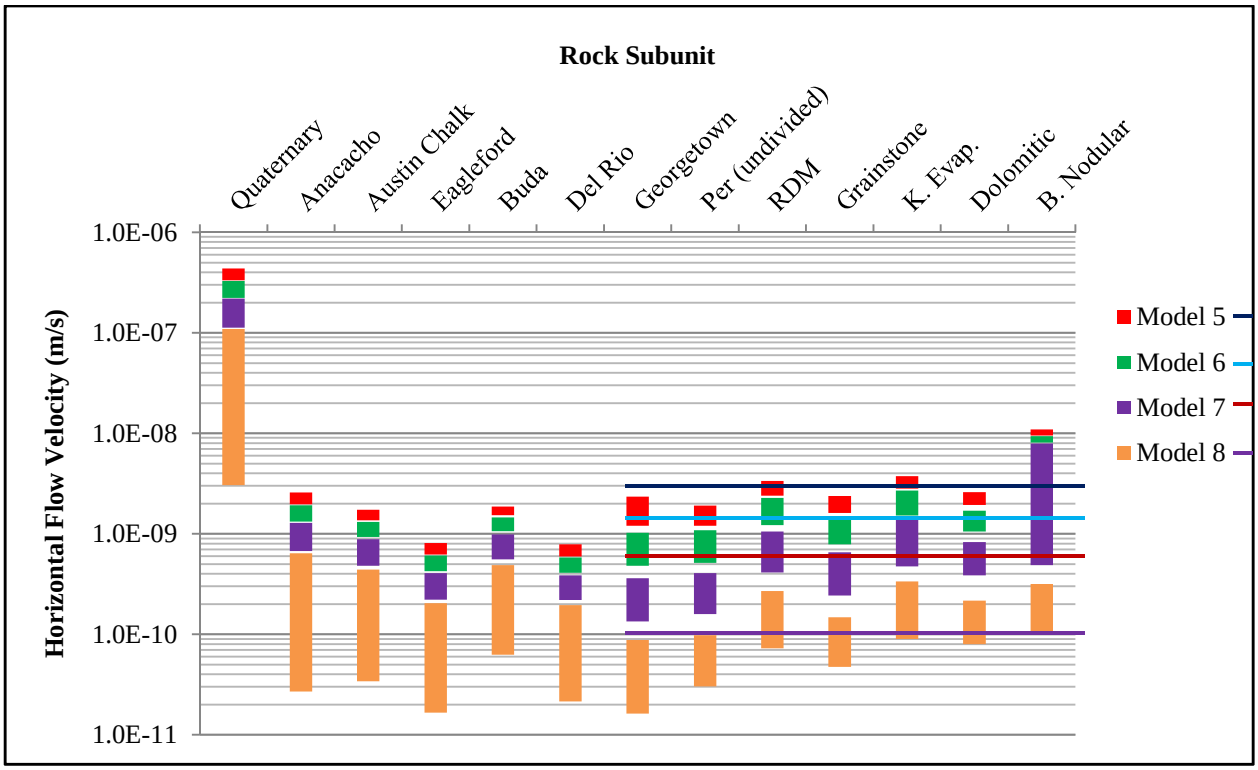

Figure 30. Horizontal flow velocity ranges for Models 5-8. Dark blue, light blue, dark red, and purple lines represent average horizontal flow velocity (m/s).

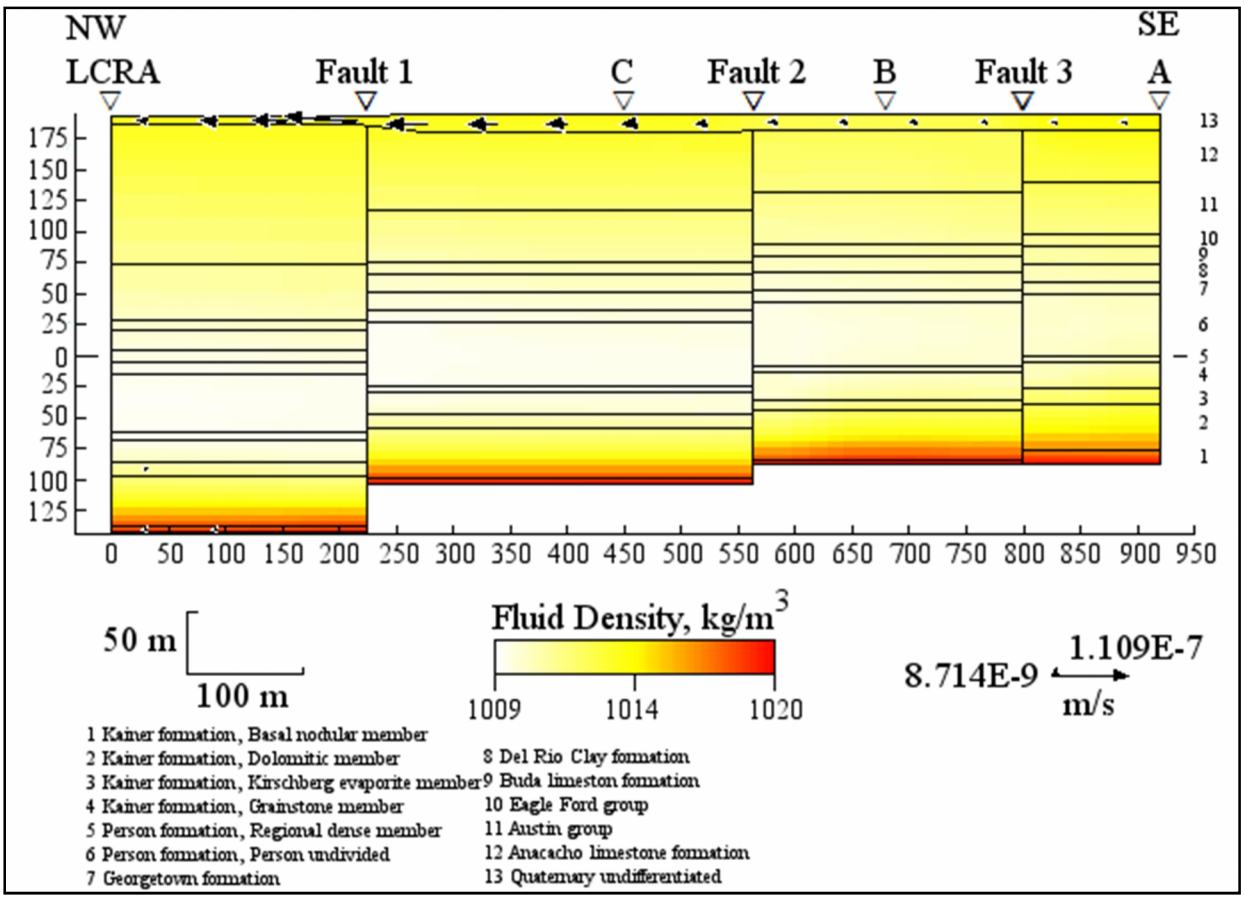

Figure 31. Model 6 is shown. Horizontal fault permeability is 0.001D and vertical fault permeability is 0.1 D, with reduced aquifer rock permeability of one order of magnitude.

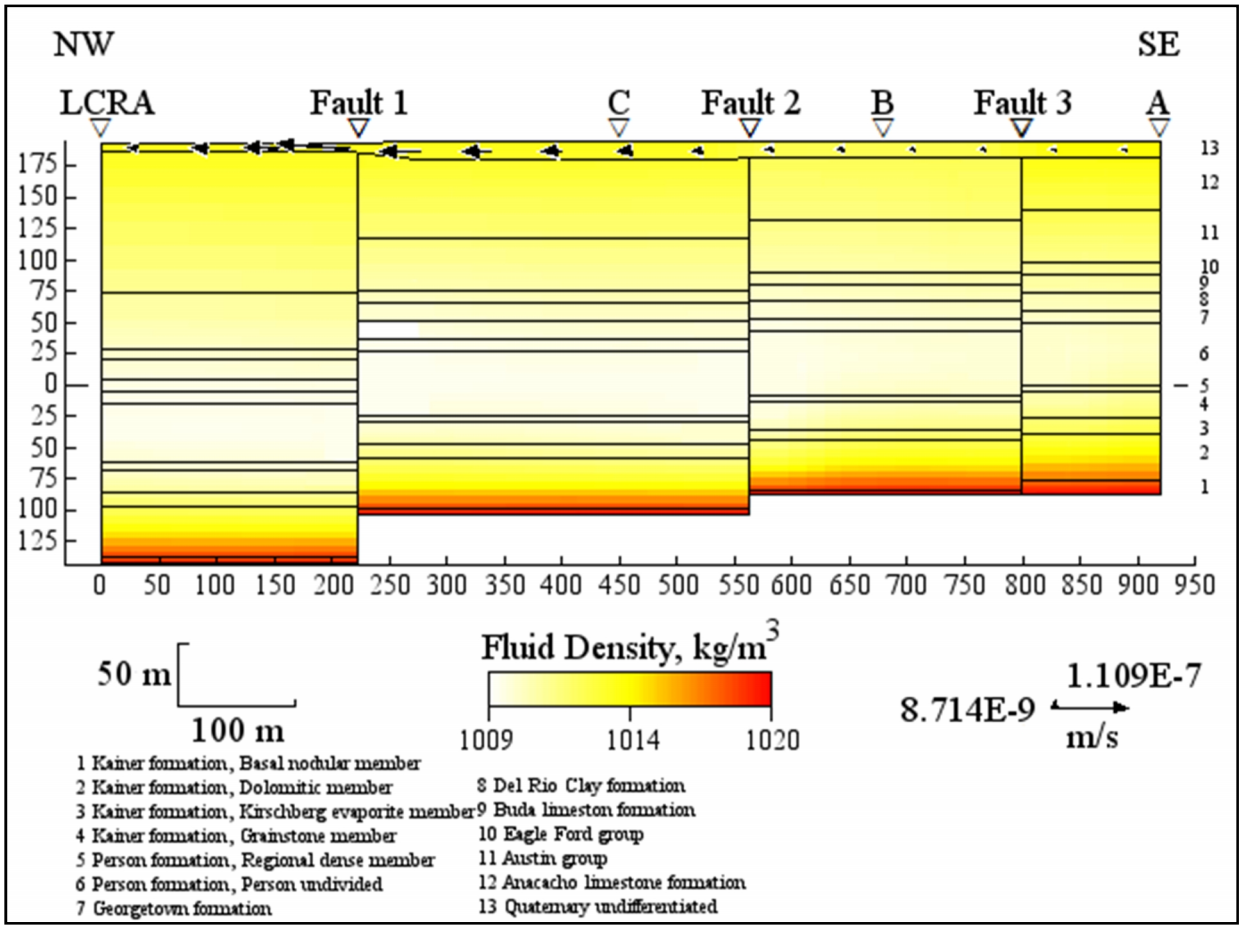

Figure 32. Model 7 is shown. Horizontal fault permeability is 0.001D and vertical fault permeability is 0.1 D, with reduced aquifer rock permeability of two orders of magnitude.

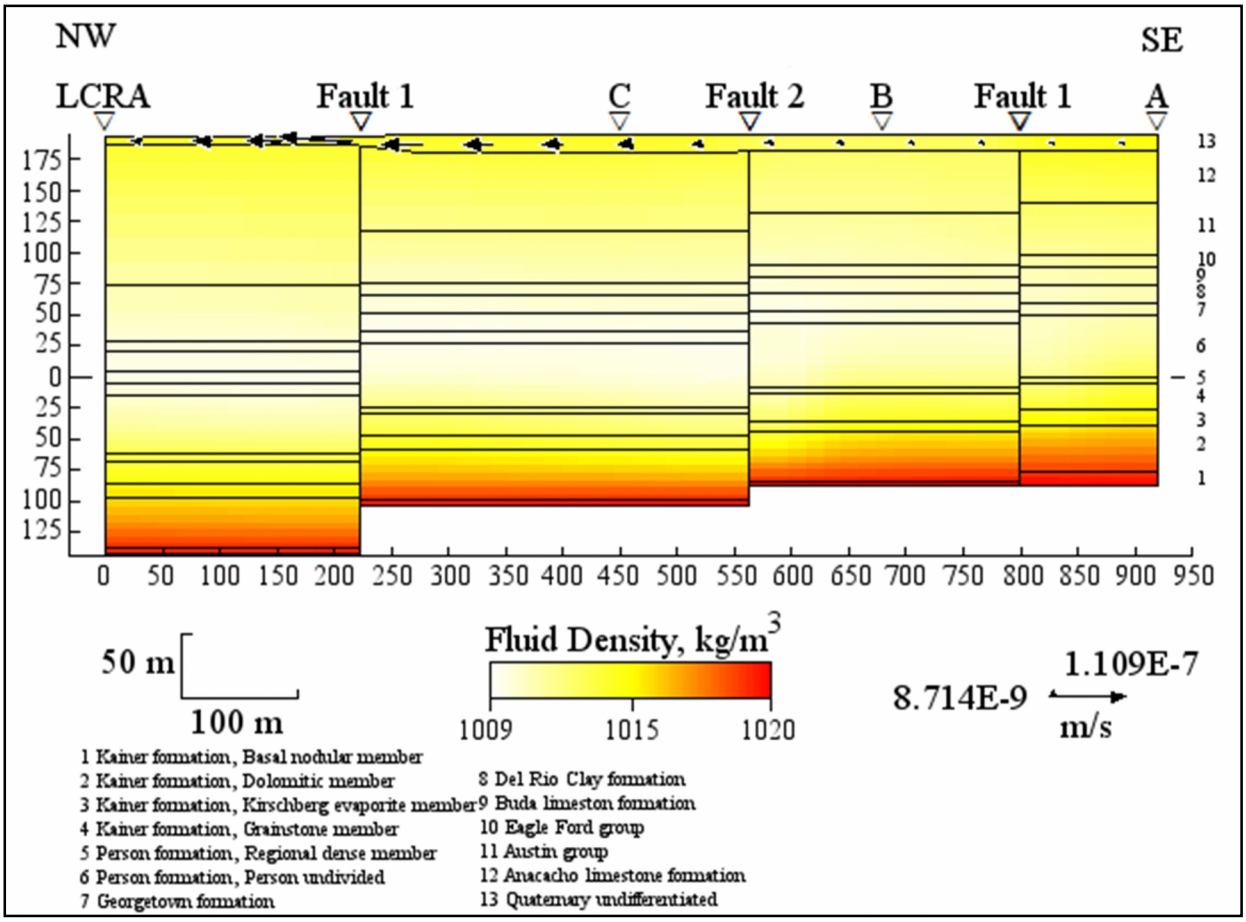

Figure 33. Model 8 is shown. Horizontal fault permeability is 0.001D and vertical fault permeability is 0.1 D, with reduced aquifer rock permeability of three orders of magnitude.

MODELS 9-12

For Models 9-12, horizontal fault permeability was set to 0.0001 D and vertical fault permeability was set to 0.1 D. In addition, aquifer rock permeability ranged from no reduction to three orders of magnitude reduction in permeability. Figure 34 shows average horizontal flow velocities, and Figure AD4 (Appendix D) shows average vertical flow velocities. In Figure 34, all models fall below the threshold of resolution for Basin2, meaning the fluid flow has shut down across the freshwater/saline-water interface. The blue, yellow, red, and purple lines represent average horizontal for Models 9-12. Average horizontal flow velocities are 6.0×10^{-9} (blue), 8.9×10^{-9} (yellow), 9.8×10^{-9} (red), and 7.5×10^{-10} (purple) m/s, respectively (Figure 34).

Average vertical flow velocities are $9.5x10^{-9}$, $4.0x10^{-10}$, $7.2x10^{-10}$, and $7.0x10^{-11}$ m/s, respectively (Appendix D: Figure AD4).

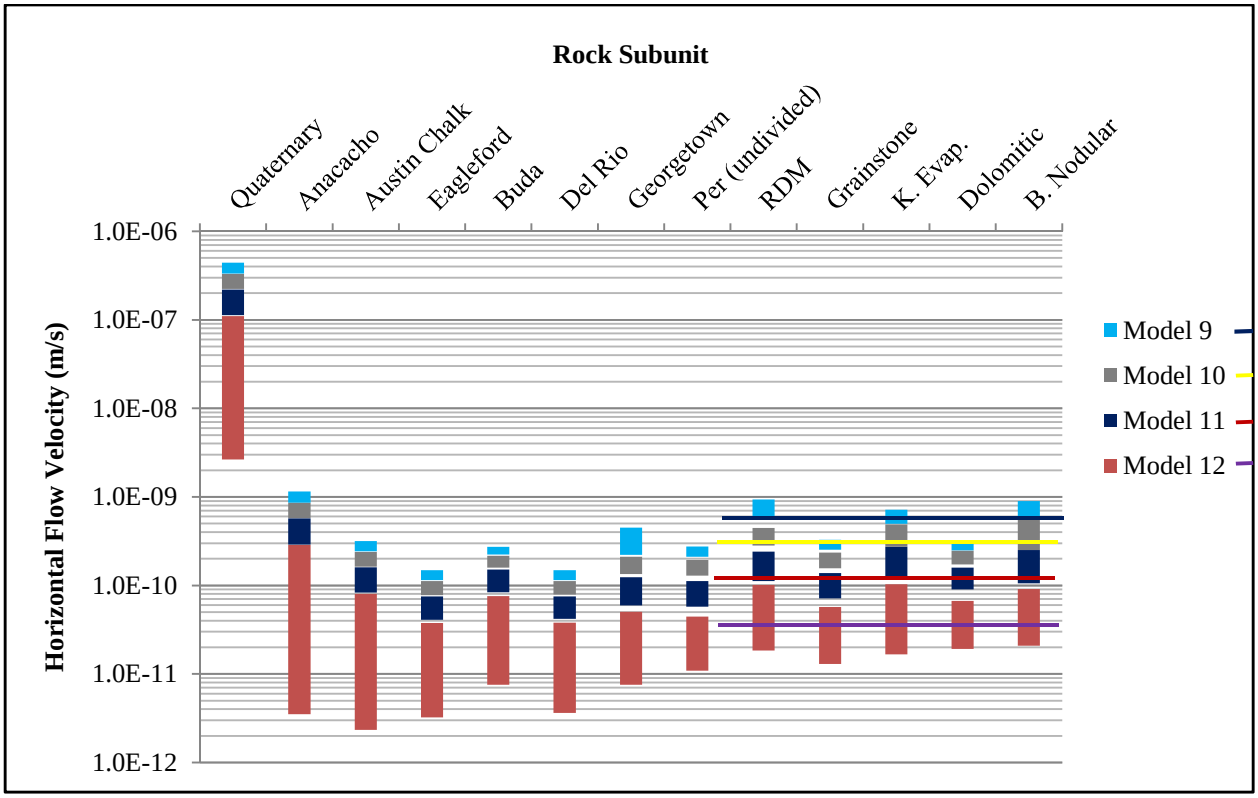

Figure 34. Horizontal flow velocity ranges for Models 9-10. Dark blue, yellow, dark red, and purple lines represent average horizontal flow velocity (m/s).

Models 9-12 (Figures 35-38) are very similar, in terms of fluid flow rates and fluid density distribution. Fluid flow has shut down across all transects, excluding the Quaternary subunit. Therefore, a horizontal fault permeability of 0.0001 D is too small to allow flow across the freshwater/saline-water interface, even in the Model 9, which had no reduced aquifer rock permeability. The only slight variation amongst these models is the color map, representing changes in fluid density. Models 9, 10, and 11 (Figures 35, 36, and 37, respectively) have a very small, centered distribution of reduced fluid density. Model 12 (Figure 38) has a more reduced fluid density area between the LCRA well and fault 2. However, compared to other models, the reduced fluid density area is still not significant. With flow shut down, diffusion is the primary

mechanism controlling fluid density distribution, which is why the reduced fluid density areas in the middle are much smaller.

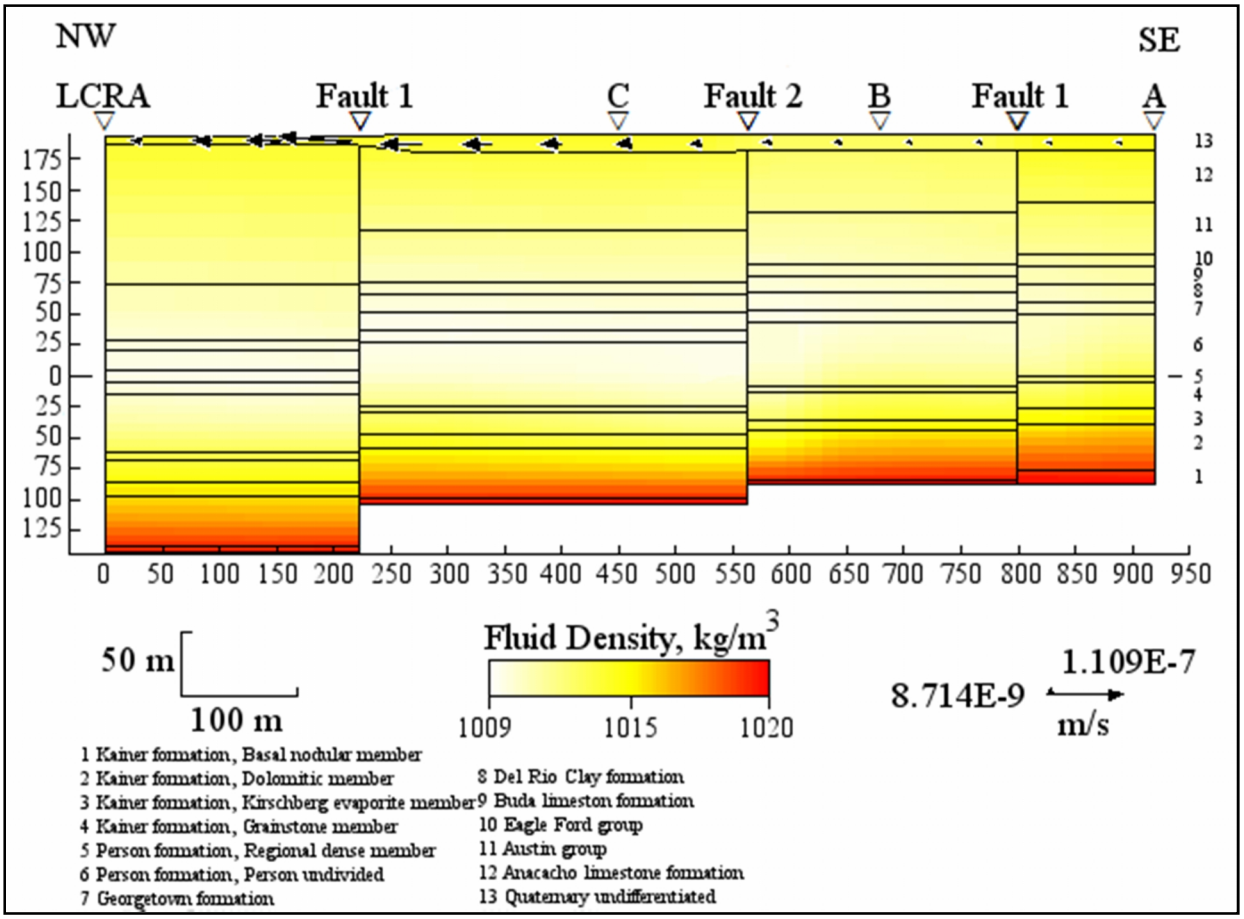

Figure 35. Model 9 is shown. Horizontal fault permeability is 0.0001D and vertical fault permeability is 0.1 D, with no reduced aquifer rock permeability.

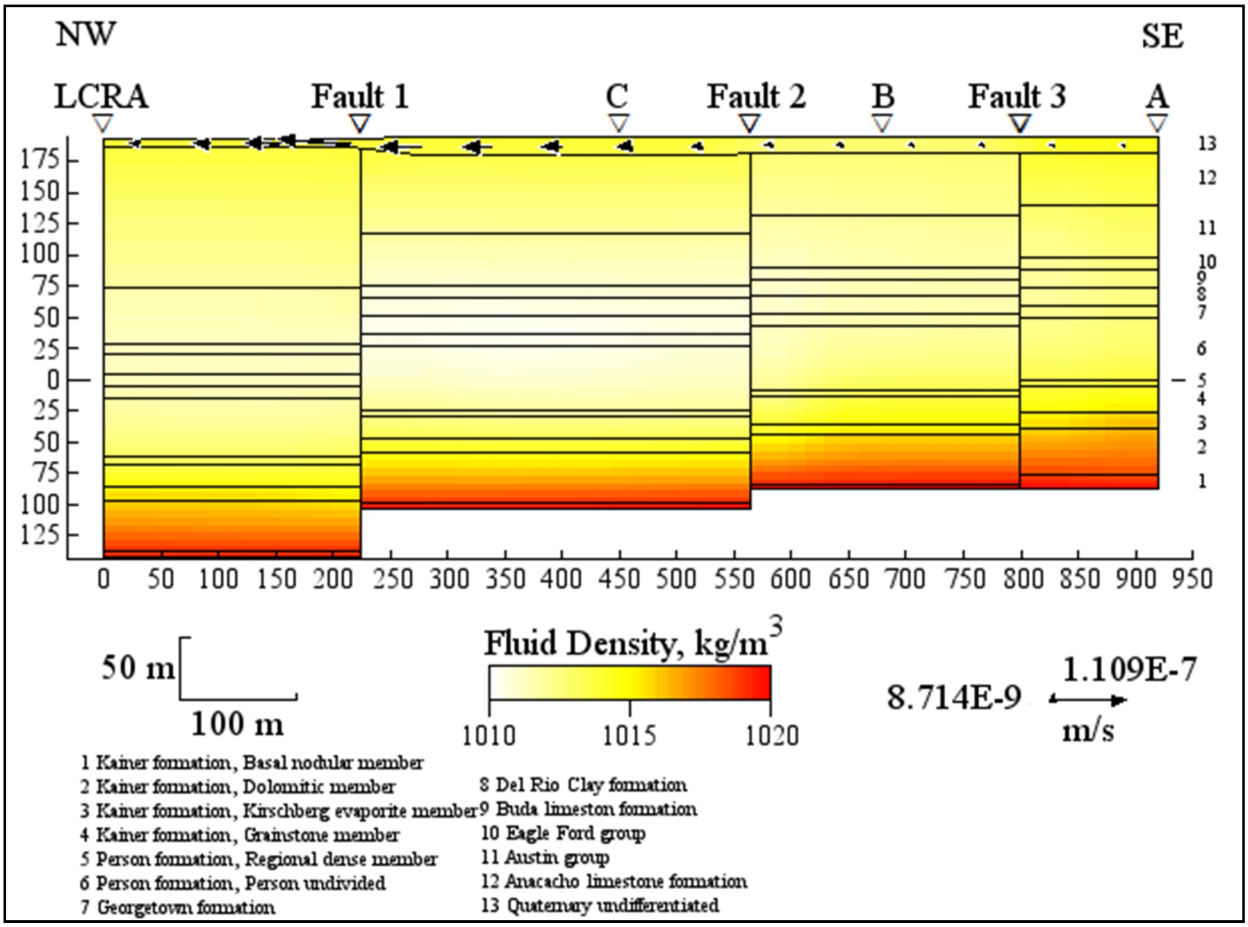

Figure 36. Model 10 is shown. Horizontal fault permeability is 0.0001D and vertical fault permeability is 0.1 D, with reduced aquifer rock permeability of one order of magnitude.

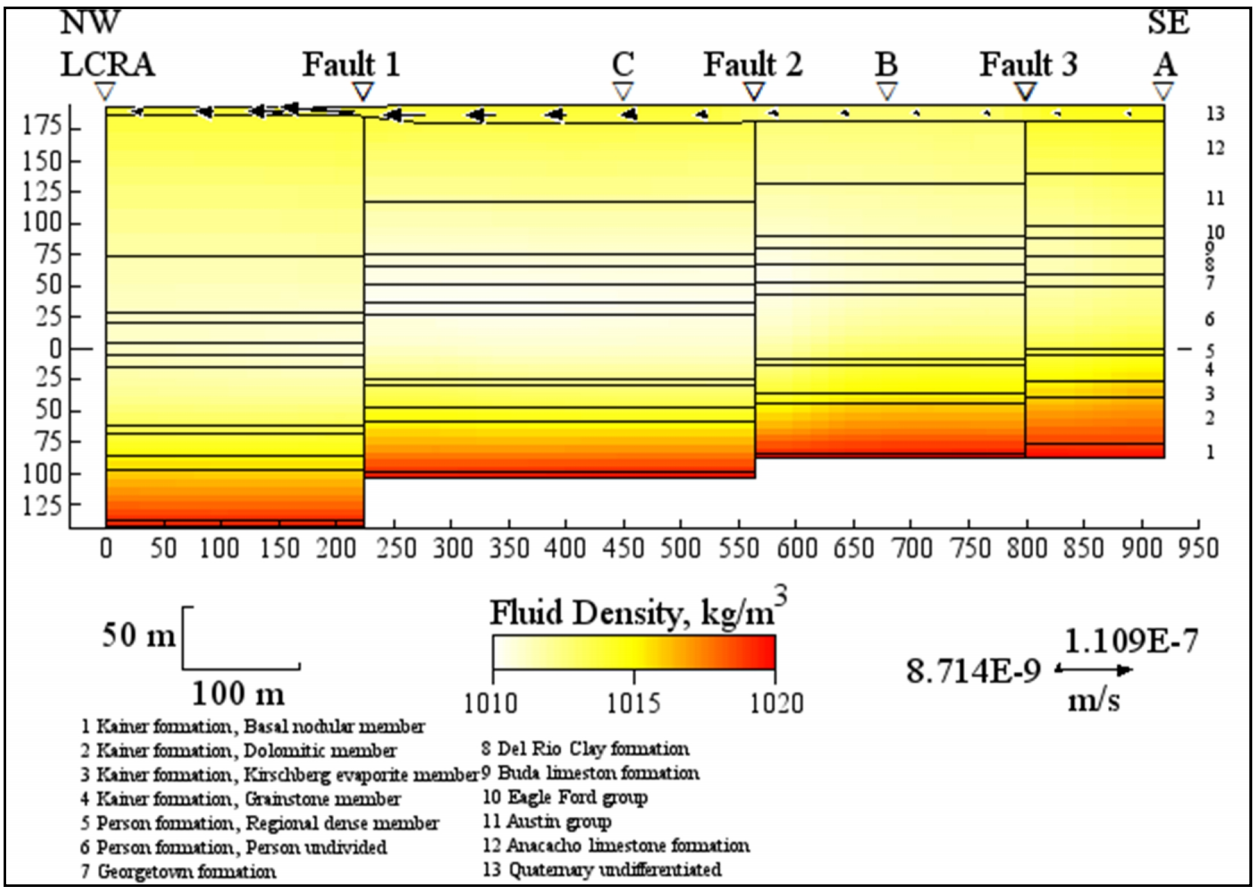

Figure 37. Model 11 is shown. Horizontal fault permeability is 0.0001D and vertical fault permeability is 0.1 D, with reduced aquifer rock permeability of two orders of magnitude.

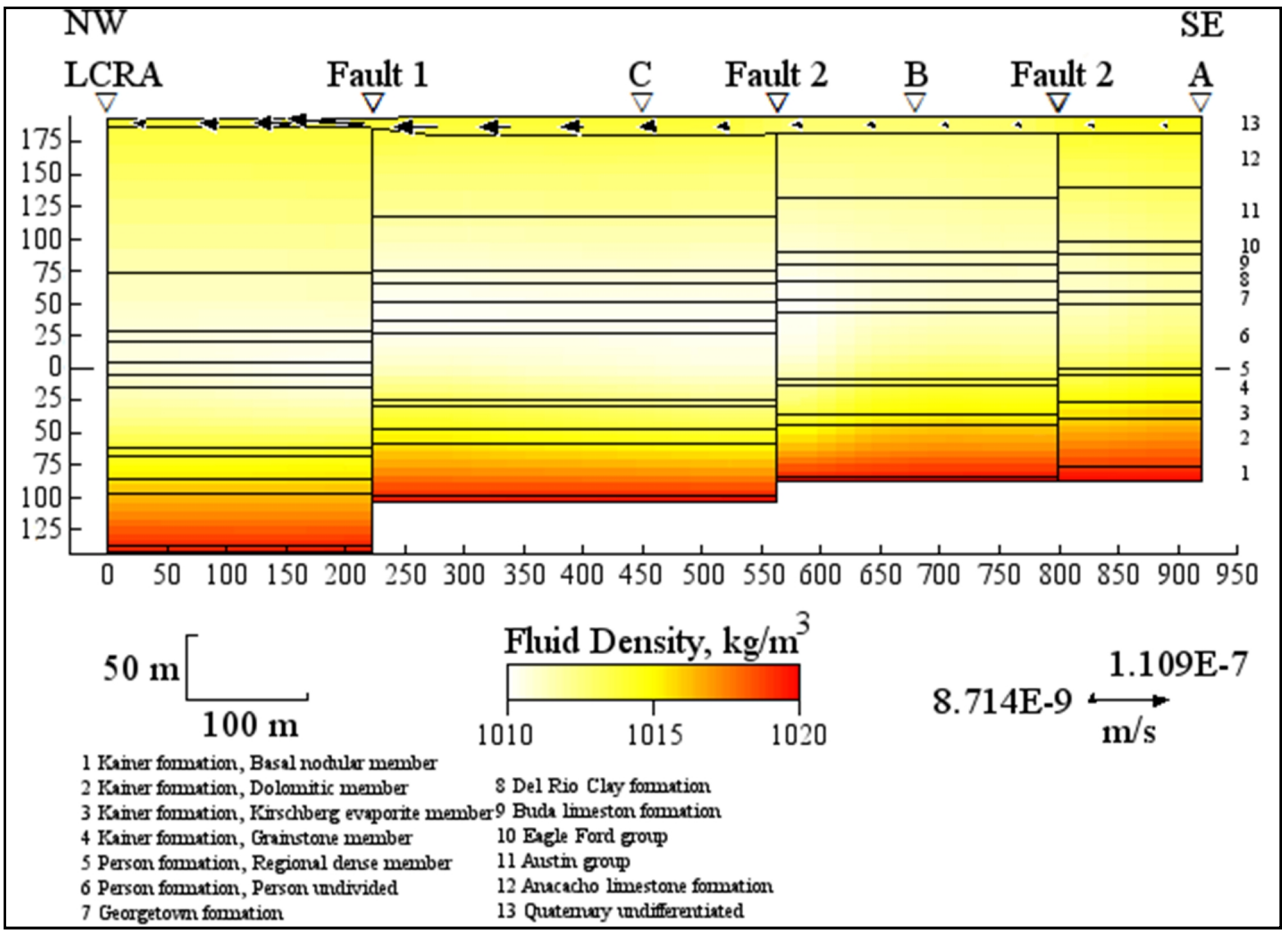

Figure 38. Model 12 is shown. Horizontal fault permeability is 0.0001D and vertical fault permeability is 0.1 D, with reduced aquifer rock permeability of three orders of magnitude.

DISCUSSION

MODEL LIMITATIONS

It should be noted that all models created along the transect are perpendicular to the actual flow of the Edwards aquifer. Figure 8 shows the potentiometric surfaces and flow paths of the aquifer. The aquifer flows from southwest to northeast, paralleling the “bad water” line. However, in order to test these hypotheses, a transect was required that cross-cut the “bad water” line perpendicularly. This ensured that the tested hypotheses could show all faults and wells, as well as get a cross-sectional view of the freshwater/saline-water interface. As the models are two dimensional models, the full three dimensional flow field is not represented. The two dimensional models allow us to investigate inhibition of flow across the freshwater/saline-water interface. It should also be noted that no other water wells with in the region followed the “bad water” line. Had data from other wells been available, a pseudo three dimensional study would have been undertaken. However, since no other well control within New Braunfels could be ascertained, this study was left with Wells A, B, C, and LCRA Well, running perpendicular to fluid flow. In addition, normal faults are treated as vertical due to limitations of Basin2. The Glen Rose limestone formation was chosen as the basal no flow boundary. However, there is connection between the Edwards aquifer and the underlying Trinity aquifer (Hunt et al., 2010).

HYPOTHESIS ONE

Based on all models and discussions, several overarching conclusions can be made from this study. Firstly, as both halite-saturation models indicated, extremely high fluid density will not inhibit fluid flow across the freshwater/saline-water interface. Fluid densities in these models were controlled primarily by salinity. Even when salinity was increased to halite-saturation

within the Kirschberg Evaporite member (6.5 molality or 380,000 ppm), fluid flow was still significant. In the second halite-saturation model, reduced fluid flow is seen, but this was due to reduced horizontal permeability. Increased fluid density can reduce the velocity of fluid flow to a certain extent, but it will not be a primary inhibitor to fluid flow. The Base Model had an average horizontal flow velocity of 9.0×10^{-6} m/s, whereas the first halite-saturation model had an average flow velocity of 2.5×10^{-7} m/s. So, bringing the Kirschberg Evaporite to halite-saturation only reduced the average horizontal velocities by less than one order of magnitude.

HYPOTHESIS TWO

Secondly, it is quite clear that horizontal fault permeability is the primary controlling factor in inhibiting fluid flow across the interface. In the Base Model, the horizontal and vertical fault permeability was 0.1 D. The 0.1 D for horizontal fault permeability was too high and readily allowed fluid flow across the transect. For Models 1-4, with 0.01 D horizontal fault permeability, significant flow still occurred. Only until the aquifer rock permeability had been reduced by three orders of magnitude did flow completely shut down for this set of models. When horizontal fault permeability reached 0.001 D for Models 5-8, flow shut down across the freshwater/saline-water interface. Model 5, which was not effected by reduced aquifer rock permeability, showed minimal fluid flow within the aquifer and no flow across the interface. For Models 9-12, no flow is seen because the threshold of shutting fluid flow down has already occurred in the previous set of models.

Ferrill et al. (2004) lists three ways in which faults and fractures in the BFZ alter flow paths and permeability: (1) faults and fractures offset stratigraphic units, thereby altering the entire geometry and communication between fault blocks, (2) faults and fractures inhibit, or provide pathways for, fluid flow or may, both, inhibit fluid flow in certain fault blocks, while

providing pathways for fluid flow in other fault blocks, and (3) permeability anisotropy is caused by faults and fractures deforming fault-blocks, with maximum permeability parallel to fault surfaces and minimum permeability perpendicular to fault surfaces. In addition, Ferrill et al. (2004) states that aquifer permeability is enhanced parallel to faults and decreased perpendicular to faults. In addition, Ferrill et al. (2004) suggested that the Del Rio Clay formation contributes clay smear to fault zones. The Edwards aquifer group in New Braunfels also contains significant volumes of shale (11-49%; based on V_{SH} calculations discussed earlier). Therefore, clay smear is also added to fault zones within the Edwards aquifer strata due to the argillaceous nature of the carbonate rocks.

Micarelli et al. (2006) also suggested four ways in which fault-related mechanisms contribute to reduction of porosity and, indirectly, permeability, in carbonate rocks: (1) pore collapse due to localized compaction and re-organization along grain boundaries, both macro- and micro-porosity, (2) grain crushing of empty fossil shells, (3) rotation-enhanced particle abrasion of larger particles during slip, and (4) precipitation of calcite cement in newly-formed fractures and in relict porosity. Micarelli et al. (2006) also identified two structural components that characterize normal faulted zones: a damaged zone and a fault core. Damaged zones contain rock volumes that are affected by fault-related fracturing (Micarelli et al., 2006). Fault cores usually contain cataclastic rocks because the majority of the displacement along the fault is accommodated during slip (Micarelli et al., 2006).

Micarelli et al. (2006) sampled several normal faulted surfaces from carbonate rocks for permeability values. All values ranged between 0.01 D and 0.0001 D, with the majority of samples with the lower 0.0001 D horizontal permeability value (Micarelli et al., 2006). The values from Micarelli et al. (2006) indicate that the horizontal fault permeability values seen in

this study (0.01 to 0.001 D) are consistent with those typically seen in carbonate and karstic rocks. Therefore, the horizontal fault permeability for the three faults tested along the New Braunfels transect range between 0.01 and 0.001 D, with fluid flow shutting down at 0.001 D.

HYPOTHESIS THREE

Thirdly, reducing the permeability of the aquifer stratigraphy does inhibit fluid flow across the freshwater/saline-water interface. However, it takes three orders of magnitude to shut down flow for Model 4, whereas the horizontal fault permeability was reduced by only two orders of magnitude from the Base Model to Model 5. This indicates that horizontal fault permeability is a greater factor in inhibiting flow across the interface than aquifer rock permeability.

TRIGGER

Since fault permeability is the major factor controlling the rate of fluid flow across the freshwater/saline-water interface, it is important to explore the mechanisms that could potentially increase fault permeability. Continued dissolution of the carbonate rocks from carbonic acid would increase fault permeability. The rate of carbonate dissolution depends on temperature, pH, and pCO_2 (Equation 8) (Ford and Williams, 2007):

Equation 8: $$\text{Rate}\ (\text{cm}^{-2} \cdot \text{s}^{-1}) = \text{k}_1 \cdot a_{\text{H}^+} + \text{k}_2 \cdot a_{\text{H}_2\text{CO}_3^0} + \text{k}_3 \cdot a_{\text{H}_2\text{O}} - \text{k}_4 \cdot a_{\text{Ca}^{2+}} \cdot a_{\text{HCO}_3^-}$$

where *a* represents activity and k_1, k_2, and k_3 are first order rate constants, which are temperature dependent ($\log k_1 = 0.98\text{-}444/T$, $\log k_2 = 2.84\text{-}217/T$, and $\log k_3 = -5.86\text{-}317/T$, where T is in Kelvin) (Ford and Williams, 2007). k_4 is approximated by the standard rate equations for calcite precipitation (Ford and Williams, 2007). Figure 30 shows the dissolution rates for carbonates, as

a function of pH. Based on Equation 8, dissolution along the fault surfaces at New Braunfels would take a significant amount of time. It most likely would take tens of thousands of years for dissolution to significantly increase the permeability of the fault surfaces. In addition, since little diagenesis in the saline water zone has been observed, dedolomitization is not a pressing issue for the saline water zone (Groschen and Buszka, 1997). This means that the permeability of the aquifer rock in the saline water zone will remain relatively constant for the foreseeable future.

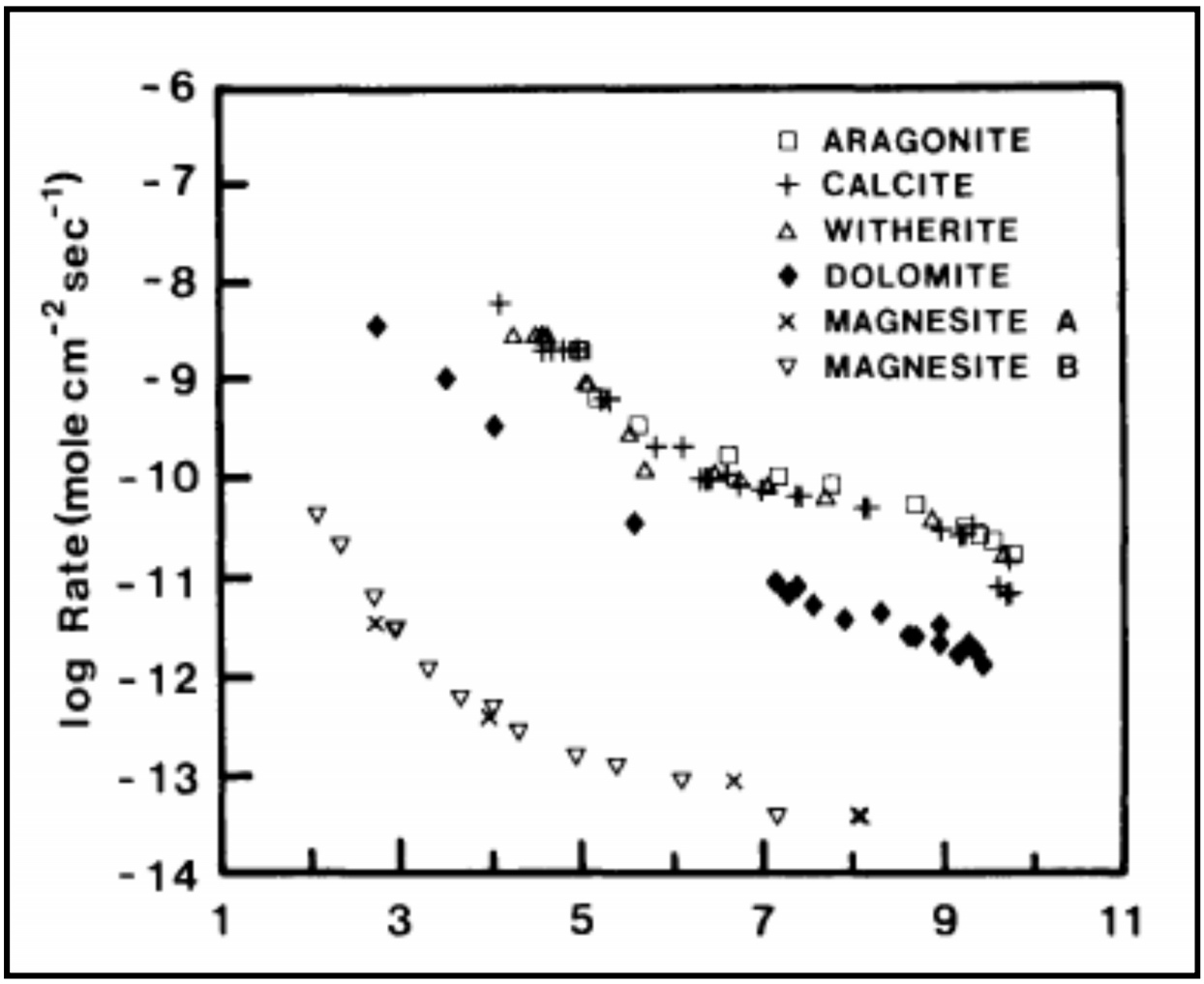

Figure 39. Dissolution rates for aragonite, calcite, witherite, dolomite, and magnesite A and B, as a function of pH. Image source: Morse and Mackenzie, 1990.

SUMMMARY & CONCLUSIONS

The karstic Edwards aquifer is located in south-central Texas. More than two million people rely on the Edwards aquifer within the San Antonio metropolitan area alone (Cox et al., 2009). The transect for this study comes from wells that run perpendicular to the freshwater/saline-water interface in New Braunfels, located between San Antonio and Austin. Geophysical well logs were used to construct models to determine the mechanisms that are, relatively, inhibiting fluid flow across this transect. Three hypotheses were tested. One: faults could be acting as a barrier between the freshwater and saline-water zones, preventing movement of the saline water into the freshwater zone. Two: the permeability of the bedrock in the saline water zone might be extremely low, limiting movement of the saline water. Three: an extremely saline water density might also prevent mixing across the interface. 2-D, variable-density, numerical models of groundwater flow (Basin2) were used to determine which factor (fault, permeability, or density) controls the lack of saline-water intrusion.

It is clear from each model that faults and their permeability, mainly horizontal permeability, is the primary controlling factor inhibiting fluid flow across the freshwater/saline-water interface. When horizontal fault permeability reached 0.01 D, flow was significantly reduced. When these values reached 0.001 D, flow across the interface ceased. Results from this study correlate well to those of Micarelli et al. (2006), which tested permeability values of normal faults within carbonate rocks (0.01 D for damaged zone and 0.0001 D for fault core). Dissolution of the carbonate rocks can increase the permeability of faults, but due to dissolution rates of carbonates, it could take tens of thousands of years to increase permeability. To a lesser extent, saline water zone permeability can control the movement of flow across this interface if the permeability values are reduced. Relatively little dedolomitization has occurred within the

saline-water zone, so permeability values within the saline-water zone are not going to increase within the foreseeable future. In addition, extremely high saline water densities are not going to cause movement across the interface. The halite-saturation models show, conclusively, that even when salinity is brought to halite-saturation within the Kirschberg Evaporite, significant flow still occurred. Fluid flow is only reduced by less than one order of magnitude.

The Edwards Aquifer Authority has been interested in the mechanisms controlling the fluid flow across the freshwater/saline-water interface for some time. Based on the results from this study, the primary inhibitor of fluid flow is horizontal fault permeability. An estimation of 0.001 D can be made for horizontal fault permeability and 0.1 D for vertical fault permeability for the three normal faults within the New Braunfels observation wells transect. Recommendations for future study include full drawdown tests within each well to determine drawdown versus time.

REFERENCES

Appelo, C.A.J., and Postma, D., 2005, Pollution by organic chemicals, *in* Appelo, C.A.J., and Postma, D. eds., Geochemistry, groundwater and pollution, A.A. Balkema, Leiden, Netherlands, 649 p.

Arfib, B., de Marsily, G., and Ganoulis, J., 2007, Locating the zone of saline intrusion in a coastal karst aquifer using springflow data: Ground Water, v. 45.1, p. 28-35.

Asquith, G., and D. Krygowski, 2004, Basic Well Log Analysis: AAPG Methods in Exploration 16, 244 p.

Barlow, P.M., and Wild, E.C., 2002, Bibliography on the occurrence and intrusion of saltwater in aquifers along the Atlantic coast of the United States: U.S. Geological Survey, Open-File Report 02-235, 32 p.

Bethke, C.M., Lee, M.-K., and Park, J., 2007, Basin modeling with Basin2: a guide to using the Basin2 software package: University of Illinois, 220 p.

Birdwell, J.E., and Engel, A.S., 2009, Variability in terrestrial and microbial contributions to dissolved organic matter fluorescence in the Edwards aquifer, central Texas: Journal of Cave and Karst Studies, v. 71.2, p. 144-156.

Cox, W.D., Meng, L., Khedun, P., Nordfelt, A., and Quiring, S.M., 2009, Discharge variability for an artesian spring of the Edwards Aquifer: Comal springs (1933-2007): International Journal of Climatology, v. 29, p. 2324-2336.

Essaid, H.I., 1986, A comparison of the coupled fresh water-salt water flow and the Ghyben-Herzberg sharp interface approaches to modeling of transient behavior in coastal aquifer systems: Journal of Hydrology, v. 86, p. 169-193.

Ewing, T.E., 1991, Structural framework, *in* Salvador, Amos, ed., The Gulf of Mexico Basin: Geological Society of America, Geology of North America, v. J, p. 31-52.

Ferrill, D.A., Morris, A.P., McGinnis, R.N., Smart, K.J., and Ward, W.C., 2011, Fault zone deformation and displacement partitioning in mechanically layered carbonates: the Hidden Valley fault, central Texas: AAPG Bulletin, v. 95.8, p. 1383-1397.

Ferrill, D.A., Sims, D.W., Waiting, D.J., Morris, A.P., Franklin, N.M., and Schultz, A.L., 2004, Structural framework of the Edwards Aquifer recharge zone in south-central Texas: Geological Society of America Bulletin, v. 116, p. 407-418.

Fleury, P., Bakalowicz, M., and de Marsily, G., 2007, Submarine springs and coastal karst aquifers: a review: Journal of Hydrology, v. 339, p. 79-92.

Ford, D., and Williams, P., 2007, Introduction to Karst: Karst Hydrogeology and Geomorphology, Chichester, West Sussex: Wiley, 562 p.

Freeze, R.A., and Witherspoon, P.A., 1967, Theoretical analysis of regional groundwater flow. II: Effects of water table configuration and subsurface permeability variations: Water Resources Research, v. 3, p. 623-634.

Groschen, G.E., and Buszka, P.M., 1997, Hydrogeologic framework and geochemistry of the Edward's aquifer saline-water zone, south-central Texas: U.S. Geological Survey, Water-Resources Investigations Report 97-4133, 47 p.

Hamilton, J.M., Esquilin, R., and Schindel, G.M., 2006, Ewards Aquifer Authority Synoptic Water Level Program, Report 2006-02, 120 p.

Harmon, R.S., and Wicks, C.M., 2006, Perspectives on Karst geomorphology, hydrology, and geochemistry: a tribute volume to Derek C. Ford and William B. White: Geological Society of America-Special Paper: 404, 76 p.

Hovorka, S.D., Mace, R.E., and Collins, E.W., 1995, Regional distribution of permeability in the Edward's Aquifer: Edward's Underground Water District Report 95-02, 127 p.

Hunt, A.G., Lambert, R.B., Fahlquist, L., 2010, Sources of groundwater based on Helium analysis in and near the Freshwater/Saline-water transition zone of the San Antonio segment of the Edwards aquifer, south-central Texas, 2002-03: U.S. Geologicial Survey, Scientific Investigations Report 2010-5030, 15 p.

Karst Waters Institute, 2011, Karst Waters Institute—What is Karst (and why is it important)?, <http://www.karstwaters.org/aboutkarst/index.php>. 29 January, 2011.

Keys, S., 1985, Borehole geophysics applied to ground-water investigations: USGS, Techniques of Water-Resources Investigations of the United States Geological Survey, 28 p.

Kimball, S., and Mattis, P., 2008, GNU Image Manipulation Program 2.6.11.

Land, L.S., and Prezbindowski, D.R., 1981, The origin and evolution of saline formation water, Lower Cretaceous carbonates, south-central Texas, U.S.A.: Journal of Hydrology, v. 54, p. 51-74.

Langmuir, D., 1997, Thermochemical Principles: *Aqueous Environmental Geochemistry*, Upper Saddle River, New Jersey: Prentice Hall, 602 p.

Larionov, V.V., 1969, Borehole radiometry: Moscow, U.S.S.R., Nedra.

Leve, G.W., 1983, Relation of concealed faults to water quality and the formation of solution features in the Floridan Aquifer, northeastern Florida, U.S.A.: Journal of Hydrology, v. 61, p. 251-264.

Lindgren, R.J., Dutton, A.R., Hovorka, S.D., Worthington, S.R.H., and Painter, S., 2004, Conceptualization and simulation of the Edwards Aquifer, San Antonio Region, Texas: U.S. Geological Survey, Scientific Investigations Report 2004-5277, 145 p.

Loáiciga, H.A., Maidment, D.R., and Valdes, J.B., 2000, Climate-change impacts in a regional karst aquifer, Texas, USA: Journal of Hydrology, v. 227, p. 173-194.

Maclay, R.W., and Small, T.A., 1983, Hydrostratigraphic subdivisions and fault barriers of the Edwards aquifer, south-central Texas, U.S.A.: Journal of Hydrology, v. 61, p. 127-146.

Maclay, R.W., and Small, T.A., 1984, Carbonate geology and hydrology of the Edwards aquifer in the San Antonio area, Texas: U.S. Geological Survey, Open-File Report 83-537, 72 p.

McCutcheon, S.C., Martin, J.L., Barnwell, T.O., Jr., 1993, Water Quality, *in* Maidment, D.R. ed., Handbook of Hydrology, McGraw-Hill, New York, NY, 1424 p.

Micarelli, L., Benedicto, A., and Wibberley, C.A.J., 2006, Structural evolution and permeability of normal fault zones in highly porous carbonate rocks: Journal of Structural Geology, v. 28, p. 1214-1227.

Miller, J.C., 1971, Groundwater resources of Saline County, Missouri: Missouri Geological Survey and Water Resources, Water Resources Report 26, 75 p.

Mitchell, M., 2002, Engauge Digitizer. < www.digitizer.sourceforge.net>. 2 May, 2012.

Morse, J.W., and Mackenzie, F.T., 1990, Geochemistry of sedimentary carbonates: Developments in Sedimentology, v. 48, 707 p.

Oetting, G.C., Banner, J.L., and Sharp, Jr, J.M., 1996, Regional controls on the geochemical evolution of saline groundwaters in the Edwards aquifer, central Texas: Journal of Hydrology, v. 181, p. 251-283.

Painter, S.L., Woodbury, A.D., and Jiang, Y., 2007, Transmissivity estimation for highly heterogeneous aquifers: comparison of three methods applied to the Edwards Aquifer, Texas, USA: Hydrogeology, v. 15, p. 315-331.

Scanlon, B.R., Mace, R.E., Barrett, M.E., and Smith, B., 2003, Can we simulate regional groundwater flow in a karst system using equivalent porous media models? Case study, Barton Springs Edwards aquifer, USA: Journal of Hydrology, v. 276, p. 137-158.

Schindel, G.M., Johnson, S.B., Johnson, E.C., Alexander, Jr., S.R.H., Worthington, S.D., Hovorka, S.D., Kreitler, C.W., and Pedler, W.H., 2005, An introduction to the Balcones Fault Zone segment of the Edwards Aquifer in south-central Texas: Edwards Aquifer Authority Report, 66 p.

APPENDIX A

Table AA1. Formation tops, thicknesses, water depth, V_{SH}, arithmetically average porosities, and intrinsic permeabilities for Well A.

Well A										
Unit	**Subunit**	**Subunit Top (m)**	**Top (m)**	**Subunit Thickness (m)**	**Total Thickness (m)**	**Water Depth (m)**	**I_{GR}**	**V_{SH}**	**Average ϕ**	**k_x (D)**
Quaternary			1.52		11.28	11.28	0.53	0.36		
Anacacho			12.80		50.29	50.29	0.48	0.31		
Austin			63.09		41.45	41.45	0.30	0.17		
Eagleford			104.55		8.84	8.84	0.55	0.38		
Buda			113.39		13.41	13.41	0.55	0.37		
Del Rio			126.80		14.02	14.02	0.57	0.40		
Georgetown			140.82		9.75	9.75	0.23	0.12	0.18	0.13
Person	Undivided	150.57	150.57	50.29	55.47	55.47	0.25	0.13	0.26	0.37
	Regional Dense	200.86		5.18			0.38	0.23	0.07	0.35
Kainer	Grainstone	206.04	206.04	21.34	73.15	73.15	0.47	0.30	0.27	0.98
	Kirshberg Evaporite	227.38		9.14			0.61	0.44	0.21	2.73
	Dolomitic	236.52		38.40			0.45	0.29	0.22	1.79
	Basal Nodular	274.93		4.27			0.53	0.35	0.26	1.79

Table AA2. Formation tops, thicknesses, water depth, V_{SH}, arithmetically average porosities, and intrinsic permeabilities for Well B.

Well B										
Unit	**Subunit**	**Subunit Top (m)**	**Top (m)**	**Subunit Thickness (m)**	**Total Thickness (m)**	**Water Depth (m)**	**I_{GR}**	**V_{SH}**	**Average ϕ**	**k_x (D)**
Quaternary			1.52		1.52	-193.55	0.53	0.36		
Anacacho			12.80		12.80	-143.26	0.48	0.31		
Austin			63.09		63.09	-101.80	0.30	0.17		
Eagleford			104.55		104.55	-92.96	0.55	0.38		
Buda			113.39		113.39	-79.55	0.55	0.37		
Del Rio			126.80		126.80	-65.53	0.57	0.40		
Georgetown			140.82		140.82	-55.78	0.23	0.12	0.18	0.13
Person	Undivided	150.57	150.57	50.29	150.57	-5.49	0.25	0.13	0.26	0.37
	Regional Dense	200.86		5.18		-0.30	0.38	0.23	0.07	0.35
Kainer	Grainstone	206.04	206.04	21.34	206.04	21.03	0.47	0.30	0.27	0.98
	Kirshberg Evaporite	227.38		9.14		30.18	0.61	0.44	0.21	2.73
	Dolomitic	236.52		38.40		68.58	0.45	0.29	0.22	1.79
	Basal Nodular	274.93		4.27		72.85	0.53	0.35	0.26	1.79

Table AA3. Formation tops, thicknesses, water depth, V_{SH}, arithmetically average porosities, and intrinsic permeabilities for Well C.

Well C										
Unit	**Subunit**	**Subunit Top (m)**	**Top (m)**	**Subunit Thickness (m)**	**Total Thickness (m)**	**Water Depth (m)**	**I_{GR}**	**V_{SH}**	**Average ϕ**	**k_x (D)**
Quaternary			0.00		13.41	-193.55	0.44	0.28		
Anacacho			13.41		62.18	-131.37	0.47	0.30		
Austin			75.59		42.06	-89.31	0.45	0.29		
Eagleford			117.65		8.53	-80.77	0.46	0.29		
Buda			126.19		14.63	-66.14	0.59	0.42		
Del Rio			140.82		13.41	-52.73	0.55	0.38		
Georgetown			154.23		10.36	-42.37	0.20	0.11	0.31	0.15
Person	Undivided	164.59	164.59	50.60	55.47	8.23	0.28	0.16	0.25	0.39
	Regional Dense	215.19		4.88		13.11	0.38	0.23	0.08	1.02
Kainer	Grainstone	220.07	220.07	16.76	72.24	29.87	0.41	0.25	0.25	1.12
	Kirshberg Evaporite	236.83		11.28		41.15	0.59	0.42	0.26	0.84
	Dolomitic	248.11		39.62		80.77	0.43	0.27	0.23	2.04
	Basal Nodular	287.73		4.57		85.34	0.59	0.42	0.17	0.40

Table AA4. Formation tops, thicknesses, water depth, V_{SH}, arithmetically average porosities, and intrinsic permeabilities for LCRA Well.

LCRA Well										
Unit	**Subunit**	**Subunit Top (m)**	**Top (m)**	**Subunit Thickness (m)**	**Total Thickness (m)**	**Water Depth (m)**	**I_{GR}**	**V_{SH}**	**Average ϕ**	**k_X (D)**
Quaternary			0.00		6.40	-192.02	0.41	0.25		
Anacacho			6.40		110.03	-81.99	0.62	0.44		
Austin			116.43		44.20	-37.80	0.25	0.14		
Eagleford			160.63		8.23	-29.57	0.43	0.27		
Buda			168.86		15.54	-14.02	0.47	0.31		
Del Rio			184.40		11.28	-2.74	0.40	0.25		
Georgetown			195.68		9.14	6.40	0.28	0.15	0.22	
Person	Undivided	204.83	204.83	46.94	52.43	53.34	0.41	0.25	0.25	
	Regional Dense	251.76		5.49		58.83	0.66	0.49	0.08	
Kainer	Grainstone	257.25	257.25	17.37	72.85	76.20	0.31	0.18	0.26	
	Kirshberg Evaporite	274.62		11.28		87.48	0.43	0.27	0.17	
	Dolomitic	285.90		39.62		127.10	0.43	0.27	0.23	
	Basal Nodular	325.53		4.57		131.67	0.59	0.42	0.21	

APPENDIX B

Table AB1. Measured porosity and calculated permeability values from Hovorka et al. 1995.

Kainer: Basal Nodular			
Well	**Average Porosity**	**Permeability (D)**	**Log Perm (log D)**
A	0.21	2.7753	0.443309936
B	0.26	1.7944	0.253919261
C	0.21	2.7753	0.443309936
Kainer: Basal Nodular			
Well	**Average Porosity**	**Permeability (D)**	**Log Perm (log D)**
A	0.25	2.9975	0.476759192
B	0.22	1.7944	0.253919261
C	0.23	2.0436	0.310395894
Kainer: Kirschberg Evaporite			
Well	**Average Porosity**	**Permeability (D)**	**Log Perm (log D)**
A	0.22	1.7176	0.234922031
B	0.21	2.7279	0.435828446
C	0.26	0.8432	-0.074069402
Kainer: Grainstone			
Well	**Average Porosity**	**Permeability (D)**	**Log Perm (log D)**
A	0.26	0.4697	-0.32817944
B	0.27	0.9807	-0.008463825
C	0.25	1.1195	0.049024098
Person: Regional Dense Member			
Well	**Average Porosity**	**Permeability (D)**	**Log Perm (log D)**
A	0.08	0.3596	-0.444180317
B	0.07	0.3517	-0.453827632
C	0.08	1.0246	0.010554352
Person: Undivided			
Well	**Average Porosity**	**Permeability (D)**	**Log Perm (log D)**
A	0.24	0.4207	-0.376027488
B	0.26	0.3676	-0.434624497
C	0.25	0.3856	-0.413862975
Georgetown			
Well	**Average Porosity**	**Permeability (D)**	**Log Perm (log D)**
A	0.17	0.2322	-0.634137785
B	0.18	0.1321	-0.879097182

Table AB1 continued.

C	0.31	0.1454	-0.837435593

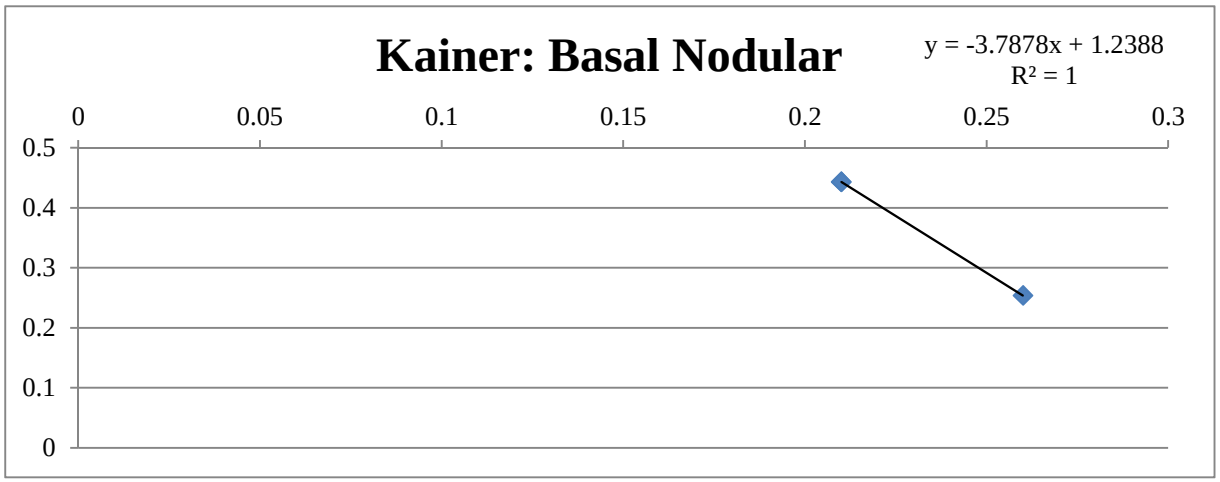

Figures AB1-AB3. Graphs showing log permeability versus porosity.

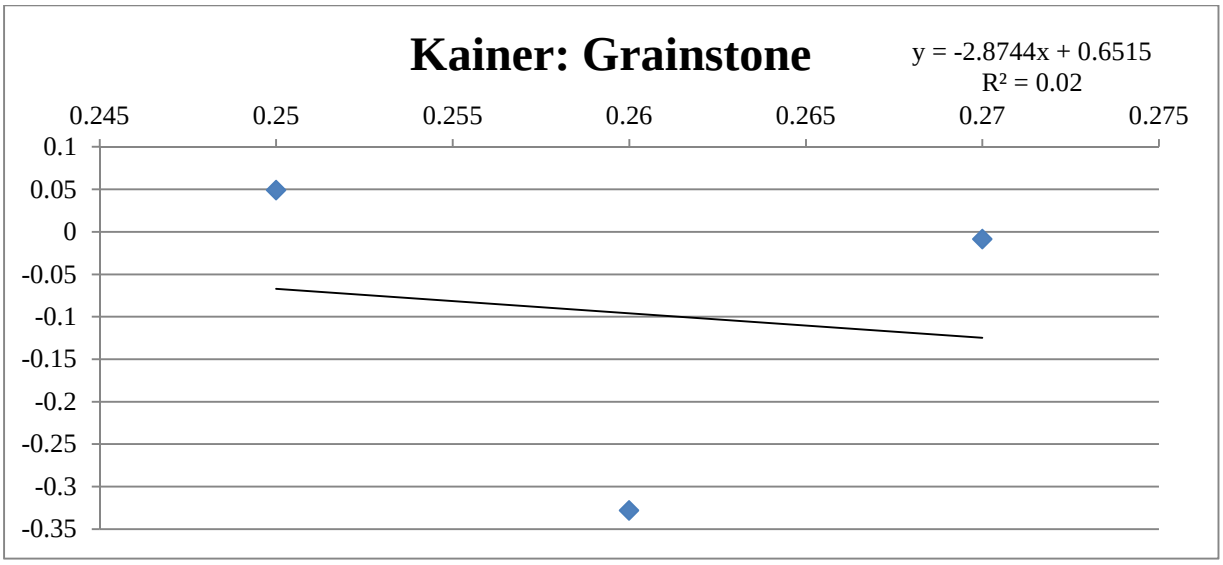
Kainer: Grainstone
y = -2.8744x + 0.6515
R² = 0.02
0.245
0.25
0.255
0.26
0.265
0.27
0.275
0.1
0.05
0
-0.05
-0.1
-0.15
-0.2
-0.25
-0.3
-0.35

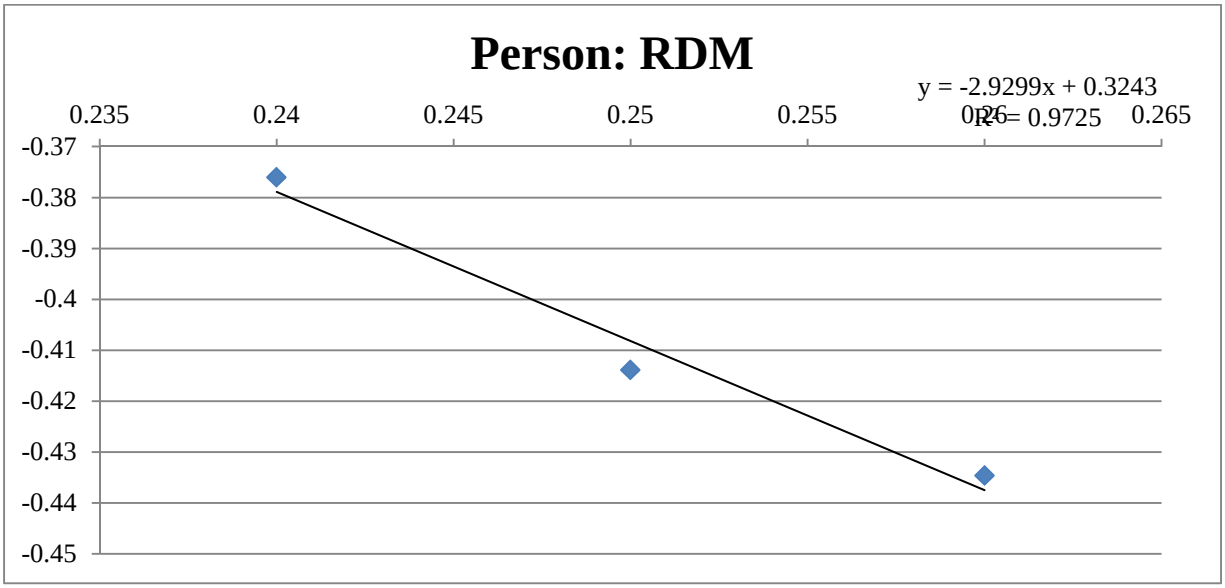
Person: RDM
y = -2.9299x + 0.3243
R² = 0.9725
0.235
0.24
0.245
0.25
0.255
0.26
0.265
-0.37
-0.38
-0.39
-0.4
-0.41
-0.42
-0.43
-0.44
-0.45

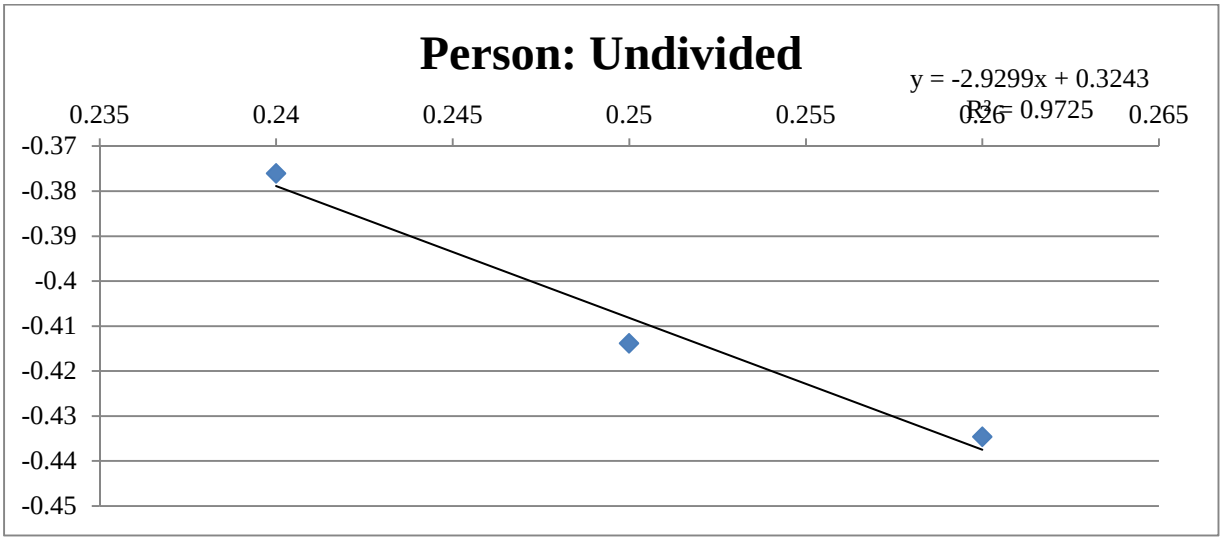
Person: Undivided
y = -2.9299x + 0.3243
R² = 0.9725
0.235
0.24
0.245
0.25
0.255
0.26
0.265
-0.37
-0.38
-0.39
-0.4
-0.41
-0.42
-0.43
-0.44
-0.45

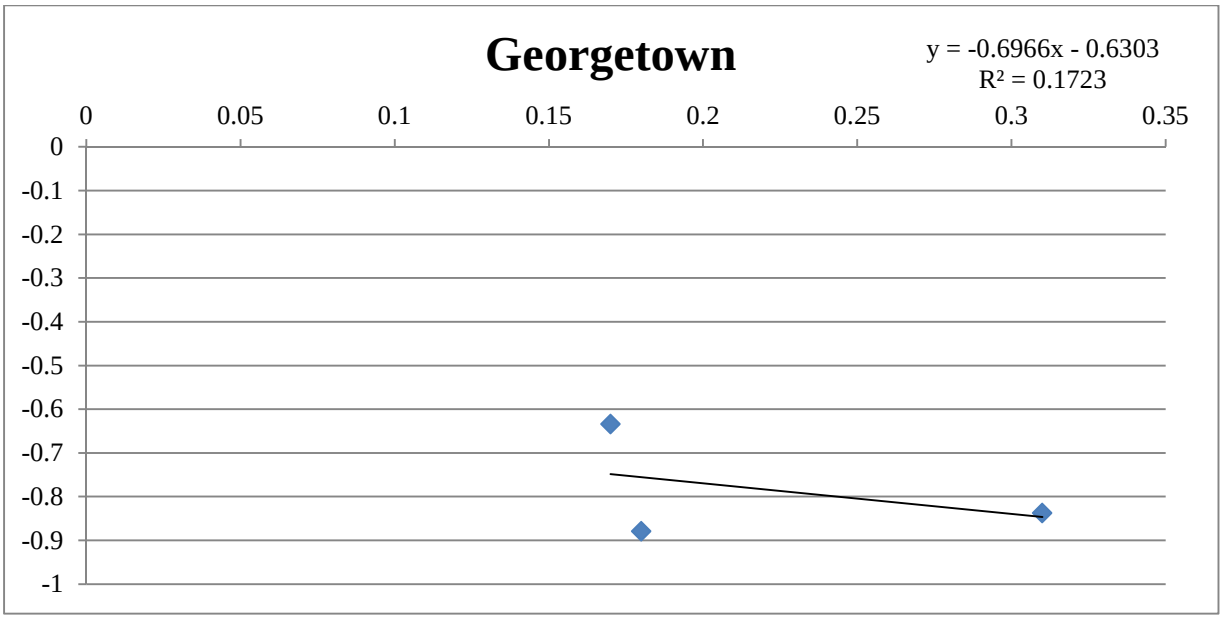

Figures AB4-AB7. Graphs showing log permeability versus porosity.

APPENDIX C

BASE MODEL INPUT FILE

```
run = steady; reference = compacted; concentration = full; flow = full; temperature = full;
residence_time = on; tables = all;
under_relax = 0.01;
x_well (m)      0       224.9 225       225.1   450     564.9   565     565.1   680     799.9 800
        800.1   920
well_name 'LCRA' '' 'Fault 1' '' 'C' ''    'Fault 2' '' 'B' '' 'Fault 3' '' 'A'
rock bas
        phi0 = 21.3%; phi1 = 0; A_perm = -3.7878;
        B_perm = 1.2388 log_darcy; rho_rk = 2.71 g/cm3;
        p_kxkz = 100
rock dol
        phi0 = 23.3%; phi1 = 0; A_perm = 7.5552;
        B_perm = -1.4158 log_darcy; rho_rk = 2.877 g/cm3;
        p_kxkz = 100
rock ev
        phi0 = 21.5%; phi1 = 0; A_perm = -9.4913;
        B_perm = 2.3819 log_darcy; rho_rk = 2.96 g/cm3;
        p_kxkz = 100;
rock grs
        phi0 = 26%; phi1 = 0; A_perm = -2.8744;
        B_perm = 0.6515 log_darcy; rho_rk = 2.71 g/cm3;
        p_kxkz = 100
rock rdm
        phi0 = 8%; phi1 = 0; A_perm = -2.9299;
        B_perm = 0.3243 log_darcy; rho_rk = 2.71 g/cm3;
        p_kxkz = 100
rock per
        phi0 = 25%; phi1 = 0; A_perm = -2.9299;
        B_perm = 0.3243 log_darcy; rho_rk = 2.71 g/cm3;
        p_kxkz = 100
rock gtn
        phi0 = 22%; phi1 = 0; A_perm = -0.6966;
        B_perm = -0.6303 log_darcy; rho_rk = 2.71 g/cm3;
        p_kxkz = 100
left = open; right = open;
strat 'Kainer, Basal Nodular'
        t_dep = -105.5 m.y.
```

column	thickness(m)	x(bas)	x(sh)	dep_wat(m)	t_surf	c_surfw
w (1:2)	4.57	.58	.42	131.67	27.68	.4277
w (3:7)	4.57	.58	.42	85.34	27.68	.4277
w (8:10)	4.27	.65	.35	72.85	30.50	.0119
w (11:13)	11.89	.76	.24	71.93	29.81	.0155

strat 'Kainer, Dolomitic'

t_dep = -104.34 m.y.

column	thickness(m)	x(dol)	x(sh)	dep_wat(m)	t_surf	c_surfw
w (1:2)	39.62	.73	.27	127.10	27.43	.0856
w (3:7)	39.62	.73	.27	80.77	27.43	.0856
w (8:10)	38.40	.71	.29	68.58	29.85	.0052
w (11:13)	36.27	.74	.26	60.05	29.42	.0154

strat 'Kainer, Kirshberg Evaporite'

t_dep = -103.17 m.y.

column	thickness(m)	x(ev)	x(sh)	dep_wat(m)	t_surf	c_surfw
w (1:2)	11.28	.73	.27	87.48	26.93	.0023
w (3:7)	11.28	.58	.42	41.15	26.93	.0023
w (8:10)	9.14	.56	.44	30.18	29.00	.0025
w (11:13)	12.19	.64	.36	23.77	28.28	.0095

strat 'Kainer, Grainstone'

t_dep = -102 m.y.

column	thickness(m)	x(grs)	x(sh)	dep_wat(m)	t_surf	c_surfw
w (1:2)	17.37	.82	.18	76.20	26.90	.0022
w (3:7)	16.76	.75	.25	29.87	26.90	.0022
w (8:10)	21.34	.70	.30	21.03	28.85	.0018
w (11:13)	20.12	.73	.27	11.58	28.04	.0073

strat 'Person, Regional Dense'

t_dep = -100.5 m.y.

column	thickness(m)	x(rdm)	x(sh)	dep_wat(m)	t_surf	c_surfw
w (1:2)	5.49	.51	.49	58.83	26.80	.0021
w (3:7)	4.88	.77	.23	13.11	26.80	.0021
w (8:10)	5.18	.77	.23	-0.30	28.70	.0017
w (11:13)	5.18	.71	.29	-8.53	27.62	.0075

strat 'Person, Undivided'

t_dep = -98.5 m.y.

column	thickness(m)	x(per)	x(sh)	dep_wat(m)	t_surf	c_surfw
w (1:2)	46.94	.75	.25	53.34	26.68	.0021
w (3:7)	50.60	.84	.16	8.23	26.68	.0021
w (8:10)	50.29	.87	.13	-5.49	28.48	.0017
w (11:13)	50.29	.74	.26	-13.72	27.38	.0075

strat 'Georgetown'

t_dep = -96.5 m.y.

column	thickness(m)	x(gtn)	x(sh)	dep_wat(m)	t_surf	c_surfw
w (1:2)	9.14	.85	.15	6.40	26.05	.0034
w (3:7)	10.36	.89	.11	-42.37	26.05	.0034
w (8:10)	9.75	.88	.12	-55.78	26.90	.0024
w (11:13)	9.45	.89	.11	-64.01	25.54	.0072

strat 'Del Rio'

t_dep = -95.5 m.y.

column	thickness(m)	x(ss)	x(sh)	dep_wat(m)	t_surf	c_surfw
w (1:2)	9.14	0	1	-2.74	25.85	.0042
w (3:7)	13.41	0	1	-52.73	25.85	.0042

w (8:10)	14.02	0	1	-65.53	26.50	.0024
w (11:13)	13.41	0	1	-73.46	25.34	.0071

strat 'Buda'

t_dep = -95 m.y.

column	thickness(m)	x(cn)	x(sh)	dep_wat(m)	t_surf	c_surfw
w (1:2)	15.54	.69	.31	-14.02	25.70	.0043
w (3:7)	14.63	.58	.42	-66.14	25.70	.0043
w (8:10)	13.41	.63	.37	-79.55	26.50	.0027
w (11:13)	14.63	.76	.24	-86.87	24.90	.0070

strat 'Eagleford'

t_dep = -89.3 m.y.

column	thickness(m)	x(ss)	x(sh)	dep_wat(m)	t_surf	c_surfw
w (1:2)	8.23	0	1	-29.57	25.50	.0046
w (3:7)	8.53	0	1	-80.77	25.50	.0046
w (8:10)	8.84	0	1	-92.96	26.00	.0029
w (11:13)	8.53	0	1	-101.50	24.49	.0070

strat 'Austin Chalk'

t_dep = -78 m.y.

column	thickness(m)	x(cn)	x(sh)	dep_wat(m)	t_surf	c_surfw
w (1:2)	44.2	.86	.14	-37.80	25.65	.0048
w (3:7)	42.06	.71	.29	-89.31	25.65	.0048
w (8:10)	41.45	.83	.17	-101.80	25.85	.0029
w (11:13)	41.76	.77	.23	-110.03	24.24	.0070

strat 'Anacacho'

t_dep = -75 m.y.

column	thickness(m)	x(cn)	x(sh)	dep_wat(m)	t_surf	c_surfw
w (1:2)	110.03	.56	.44	-81.99	25.30	.0027
w (3:7)	62.18	.70	.30	-131.37	25.30	.0027
w (8:10)	50.29	.69	.31	-143.26	24.75	.0034
w (11:13)	41.76	.75	.25	-151.79	23.56	.0070

strat 'Hiatus'

thickness = 0 m; t_dep = -2 m.y.

strat ‘Quaternary’

t_dep = 0 yrs

column	thickness(m)	x(ss)	x(sh)	dep_wat(m)	t_surf	c_surfw
w (1:2)	6.4	.75	.25	-192.02	23.80	.0026
w (3:7)	13.41	.72	.28	-193.55	23.80	.0026
w (8:10)	11.28	.64	.36	-193.55	25.50	.0034
w (11:13)	11.89	.68	.32	-193.55	23.00	.0077

end_strat

fault '1'

fault_position = 225 m; fault_xperm = .1 darcy;
fault_zperm = .1 darcy; fault_bottom = 1; fault_top = 13;

fault '2'

fault_position = 565 m; fault_xperm = .1 darcy;
fault_zperm = .1 darcy; fault_bottom = 1; fault_top = 13;

fault '3'

fault_position = 800 m; fault_xperm = .1 darcy;
fault_zperm = .1 darcy; fault_bottom = 1; fault_top = 13;

DEVIATIONS FROM THE BASE MODEL FOR REMAINING MODELS

- Halite Saturation Model 1: within "rock dol" an additional setting was used, "halite_sat=ev".
- Halite Saturation Model 2: within "rock dol" an additional setting was used, "halite_sat=ev"; horizontal fault permeability was set to 0.01 darcy's.
- Model 1: horizontal fault permeability is reduced to 0.01 D, no reduction in aquifer rock permeability.
- Model 2: horizontal fault permeability is reduced to 0.01 D, one order of magnitude reduction of aquifer rock permeability (see Table 6).
- Model 3: horizontal fault permeability is reduced to 0.01 D, two order of magnitude reduction of aquifer rock permeability (see Table 6).
- Model 4: horizontal fault permeability is reduced to 0.01 D, three order of magnitude reduction of aquifer rock permeability (see Table 6).
- Model 5: horizontal fault permeability is reduced to 0.001 D, no reduction in aquifer rock permeability.
- Model 6: horizontal fault permeability is reduced to 0.001 D, one order of magnitude reduction of aquifer rock permeability (see Table 6).
- Model 7: horizontal fault permeability is reduced to 0.001 D, two order of magnitude reduction of aquifer rock permeability (see Table 6).
- Model 8: horizontal fault permeability is reduced to 0.001 D, three order of magnitude reduction of aquifer rock permeability (see Table 6).

- Model 9: horizontal fault permeability is reduced to 0.0001 D, no reduction in aquifer rock permeability.
- Model 10: horizontal fault permeability is reduced to 0.0001 D, one order of magnitude reduction of aquifer rock permeability (see Table 6).
- Model 11: horizontal fault permeability is reduced to 0.0001 D, two order of magnitude reduction of aquifer rock permeability (see Table 6).
- Model 12: horizontal fault permeability is reduced to 0.0001 D, three order of magnitude reduction of aquifer rock permeability (see Table 6).

APPENDIX D

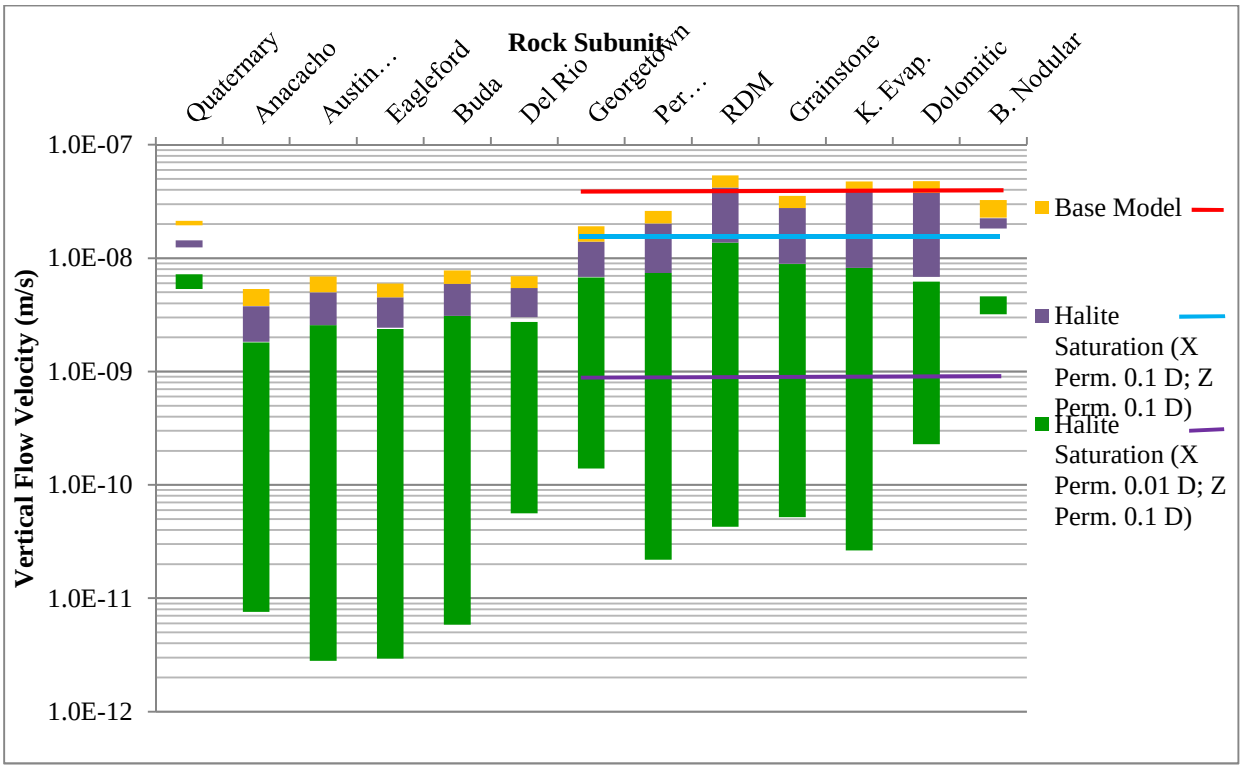

Figure AD1: Vertical flow velocity ranges for the base model and the halite-saturation models.

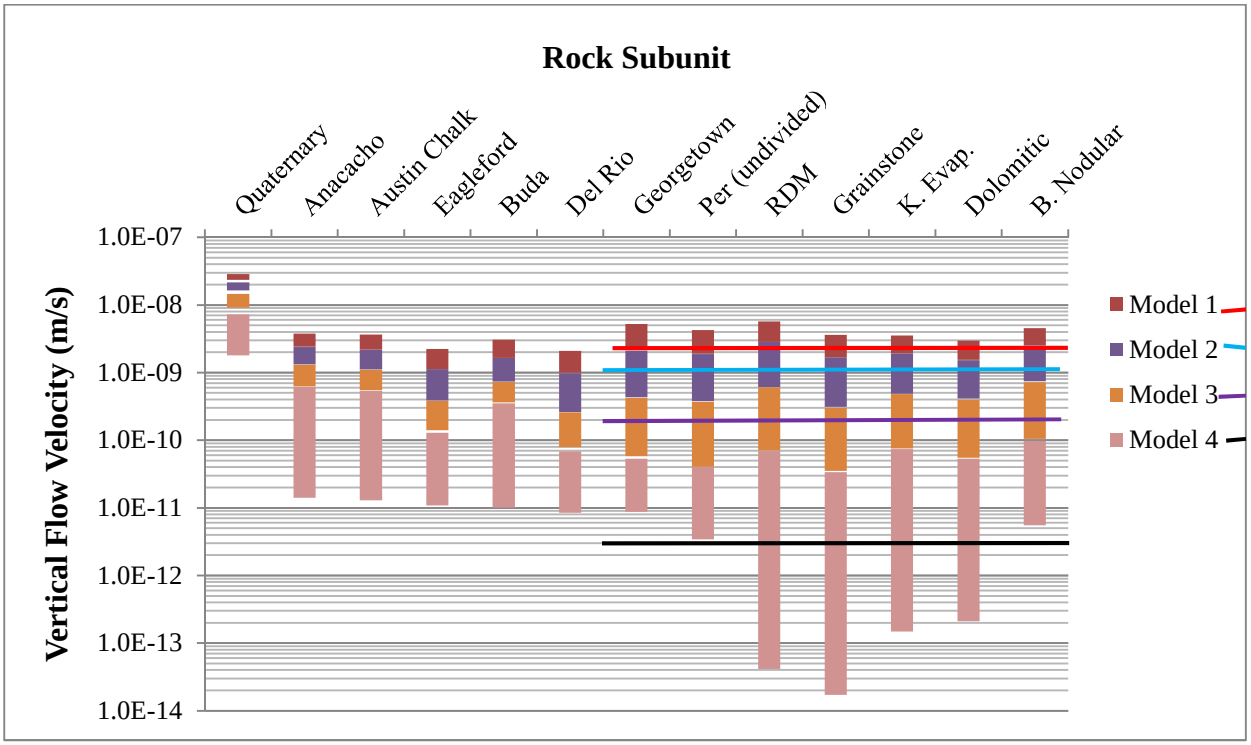

Figure AD2: Vertical flow velocity ranges for Models 1-4.

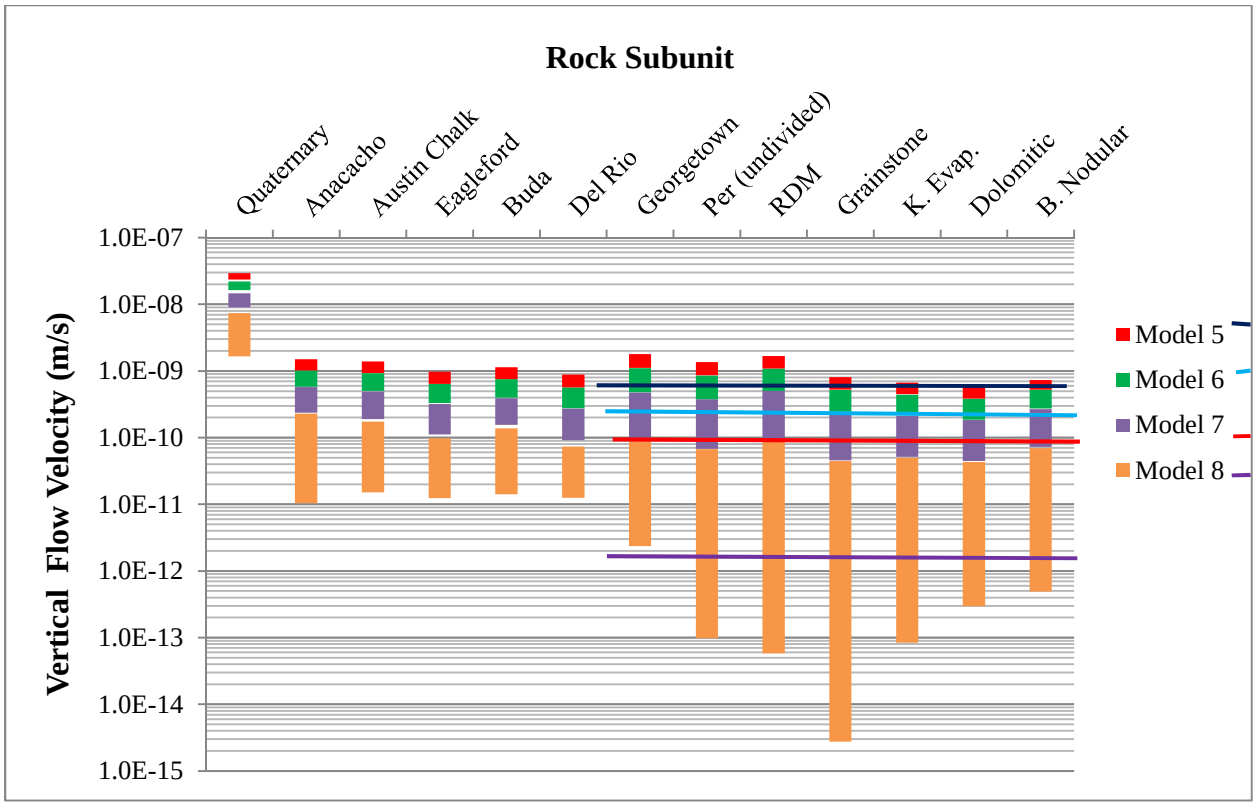

Figure AD3. Vertical flow velocity ranges for Models 5-8.

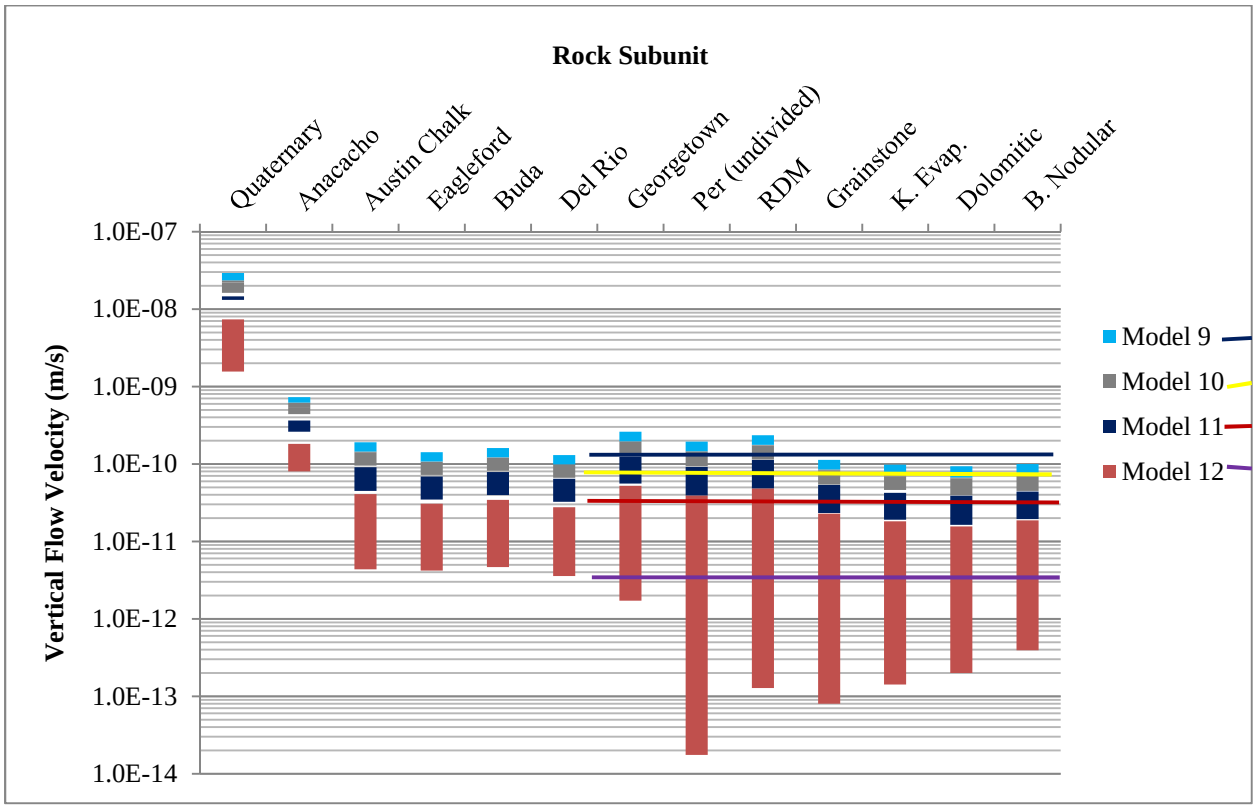

Figure AD4. Vertical flow velocity ranges for Models 9-12.

Table AD1. Flow velocity and fluid density ranges for the Base Model and Halite-Saturation Models 1-2.

Model	Subunit	Horizontal Flow Velocity Range (m/s)		Vertical Flow Velocity Range (m/s)		Fluid Density Range (kg/m^3)	
		From	To	From	To	From	To
Base	Quaternary	1.0E-07	5.3E-09	1.9E-09	5.1E-09	1012	1014
	Anacacho	2.2E-09	9.3E-10	1.6E-09	2.0E-11	1012	1013
	Austin Chalk	1.5E-09	1.3E-09	1.9E-09	3.7E-12	1011	1012
	Eagleford	1.6E-10	9.5E-11	1.5E-09	3.7E-13	1010	1011
	Buda	1.5E-09	1.0E-09	1.9E-09	1.8E-12	1010	1011
	Del Rio	1.8E-10	8.0E-11	1.5E-09	9.7E-12	1010	1011
	Georgetown	1.1E-08	9.4E-09	5.1E-09	3.2E-11	1010	1011
	Per (undivided)	1.7E-08	1.4E-08	5.9E-09	2.8E-11	1010	1010
	RDM	4.1E-08	2.1E-08	1.2E-08	2.1E-11	1010	1010
	Grainstone	3.5E-08	1.9E-08	7.7E-09	7.3E-12	1011	1012
	K. Evap.	3.1E-08	1.9E-08	6.5E-09	1.4E-11	1012	1014
	Dolomitic	3.3E-08	2.5E-08	9.9E-09	2.6E-11	1017	1018
	B. Nodular	3.8E-08	2.1E-08	9.8E-09	2.6E-10	1019	1021
Halite-Saturation 1	Quaternary	1.0E-07	5.2E-09	1.9E-09	5.3E-09	1012	1014
	Anacacho	7.9E-07	2.0E-09	1.9E-09	2.1E-11	1012	1014
	Austin Chalk	2.2E-09	1.1E-09	2.4E-09	2.4E-12	1012	1015
	Eagleford	2.5E-10	9.4E-11	2.1E-09	7.3E-11	1012	1029
	Buda	2.6E-09	8.0E-10	2.8E-09	2.0E-12	1013	1033
	Del Rio	2.9E-10	9.1E-11	2.4E-09	2.8E-10	1016	1040
	Georgetown	2.1E-08	9.6E-09	7.1E-09	8.0E-11	1023	1043
	Per (undivided)	3.6E-08	1.6E-08	1.3E-08	1.3E-13	1036	1053
	RDM	8.2E-08	4.1E-08	2.8E-08	2.4E-11	1053	1087
	Grainstone	6.3E-08	4.0E-08	1.9E-08	6.2E-11	1075	1106
	K. Evap.	1.0E-07	2.9E-08	3.3E-08	2.4E-12	1175	1176
	Dolomitic	7.1E-08	2.3E-08	3.1E-08	6.5E-10	1089	1115
	B. Nodular	9.3E-08	4.2E-08	4.2E-09	1.4E-08	1032	1056

Table AD1 continued.

Halite-Saturation 2	Quaternary	1.0E-07	4.6E-09	1.9E-09	5.3E-09	1012	1014
	Anacacho	1.5E-09	1.9E-10	1.8E-09	7.6E-12	1012	1014
	Austin Chalk	1.4E-09	5.0E-10	2.6E-09	2.8E-12	1011	1014
	Eagleford	2.8E-10	6.3E-11	2.4E-09	2.9E-12	1012	1022
	Buda	1.7E-09	5.5E-10	3.1E-09	5.8E-12	1012	1027
	Del Rio	2.6E-10	6.0E-11	2.7E-09	5.6E-11	1014	1034
	Georgetown	7.3E-09	2.5E-09	6.6E-09	1.4E-10	1018	1040
	Per (undivided)	7.9E-09	3.2E-09	7.4E-09	2.2E-11	1029	1055
	RDM	1.3E-08	4.5E-09	1.4E-08	4.3E-11	1046	1091
	Grainstone	1.1E-08	5.5E-09	8.8E-09	5.2E-11	1078	1114
	K. Evap.	1.9E-08	3.9E-09	8.2E-09	2.6E-11	1175	1176
	Dolomitic	1.4E-08	5.2E-10	6.0E-09	2.3E-10	1098	1155
	B. Nodular	2.6E-08	9.8E-09	1.4E-09	3.2E-09	1029	1082

Table AD2. Flow velocity and fluid density ranges for Models 1-4.

Model	Subunit	Horizontal Flow Velocity Range (m/s)		Vertical Flow Velocity Range (m/s)		Fluid Density Range (k/m^3)	
		From	To	From	To	From	To
1	Quaternary	1.0E-07	5.1E-09	5.1E-09	1.9E-09	1012	1014
	Anacacho	1.7E-09	4.3E-10	1.4E-09	8.5E-12	1012	1013
	Austin Chalk	1.1E-09	6.0E-10	1.5E-09	3.3E-12	1010	1012
	Eagleford	2.2E-10	6.6E-11	1.1E-09	3.6E-13	1010	1011
	Buda	9.3E-10	6.8E-10	1.4E-09	5.4E-12	1010	1011
	Del Rio	2.9E-10	4.5E-11	1.1E-09	1.5E-11	1009	1010
	Georgetown	4.4E-09	2.4E-09	3.1E-09	4.3E-11	1009	1010
	Per (undivided)	4.4E-09	2.1E-09	2.4E-09	1.2E-11	1009	1009
	RDM	7.0E-09	3.5E-09	2.9E-09	7.3E-12	1008	1009
	Grainstone	5.4E-09	2.3E-09	1.9E-09	3.9E-12	1009	1009
	K. Evap.	5.5E-09	2.4E-09	1.6E-09	7.2E-12	1009	1010
	Dolomitic	5.0E-09	2.9E-09	1.4E-09	2.0E-11	1011	1012
	B. Nodular	6.2E-09	2.6E-09	2.0E-09	2.5E-11	1018	1019
2	Quaternary	1.0E-07	4.8E-09	5.2E-09	1.8E-09	1012	1014
	Anacacho	1.7E-09	4.0E-10	1.1E-09	1.1E-11	1012	1013
	Austin Chalk	1.2E-09	5.3E-10	1.1E-09	9.1E-12	1010	1012
	Eagleford	2.2E-10	7.8E-11	7.4E-10	8.2E-12	1010	1011
	Buda	1.0E-09	5.9E-10	9.2E-10	6.7E-12	1010	1011
	Del Rio	2.0E-10	7.6E-11	7.2E-10	4.8E-12	1009	1010
	Georgetown	1.3E-09	8.2E-10	1.7E-09	7.6E-12	1009	1010
	Per (undivided)	1.9E-09	1.0E-09	1.5E-09	1.1E-11	1009	1009
	RDM	5.2E-09	2.5E-09	2.2E-09	5.7E-12	1008	1009
	Grainstone	3.4E-09	1.5E-09	1.4E-09	8.9E-12	1009	1010
	K. Evap.	6.4E-09	2.0E-09	1.4E-09	9.6E-12	1009	1010
	Dolomitic	3.7E-09	2.2E-09	1.1E-09	1.4E-11	1012	1013
	B. Nodular	5.7E-09	2.2E-09	1.8E-09	2.1E-11	1018	1019
3	Quaternary	1.0E-07	4.2E-09	5.5E-09	1.8E-09	1012	1014
	Anacacho	1.7E-09	3.2E-10	6.9E-10	1.4E-11	1012	1013
	Austin Chalk	1.3E-09	4.0E-10	5.6E-10	1.3E-11	1010	1012
	Eagleford	2.3E-10	7.0E-11	2.4E-10	1.1E-11	1010	1011

Table AD2 continued.

	Buda	1.1E-09	4.8E-10	3.7E-10	1.2E-11	1009	1011
	Del Rio	2.0E-10	7.9E-11	1.8E-10	1.1E-11	1009	1010
	Georgetown	2.2E-10	1.1E-10	3.6E-10	4.6E-12	1009	1010
	Per (undivided)	3.4E-10	1.9E-10	3.3E-10	2.2E-13	1009	1010
	RDM	1.3E-09	6.3E-10	5.4E-10	1.5E-12	1009	1011
	Grainstone	7.7E-10	3.8E-10	2.7E-10	1.4E-12	1010	1012
	K. Evap.	2.2E-09	8.5E-10	4.0E-10	1.6E-12	1012	1013
	Dolomitic	1.1E-09	7.3E-10	3.4E-10	2.1E-12	1015	1017
	B. Nodular	1.9E-09	9.8E-10	6.2E-10	6.7E-12	1019	1020
4	Quaternary	1.0E-07	4.1E-09	5.5E-09	1.8E-09	1012	1014
	Anacacho	1.7E-09	2.9E-10	5.9E-10	1.4E-11	1012	1013
	Austin Chalk	1.4E-09	3.6E-10	5.2E-10	1.3E-11	1010	1012
	Eagleford	2.3E-10	6.8E-11	1.2E-10	1.1E-11	1010	1011
	Buda	1.1E-09	4.3E-10	3.4E-10	1.0E-11	1010	1011
	Del Rio	2.1E-10	7.2E-11	6.0E-11	8.5E-12	1010	1011
	Georgetown	5.8E-11	2.7E-11	4.5E-11	8.7E-12	1010	1011
	Per (undivided)	7.2E-11	5.2E-11	3.7E-11	3.4E-12	1011	1013
	RDM	2.4E-10	1.2E-10	6.9E-11	4.2E-14	1012	1015
	Grainstone	1.1E-10	8.0E-11	3.4E-11	1.7E-14	1014	1016
	K. Evap.	3.1E-10	1.8E-10	7.3E-11	1.5E-13	1015	1017
	Dolomitic	1.7E-10	1.2E-10	5.3E-11	2.1E-13	1018	1018
	B. Nodular	3.0E-10	1.8E-10	9.2E-11	5.6E-12	1019	1020

Table AD3. Flow velocity and fluid density ranges for Models 5-8.

Model	Subunit	Horizontal Flow Velocity Range (m/s)		Vertical Flow Velocity Range (m/s)		Fluid Density Range (kg/m^3)	
		From	To	From	To	From	To
5	Quaternary	1.1E-07	3.5E-09	5.6E-09	1.7E-09	1012	1014
	Anacacho	6.1E-10	3.9E-11	4.7E-10	2.4E-12	1012	1013
	Austin Chalk	3.7E-10	4.7E-11	4.5E-10	8.4E-12	1010	1012
	Eagleford	1.9E-10	1.7E-11	3.4E-10	2.5E-12	1010	1011
	Buda	3.4E-10	7.2E-11	3.9E-10	1.1E-12	1009	1011
	Del Rio	1.9E-10	1.5E-11	3.1E-10	2.0E-12	1009	1010
	Georgetown	1.1E-09	1.8E-10	6.7E-10	1.1E-11	1009	1010
	Per (undivided)	7.1E-10	1.2E-10	5.0E-10	3.5E-12	1009	1010
	RDM	9.6E-10	1.2E-10	5.9E-10	1.7E-12	1009	1010
	Grainstone	7.6E-10	1.5E-10	2.8E-10	2.0E-12	1009	1011
	K. Evap.	9.4E-10	1.3E-10	2.2E-10	1.1E-11	1010	1012
	Dolomitic	6.7E-10	2.4E-10	2.1E-10	3.7E-12	1013	1014
	B. Nodular	1.4E-09	1.5E-10	2.1E-10	3.7E-12	1018	1019
6	Quaternary	1.1E-07	3.4E-09	5.6E-09	1.7E-09	1012	1014
	Anacacho	6.1E-10	3.8E-11	4.4E-10	2.3E-12	1012	1013
	Austin Chalk	3.8E-10	4.6E-11	4.2E-10	1.3E-11	1010	1012
	Eagleford	1.8E-10	1.8E-11	3.1E-10	9.8E-12	1010	1011
	Buda	3.9E-10	7.5E-11	3.6E-10	8.4E-12	1009	1011
	Del Rio	1.7E-10	2.5E-11	2.9E-10	4.4E-12	1009	1010
	Georgetown	5.4E-10	1.2E-10	6.2E-10	3.5E-12	1009	1010
	Per (undivided)	5.7E-10	1.1E-10	4.8E-10	2.3E-12	1009	1010
	RDM	1.1E-09	1.6E-10	5.8E-10	5.5E-14	1009	1010
	Grainstone	6.8E-10	1.3E-10	2.8E-10	1.4E-12	1009	1011
	K. Evap.	1.2E-09	1.4E-10	2.2E-10	2.7E-12	1010	1012
	Dolomitic	6.5E-10	2.3E-10	2.0E-10	3.5E-12	1013	1014
	B. Nodular	1.3E-09	1.6E-10	2.5E-10	4.5E-12	1018	1019
7	Quaternary	1.1E-07	3.3E-09	5.7E-09	1.7E-09	1012	1014
	Anacacho	6.1E-10	3.3E-11	3.4E-10	5.9E-12	1012	1013
	Austin Chalk	4.0E-10	4.0E-11	3.0E-10	1.6E-11	1010	1012
	Eagleford	1.8E-10	1.7E-11	2.1E-10	1.4E-11	1010	1011

Table AD3 continued.

	Buda	4.3E-10	7.0E-11	2.3E-10	1.8E-11	1009	1011
	Del Rio	1.7E-10	2.4E-11	1.8E-10	1.8E-11	1009	1010
	Georgetown	2.3E-10	4.6E-11	3.8E-10	9.7E-12	1009	1010
	Per (undivided)	2.5E-10	6.1E-11	3.1E-10	2.9E-13	1009	1010
	RDM	6.4E-10	1.4E-10	4.1E-10	3.3E-13	1009	1011
	Grainstone	4.1E-10	9.5E-11	2.0E-10	1.1E-12	1009	1011
	K. Evap.	9.0E-10	1.4E-10	1.6E-10	1.6E-12	1010	1012
	Dolomitic	4.4E-10	1.7E-10	1.4E-10	1.5E-12	1013	1015
	B. Nodular	7.4E-09	1.7E-10	2.0E-10	3.2E-12	1018	1019
8	Quaternary	1.1E-07	3.0E-09	5.7E-09	1.7E-09	1012	1014
	Anacacho	6.1E-10	2.7E-11	2.2E-10	1.0E-11	1012	1013
	Austin Chalk	4.1E-10	3.4E-11	1.6E-10	1.5E-11	1010	1012
	Eagleford	1.9E-10	1.7E-11	8.6E-11	1.2E-11	1010	1011
	Buda	4.2E-10	6.3E-11	1.2E-10	1.4E-11	1010	1011
	Del Rio	1.7E-10	2.2E-11	6.1E-11	1.3E-11	1009	1011
	Georgetown	7.2E-11	1.6E-11	8.6E-11	2.4E-12	1009	1011
	Per (undivided)	6.8E-11	3.0E-11	6.8E-11	9.8E-14	1009	1011
	RDM	2.0E-10	7.3E-11	9.1E-11	5.8E-14	1010	1013
	Grainstone	1.0E-10	4.7E-11	4.5E-11	2.8E-15	1011	1014
	K. Evap.	2.5E-10	9.0E-11	5.0E-11	8.4E-14	1012	1015
	Dolomitic	1.4E-10	8.0E-11	4.3E-11	3.0E-13	1016	1017
	B. Nodular	2.2E-10	1.0E-10	6.9E-11	4.9E-13	1019	1020

Table AD4. Flow velocity and fluid density ranges for Models 9-12.

Model	Subunit	Horizontal Flow Velocity Range (m/s)		Vertical Flow Velocity Range (m/s)		Fluid Density Range (kg/m^3)	
		From	To	From	To	From	To
9	Quaternary	1.1E-07	2.7E-09	5.8E-09	1.6E-09	1012	1014
	Anacacho	2.8E-10	3.6E-12	1.1E-10	7.6E-11	1012	1013
	Austin Chalk	7.5E-11	3.5E-12	4.6E-11	3.4E-12	1011	1013
	Eagleford	3.4E-11	2.8E-12	3.4E-11	1.6E-12	1010	1012
	Buda	4.9E-11	8.2E-12	3.9E-11	9.7E-13	1010	1012
	Del Rio	3.4E-11	2.3E-12	3.1E-11	7.8E-13	1010	1012
	Georgetown	2.3E-10	1.1E-11	6.5E-11	3.0E-12	1010	1012
	Per (undivided)	6.4E-11	1.7E-11	4.9E-11	2.6E-12	1010	1013
	RDM	3.8E-10	1.1E-10	5.8E-11	2.6E-12	1012	1013
	Grainstone	7.5E-11	1.9E-11	2.8E-11	2.2E-12	1012	1014
	K. Evap.	2.2E-10	7.2E-12	2.2E-11	6.7E-12	1013	1016
	Dolomitic	7.6E-11	1.4E-12	2.6E-11	1.8E-12	1016	1017
	B. Nodular	3.4E-10	3.9E-12	2.7E-11	8.9E-13	1019	1020
10	Quaternary	1.1E-07	2.7E-09	5.8E-09	1.6E-09	1012	1014
	Anacacho	2.8E-10	3.6E-12	1.1E-10	7.6E-11	1012	1013
	Austin Chalk	7.6E-11	3.2E-12	4.7E-11	3.6E-12	1011	1013
	Eagleford	3.4E-11	2.9E-12	3.5E-11	2.8E-12	1010	1012
	Buda	5.7E-11	8.1E-12	3.9E-11	2.9E-12	1010	1012
	Del Rio	3.4E-11	3.5E-12	3.2E-11	1.9E-12	1010	1012
	Georgetown	7.7E-11	1.1E-11	6.7E-11	1.8E-12	1010	1012
	Per (undivided)	6.5E-11	1.6E-11	5.0E-11	1.4E-12	1010	1013
	RDM	1.6E-10	4.3E-11	6.0E-11	1.2E-12	1012	1014
	Grainstone	7.8E-11	1.9E-11	2.8E-11	7.7E-13	1012	1015
	K. Evap.	2.2E-10	6.9E-13	2.3E-11	3.7E-12	1013	1016
	Dolomitic	7.5E-11	1.4E-11	2.5E-11	9.5E-13	1016	1017
	B. Nodular	3.0E-10	1.1E-12	2.7E-11	8.9E-13	1019	1020
11	Quaternary	1.1E-07	2.7E-09	1.6E-09	5.8E-09	1012	1014
	Anacacho	2.8E-10	3.5E-12	1.0E-10	7.8E-11	1012	1013
	Austin Chalk	7.7E-11	2.7E-12	4.6E-11	4.0E-12	1011	1012
	Eagleford	3.4E-11	3.2E-12	3.4E-11	4.1E-12	1010	1012

Table AD4 continued.

	Buda	6.7E-11	7.8E-12	3.9E-11	5.3E-12	1010	1012
	Del Rio	3.4E-11	3.8E-12	3.2E-11	4.9E-12	1010	1012
	Georgetown	6.4E-11	9.2E-12	6.8E-11	3.7E-12	1010	1012
	Per (undivided)	5.5E-11	1.3E-11	5.3E-11	3.0E-14	1010	1012
	RDM	1.3E-10	1.0E-11	6.4E-11	1.8E-13	1012	1014
	Grainstone	6.6E-11	1.4E-11	3.0E-11	4.1E-13	1013	1015
	K. Evap.	1.6E-10	1.2E-11	2.4E-11	7.9E-13	1014	1016
	Dolomitic	6.8E-11	2.4E-11	2.2E-11	6.8E-13	1016	1017
	B. Nodular	1.4E-10	1.4E-11	2.5E-11	7.4E-13	1019	1020
12	Quaternary	1.1E-07	2.7E-09	5.8E-09	1.6E-09	1012	1014
	Anacacho	2.8E-10	3.5E-12	1.0E-10	8.0E-11	1012	1013
	Austin Chalk	7.8E-11	2.3E-12	3.6E-11	4.4E-12	1011	1012
	Eagleford	3.4E-11	3.2E-12	2.6E-11	4.2E-12	1010	1012
	Buda	6.8E-11	7.6E-12	3.0E-11	4.7E-12	1010	1012
	Del Rio	3.4E-11	3.6E-12	2.4E-11	3.6E-12	1010	1011
	Georgetown	4.3E-11	7.5E-12	5.1E-11	1.7E-12	1010	1011
	Per (undivided)	3.4E-11	1.1E-11	3.9E-11	1.8E-14	1010	1012
	RDM	8.3E-11	1.8E-11	4.8E-11	1.3E-13	1011	1014
	Grainstone	4.4E-11	1.3E-11	2.3E-11	8.0E-14	1012	1015
	K. Evap.	8.7E-11	1.7E-11	1.8E-11	1.4E-13	1014	1016
	Dolomitic	4.8E-11	1.9E-11	1.5E-11	2.0E-13	1016	1018
	B. Nodular	7.0E-11	2.1E-11	1.8E-11	3.9E-13	1019	1020

APPENDIX E

Table AE1. Water level data (modified from Hamilton et al., 2006).

Well ID #	Date	Measuring Point Height (ft)	Measuring Point Elevation (ft)	LSD (ft)	Water Level	Aquifer
6823302	7/18/2005	1.00	643.59	642.59	628	Recharge
6823304	7/21/2005	0.36	626.53	626.17	643	Artesian
6823617	7/21/2005	2.72	635.94	633.22	647	Saline
6823616A	7/21/2005	2.40	637.82	635.42	646	Saline
6823619B	7/21/2005	2.30	636.71	634.41	644	Saline
6823302	10/24/2005	1.00	643.59	642.59	628	Recharge
6823304	10/27/2005	0.36	626.53	626.17	641	Artesian
6823617	10/26/2005	2.72	635.94	633.22	640	Saline
6823616A	10/26/2005	2.40	637.82	635.42	643	Saline
6823302	7/17/2006	1.00	643.59	642.59	624	Recharge
6823304	7/20/2006	0.36	626.53	626.17	631	Artesian
6823302	10/11/2006	1.00	643.59	642.59	624	Recharge
6823304	10/11/2006	0.36	626.53	626.17	632	Artesian
6823302	1/30/2007	1.00	643.59	642.59	626	Recharge
6823304	1/30/2007	0.36	626.53	626.17	636	Artesian
6823302	7/9/2007	1.00	643.59	642.59	629	Recharge
6823304	7/12/2007	0.36	626.53	626.17	643	Artesian
6823617	7/12/2007	2.72	635.94	633.22	645	Saline
6823616A	7/12/2007	2.40	637.82	635.42	646	Saline
6823619B	7/12/2007	2.30	636.71	634.41	643	Saline
6823302	11/1/2007	1.00	643.59	642.59	629.8	Recharge
6823304	11/2/2007	0.36	626.53	626.17	646.42	Artesian
6823617	11/2/2007	2.72	635.94	633.22	643.9	Saline
6823616A	11/1/2007	2.40	637.82	635.42	641.05	Saline
6823619B	11/1/2007	2.30	636.71	634.41	640.52	Saline

Table AE1 continued.

6823302	2/4/2008	1.00	643.59	642.59	629	Recharge
6823304	2/5/2008	0.36	626.53	626.17	644	Artesian
6823617	2/5/2008	4.46	637.68	633.22	645	Saline
6823616A	2/7/2008	4.91	640.33	635.42	647	Saline
6823619B	2/5/2008	5.20	639.61	634.41	644	Saline
6823302	8/6/2008	1.00	643.59	642.59	626	Recharge
6823304	8/7/2008	0.36	626.53	626.17	636	Artesian
6823617	8/6/2008	4.46	637.68	633.22	637	Saline
6823616A	8/6/2008	4.91	640.33	635.42	637	Saline
6823619B	8/6/2008	5.20	639.61	634.41	636	Saline
6823302	10/23/2008	1.00	643.59	642.59	626	Recharge
6823304	10/22/2008	0.36	626.53	626.17	636	Artesian
6823617	10/24/2008	4.46	637.68	633.22	637	Saline
6823616A	10/23/2008	4.91	640.33	635.42	639	Saline
6823619B	10/23/2008	5.20	639.61	634.41	637	Saline
6823302	2/18/2009	1.00	643.59	642.59	626	Recharge
6823304	2/24/2009	0.36	626.53	626.17	635	Artesian
6823617	2/25/2009	4.46	637.68	633.22	636	Saline
6823616A	2/25/2009	4.91	640.33	635.42	636	Saline
6823619B	2/24/2009	5.20	639.61	634.41	635	Saline
6823302	7/20/2009	1.00	643.59	642.59	623	Recharge
6823304	7/20/2009	3.94	630.11	626.17	627	Artesian
6823617	7/30/2009	4.46	637.68	633.22	628	Saline
6823616A	7/30/2009	4.91	640.33	635.42	629	Saline
6823619B	7/30/2009	5.20	639.61	634.41	627	Saline
6823302	10/23/2009	1.00	643.59	642.59	626	Recharge
6823304	No Data	0.36	626.53	626.17	No Data	Artesian
6823616A	11/6/2009	5.23	640.65	635.42	639	Saline
6823619B	11/6/2009	5.20	639.61	634.41	636	Saline

VITA

Scott Ryan Tipple was born on August, 1986 in Fort Wayne, Indiana, to Bernita Elaine Pitts Tipple and John Mark Tipple. In August 2000, he moved with his family to Abita Springs, Louisiana. Scott graduated high school from Saint Paul's School with Honors in May 2005. During his undergraduate tenure at Louisiana State University (LSU), he attended Geology Field Camp as a freshman and a senior. Scott was a Taylor Opportunity Program for Students (TOPS) scholarship recipient from 2005-2009. In addition, he received a 2005 Geology and Geophysics Departmental scholarship for freshmen field camp. He graduated from LSU in December 2009 with a Bachelor's of Science degree in Professional Geology. While pursuing a Master's of Science degree in the Geology and Geophysics Department at LSU, he was a Geology Field Camp senior teaching assistant during the summers of 2010 and 2011. He also taught introductory labs during the academic year. His research was awarded three grants in 2011 by the following institutions: i) American Association of Petroleum Geologists (AAPG), ii) Geological Society of America (GSA), and iii) Gulf Coast Association of Geological Societies (GCAGS). He was elected President of LSU's AAPG Student Chapter for 2011-2012, as well as Social Chair for 2010-2011. In 2012, he competed on LSU's Imperial Barrel Award team and presented his research at the annual AAPG Convention and Exhibition in Long Beach, California. He has accepted an internship with Chesapeake Energy for 2012.